2016-07-01

Emission from Black Holes and Supernovae in the Early Universe

Brandon Kerry Wiggins
Brigham Young University

BYU ScholarsArchive Citation

Wiggins, Brandon Kerry, "Emission from Black Holes and Supernovae in the Early Universe" (2016). *All Theses and Dissertations*. 6432.
https://scholarsarchive.byu.edu/etd/6432

Emission from Black Holes and Supernovae

in the Early Universe

Brandon Kerry Wiggins

A dissertation submitted to the faculty of
Brigham Young University
in partial fulfillment of the requirements for the degree of

Doctor of Philosophy

David Neilsen, Chair
Wesley Even
Denise Stephens
Eric Hirschmann
J. Ward Moody
Michael Joner

Department of Physics and Astronomy

Brigham Young University

July 2016

ABSTRACT

Emission from Black Holes and Supernovae
in the Early Universe

Brandon Kerry Wiggins
Department of Physics and Astronomy, BYU
Doctor of Philosophy

To constrain the era when the first galaxies and stars appeared upcoming instruments will rely on the brightest events in the universe: supernovae and brilliant emission from massive black holes. In this dissertation, we investigate the observability of certain types of supernovae of the very first stars (Population III stars) and find that while these events are sufficiently luminous to be observed with deep-sky instruments such as the James Webb Space Telescope (JWST), they may not observe these particular types of events in their lifetimes. We next explore the origins of massive black holes and introduce the direct collapse hypothesis of supermassive black hole formation. We model CR7, an apparently metal-free, luminous, Lyman-α emitting galaxy, as if it were powered by a massive direct collapse black hole and find that such a black hole can account for CR7's impressive Lyman-α flux. We finally investigate the nature of the connection between water megamasers, very bright radio sources originating from population inversion in dense, shocked gas around massive black holes and hydroxyl megamasers which generally accompany star formation. We carry out a ~ 60 hour radio survey for water emission among galaxies hosting OH megamaser hosts to assess the connection between the two types of emission. We find marginally statistically significant evidence that OH megamasers exclude water kilomasers and confirm with high levels of significance ($> 8\sigma$) the presence of a water megamaser in II Zw 96, establishing this object as the second galaxy known to cohost simultaneous water and hydroxyl megamasers.

Keywords: supernovae, black holes, Lyman-alpha, megamaser

ACKNOWLEDGMENTS

This work would not have been possible without the advisement, support and counsel of Wesley Even, Joseph Smidt, Victor Migenes, Christopher Fryer, Jarrett Johnson, Joshua Dolence, Christopher Malone, Ryan Wollaeger, David Neilsen and many others. This dissertation is dedicated to Angela Wiggins for her unwavering, loving support during this wonderful if short chapter of our lives.

CONTENTS

CHAPTER

ONE

INTRODUCTION

> *. . . [A] marshmallow dropped onto the surface of a neutron star releases enough gravitational potential energy to produce an explosion equal to that of a medium-sized atomic bomb on Earth. This is the realm of physical reality we will be exploring.*
>
> Fulvio Melia

Observational astronomy favors the detection of the brightest astrophysical sources. Electromagnetic radiation, including those from very luminous sources, has long served as the predominant messenger by which the astronomer has interpreted the cosmos. Radiation from high-energy and high-luminosity events have made important contributions to our understanding of the universe as a whole: Type Ia supernovae were employed to constrain the presence of dark energy, luminous quasars have elucidated the epoch of reionization. Whether these events be exploding stars or accreting black holes, high energy phenomena further serve as critical laboratories for matter at the most extreme of energies and densities. Correctly interpreting or predicting this emission requires effective modeling of these systems.

With upcoming telescopes such as the James Webb Space Telescope (JWST) which is scheduled to launch in 2018, WFIRST, and the Square Kilometer Array (SKA), the community will be situated to study the distant past like never before. To probe the era of the first stars (13.5 billion years ago) and the era of the first galaxies (13 billion years ago), these powerful instruments will rely heavily on the most luminous astrophysical events to provide constraints on these epochs. These may include the spectacular supernova explosions of the first stars and the emission of powerful young quasars. In this dissertation, we investigate the observability of some of these events from high redshift. We explore the exotic origins of supermassive black holes and model emission from massive black hole seeds. We conclude our discussion with an investigation of water megamasers, tracers of active supermassive black hole activity, commenting on the relationship between hydroxyl and water megamasers.

1.1 The Exotic Early Universe

Because the universe had a beginning, there must have been a first star. Supercomputer simulations now show that the first stars probably formed at redshift $z \sim 20$, or only $200-400$ million years after the Big Bang in an event now called “Cosmic Dawn.” But star formation during this time was very different from what we observe in the universe today. The first stars formed in small pregalactic structures known as cosmological halos, in pristine hydrogen and helium gases that were devoid of the heavier elements and dust that are ubiquitous in star-forming clouds today. A hypothetical telescope image of this time would not contain spiral and elliptical galaxies, but individual stars sprinkled through the universe’s invisible dark-matter filamentary structure and slowly collecting in small stellar communities.

Because these stars were discovered most recently, they are called Population III (Pop III) stars; Pop III stars were created from only hydrogen and helium, and they would have had some unfamiliar characteristics. Stars may have routinely been up to hundreds of times more massive than the Sun and tens of millions of times more luminous (e.g., Hirano et al. 2014). A few may have been a hundred thousand times the mass of the Sun and may have been the precursors of supermassive black holes (Wise et al. 2008; Regan and Hehnelt 2009a). In a sense, one can think of this as the universe's very own *Jurassic era* when it manufactured *monsters.* These cosmological "dinosaurs" became extinct long ago as the first stars spewed heavier elements throughout the cosmos in spectacular supernova explosions. Chemically enriched interstellar clouds cool more rapidly and so are unable to grow to such large masses before collapsing to form stars. Thus, the modern cosmos is incapable of making the gigantic stars that were found in the primeval universe. Remains of this period likely persist today in the chemical composition of ancient, dim stars of the halos of galaxies.

Our interest in the first stars extends beyond their curious properties; these stars populated the cosmos with heavy elements, allowing for the later formation of planets and life. Their light also gradually transformed the universe from a cold, dark, featureless void into the vast, hot, transparent cosmic web of galaxies we observe today (Bromm et al. 2009). These stars and this period are key in resolving long-standing cosmological mysteries such as how super-massive black holes billions of times more massive than the Sun appeared less than a billion years after the Big Bang (Moretti et al. 2014). Primordial stars also populated the first primitive galaxies, which will be principal targets of the James Webb Space Telescope (JWST), which is slated to launch in 2018 (Bromm et al. 2009). Understanding the nature of the first stars is crucial to predicting the luminosities and spectra of primeval galaxies.

Unfortunately, these stars are beyond the reach of current observations. Individual primordial stars will not even be visible to the next generation of 30-meter class telescopes or space missions because they literally lie near the edge of the observable universe, when it was only 200 million years old. But the first stars may have died in luminous supernova explosions, and these spectacular events may be visible to upcoming instruments. Indeed, supernovae in the local universe can outshine their entire host galaxies and have now been detected as far away as 10 billion light years. With the coming telescopes, it may be possible to see even more distant explosions, which took place at Cosmic Dawn. These ancient supernovae (SNe) may offer the first observational constraints on this important but elusive and distant epoch of cosmic history.

To interpret the findings of future observations, cosmologists rely on predictions regarding the character, the luminosity, and the frequency of ancient SNe. In particular, cosmologists must know whether Pop III SNe are sufficiently luminous to be observable to upcoming instruments. Computer simulations are employed to provide models for the light curves (total luminosity as a function of time) and the spectra of these spectacular events. These will be used by observers to identify and characterize ancient SNe. Some types of primordial SNe have been modeled in the literature (see, e.g., Whalen et al. 2013a, 2013b, 2014b). In the next chapter, we will investigate the observability of Pop III pair-instability supernovae and hypernovae, which are types of brilliant supernovae explosions of very large stars. This era of the first stars in the universe may well have been the epoch of its most luminous supernovae if the first stars were sufficiently massive.

1.2 How Big was Big?

The argument that Pop III stars may have been more massive than stars today hinges on the simple chemistry of primordial gas. To form stars, clouds of gas must become gravitationally unstable and collapse. A cloud is supported by thermal pressure. In equilibrium we expect that the thermal energy of the cloud will be on the order of the gravitational potential energy,

$$3Nk_BT = \frac{3}{5}\frac{GM_J^2}{R}, \tag{1.1}$$

where N is the number density of the gas multiplied by the volume of the cloud, k_B is the Boltzmann constant, T is temperature, M_J is the Jeans mass, R is radius with gravitational constant G.

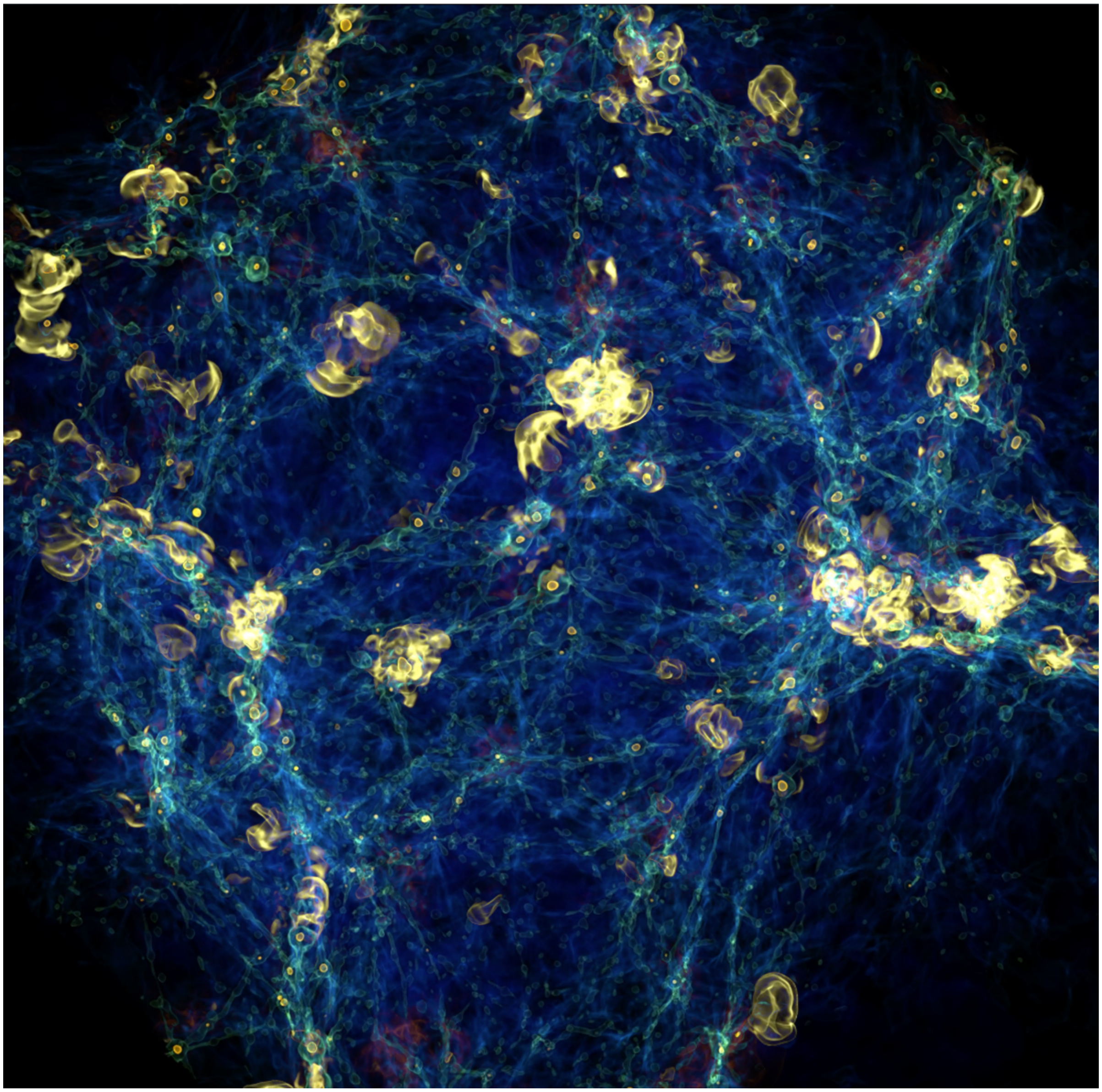

Figure 1.1 Snapshot of a cosmological simulation at $z \simeq 15$ carried out in *ENZO* run by Joseph Smidt (LANL). Contours correspond to surfaces of iso-density which appear in cool hues. The network of filaments and voids is apparent. Overlaid is gas temperature plotted in warmer colors. Star formation has begun, driving outflows of hot gas and creating HII regions (which appear as brighly colored plumes) into the intracluster medium.

Note that for a cloud of given size R, equation (1.1) implicitly defines a maximum mass M_J which can be supported by a given temperature T. If the mass of the cloud exceeds this, we expect the cloud to contract. During such a contraction one might expect the temperature of the cloud to increase and stability in the cloud is regained at some smaller radius $R' < R$. However if the cooling timescale is much quicker than the timescale on which the cloud's radius is changing (also termed the *dynamical time*), the cloud will radiate away this extra heat faster than it can regain it through collapse. If this is the case, the temperature of the cloud does not increase during contraction even as gravitational potential energy of the system increases due to diminishing R. The process quickly runs away, leading to a gravitational collapse of the cloud provided that it never becomes optically thick to the escaping radiation. It is easy to see that the nature of the collapse of a candidate star-forming cloud is dependent upon its ability to cool. Star formation in the local universe would have been different than the star formation which took place in very early universe. The modern ISM is composed of many elements that provide a host of transitions which can be collisionally excited and subsequently spontaneously decay, emitting photons which leave the system and cool the gas. As this gas cools, it contracts and the environment becomes optically thick to UV radiation. In these dark, cool environments, molecules can form and persist, giving rise to another symphony of rotational and vibrational states that can also be excited by collisions. Molecule formation is enhanced by the presence of dust, very large particles where atoms can meet to react. Molecules can act as additional coolants for these clouds which can become gravitationally unstable, either by cooling or by mechanical compression of the gas, say from interactions with supernova remnants. The clouds that become gravitational unstable to produce a single star or a single binary system are termed "cores." A "clump" that consists of a number of cores may typically contain $\sim 10^3$ $M_\odot$ in gas.

In the early cosmos, only hydrogen, helium and small amounts of lithium comprised the baryonic universe. Compared to heavier elements, hydrogen and helium have very simple electron structures and thus limited channels to cool. To trigger Lyman cooling, or to collisionally excite the $n = 2$ state in hydrogen, requires temperatures of ~ 10 eV or $\sim 10,000$ K. Such clouds could grow to enormous sizes before cooling and collapsing, $\sim 10^8$ $M_\odot$! But it was not from such large clouds that population III stars formed. When WMAP results indicated that reionization took place earlier than some cosmologist had predicted, it was clear that clouds in the early universe were collapsing *earlier* and with *smaller masses* (Schneider 2008). Only then was it appreciated that molecular hydrogen H_2 could act as an effective coolant and give rise to the smaller halos needed to explain WMAP results. Molecular hydrogen forms in very trace amounts as halos grow in mass, but its rotational transitions[1] can be excited at ~ 1000 K (see Figure 1.2) which caps primordial halo growth to sizes around $\sim 10^4 - 10^6$ $M_\odot$ with $< 1\%$ of the gas going into stars. This is substantially larger than collapsing cores or clumps in the modern universe ($\sim 10^3$ $M_\odot$), leaving open the possibility that population III stars may have been much more massive than their modern stellar counterparts.

Studying the collapse of massive halos to star formation has been the subject of many numerical studies. The collapsing cloud should possess some net angular momentum and the imploding flow forms an accretion disk on small scales which feeds the young protostar. Star formation is a challenging simulation problem with a host of temporal and spatial scales. Some calculations suggest that the disk fragments and a series of population III stars form instead of a single massive star. It is not surprising, therefore, that the literature is not always in agreement on how massive Pop III stars actually were. Some studies suggest that they were tens of solar masses (e.g., Hosokawa et al. 2011), but others have found that some may have had masses of 500-600 times that of the Sun (e.g., Hirano et al. 2014). These estimates are largely based on simulations that attempt to follow the collapse and accretion of gas onto a protostar; however, no high-resolution simulation

---

[1] Molecular hydrogen possess a number of vibrational states v up to its dissociation energy ~ 4.48 eV. Each vibrational state possess multiple rotational states J. Below 10^4 K, only rotational states in the ground vibrational state are excited. These correspond to energies in the infrared, e.g. $J = 2 \rightarrow 0$: 28.22 μm, $J = 3 \rightarrow 1$: 17.04 μm.

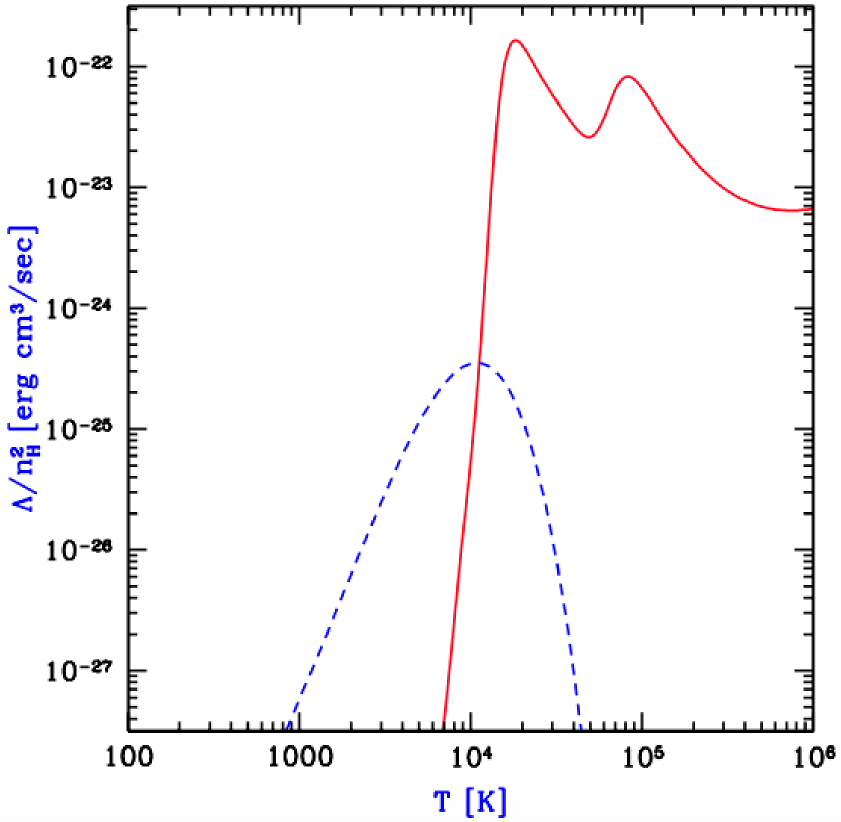

Figure 1.2 Cooling rates Λ per unit volume for atomic metal-free primordial gas (solid red) and molecular hydrogen (dashed blue). The two peaks in the red curve at 10^4 K and 10^5 K correspond to the energy of hydrogen Lyman-α and helium cooling respectively. Once appreciable amounts of molecular hydrogen form, halos cannot grow past masses which can be supported by $\sim$ 1000 K. Credit: Barkana & Loeb 2000, astro-ph/0010468.

has evolved the protostar for more than a 1000 years, while the time between the formation and evaporation of its accretion disk may take millions of years (see Whalen 2012). Consequently, simulations cannot yet constrain the masses of the first stars.

Some properties of primordial stars can be inferred from the chemical abundances found in old halo stars in our own galaxy (see, e.g., Christlieb et al. 2002, Frebel et al. 2005). When the first stars died, ashes from their explosions may have been taken up in the formation of the next generation of stars. Joggerst et al. (2009) found that the cumulative nucleosynthetic yields of $15-40$ $M_{\odot}$ Pop III supernovae are a good match to the elemental abundances measured in the extremely metal-poor stars to date. This finding would apparently contradict the results of simulations predicting Pop III stars of 100s of solar masses; however, “stellar archeology” as this study is called, is still in its infancy because of small sample sizes and the fact that the very metal-poor stars found so far reside in the galactic halo instead of the galactic nucleus, where most second-generation stars would be expected (Hirano et al. 2014). Most sources place Pop III stars as having between 50 to 500 solar masses. In chapter 2, we shall model pair-instability and hypernovae to assess their observability to upcoming instruments. In doing this, we are exploring the paradigm that the first stars were very large.

1.3 When Massive Stars Die

1.3.1 Core-collapse

Massive Pop III stars would have evolved like stars in the modern universe, moving from the main sequence as hydrogen is depleted from their cores. As one suspects, massive Pop III stars also commence burning of successively heavier elements as is predicted for stars in the modern universe. Stars with masses greater than about 8 $M_{\odot}$ would have experienced core-collapse and subsequent supernova. We do not model lightcurves from population III core-collapse events in this thesis. However, because the core-collapse mechanism and issues arising in attempting to reproduce it inform and motivate both the method and our need to explode stars numerically, we provide a brief review of the core-collapse mechanism in this subsection.

Sufficiently massive stars will burn through Ne and Si, leading to Fe buildup in late stages of burning. The star's core contracts as the supply of Si is exhausted, raising its temperatures and pressures. Fe, however, is remarkably stable and undergoes an endothermic as opposed to exothermic nuclear reaction. An energy crisis ensues as the stellar core contracts and temperatures soar. Photons become hot enough to begin dissociating Fe in the core. An example of such a reaction is

$$^{56}\mathrm{Fe}+\gamma=13\,^{4}\mathrm{He}+4\mathrm{n}.$$

The above and similar processes are *endothermic*, which eliminate high energy photons from the core and so drain it of radiation pressure. When dissociation begins to outpace recombination, the process quickly runs away and models predict that the surface of the core contracts at a sizable fraction of the speed of light.

Supernovae, however, are observed as brilliant explosions and so there must be a mechanism for reversing core-collapse. In the 1970's it was thought that free nucleons from photodisintegration would begin to provide pressure and halt contraction before one reached nuclear densities (see Burrows 2012 for a review). But Bethe et al. (1979) showed that infall energy is actually channeled into many nuclear states of the nucleons. This effectively raises the "specific heat" of the material, allowing the collapsing core to reach nuclear densities. At this point free nucleons are mutually repelled by the strong force, the equation of state "stiffens", and the core ceases to contract.

The increase in densities and temperatures during infall facilitate electron capture on nuclei. High energy electrons overcome reaction barriers, fusing with protons and producing neutrons and electron neutrinos (ν_e). As temperatures continue to increase and pair- production becomes significant, positron captures on nuclei produce electron antineutrinos (ν_e^-). Electron-positron annihilation and nucleon-nucleon bremstrahlung reactions provide neutrino- antineutrino pairs in all neutrino flavors. Pure neutrino reactions take place between neutrino flavors as collapse ensues.

Initially, neutrinos were not thought to affect supernova processes, as they are able to penetrate "ĂIJlight years of lead"Ăİ before interacting. But when matter reaches densities around $10^{11} - 10^{12}$ g cm^{-3}, neutrino trapping occurs because the neutrino diffusion timescale becomes larger than the free-fall timescale of the gas (see the first portion of Janka et al. 2012 for a review). In spite of this trapping, collapse is not halted until nuclear densities are reached.

As the stellar core increases in density, neutrino optical depths reach $\sim 10^5$ and the probability of a neutrino interacting with a proton to create an electron and proton increase. Thus not all electrons are lost to capture during core-collapse: the process is balanced by the increasing reverse reactions as densities in the core scale. In effect one can think of neutrino trapping as locking the number of electrons and neutrinos in a given mass shell. Because large numbers of electrons persist in the process, neutrons are unable to leave nuclei that already have too many neutrons for comfort. This is the mechanism that preserves nuclei all the way until collapse is halted at nuclear densities. If this were not the case, bounce would occur at lower densities, which means lower neutrino optical depths, which translates into a harder, shorter (about 100 millisecond) pulse of neutrinos from the star at the moment of death (Burrows 2012). Neutrino trapping theory is successful in dragging the event out to 10s of seconds consistent with neutrino observations of SN 1987a (see e.g. Hirata et al. 1987).

The literature is largely in agreement with events prior to core bounce. Indeed, some aspects of the theory are even verified by observation. But the evolution and birth of the supernova after core-collapse remains a troubling open problem in the literature. Naively, we might assume that bounce drives a shock wave which propagates through the star, bursts through the stellar photosphere, disrupting the star in a brilliant explosion. Though the gravitational binding energy of the infalling core is apparently sufficient to power at 10^{53} erg explosion (100 times more energetic than typical

Type II supernovae), numerical models fail to produce explosions with only the foregoing physics.

The issue lies in what is known the supernova community as the “stalled shock” problem. Explanations of varying sophistication exist in the literature, but the essential idea is this. During collapse the core effectively ĂIJseparatesĂİ into two regions: a sub-sonically collapsing inner core and a supersonically collapsing outer core. After neutrino trapping, the inner core-collapses homologously and subsonically. When this inner core stops collapsing and re- expands it does so into the supersonically collapsing outercore to drive the shock wave which will presumably destroy the star. All shocks carry energy and all shocks heat material as they pass over it. The high-energy shock passes through the iron-rich outer core and heats it to extreme temperatures. This leads to photodisintegration of the Fe, which effectively raises the specific heat of the material and leads to a less efficient conversion between kinetic energy of the shock and pressure. In short, a chunk the kinetic energy budget of the shock goes into photodisintegration. Once the neutrinos leave, carrying away the vast majority of the binding energy of the core, the shock stalls and dissipates. In some calculations, the lifetime of the would-be shock wave is a very short 5 milliseconds (Burrows 2012).

It was Stirling Colgate and Dick White of Lawrence Livermore National Laboratory who first proposed what is now accepted as the correct “shock revival” mechanism. Though their initial proposal was flawed in detail, they correctly determined that it must, in fact, be the neutrinos which power the shock wave during its initial millisecond evolution (Colgate and White 1965).

Imparting energy to the shock from the neutrinos is simple in principle but involved in detail. The basic idea is that a huge reservoir of energy is locked up in neutrinos in the dense proto-neutron star. Shortly after bounce, the core effectively becomes a “neutrino star” or “neutrino lightbulb” with a neutrino photosphere. In the surrounding dense environment, neutrinos would be likely to interact and impart their kinetic energy to the stalled shock and facilitate the explosion. The energy would need to be imparted quickly as material heated by the neutrinos is liable to expand and move

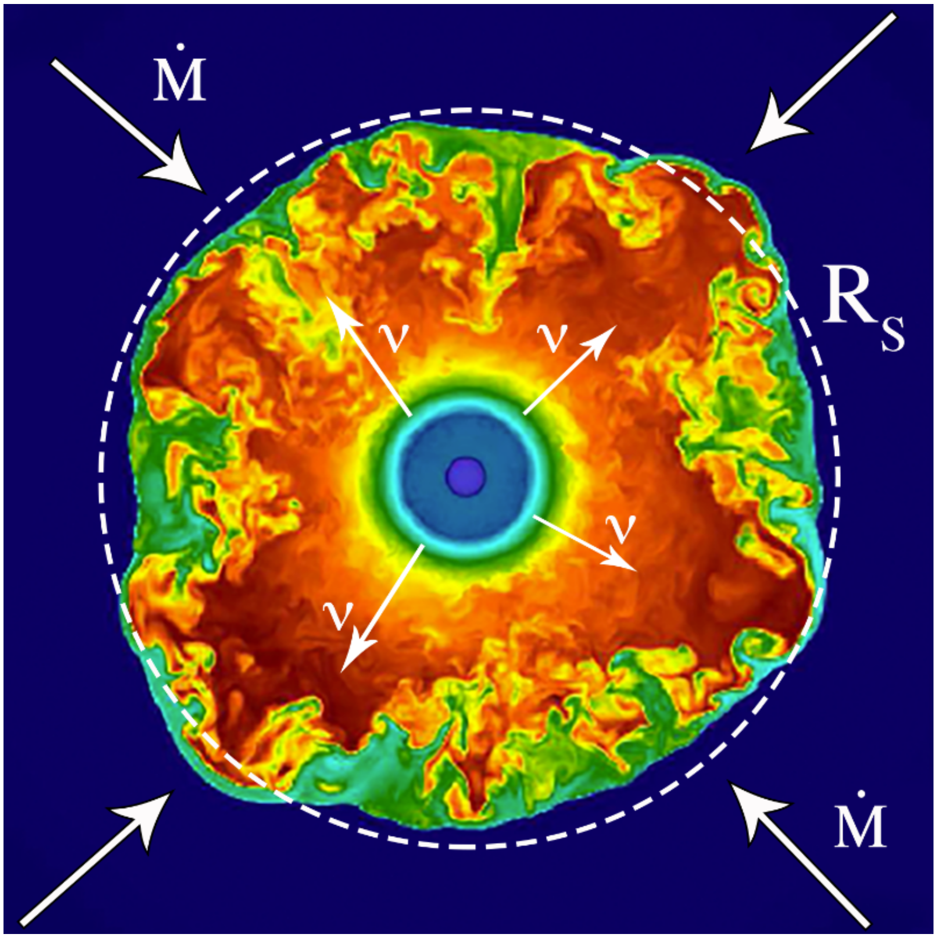

Figure 1.3 Schematic of the supernova mechanism. The core of the star bounces, giving rise to shock wave which stalls in the infalling accretion flow. Without neutrino energy deposition, material still infalling onto the proto-neutron star (represented by arrows labeled $\dot{M}$) prevents the shock from expanding and destroying the star. However, neutrinos leaving a proto-neutron star heat and impart momentum to surrounding gas. With the help of turbuelent neutrino-driven convection, energy is transported to the shock front and the stalled shock at R_s is ultimately revived leading to a supernova explosion. Background core-collapse simulation visualization, the simulation box roughly 500 kilometers on a side, 200 milliseconds after core-bounce of a 12 $M_\odot$ progenitor was kindly provided by Joshua Dolence, astro-ph/1210.5241.

away from the neutrino source. Sufficient power must be delivered to the shock by the neutrinos to power the explosion.

Near the neutrino photosphere, the star is cooling, loosing energy to "evaporating" neutrinos. At some greater radius however, neutrino evaporation is outpaced by neutrino absorption and the material is heated. The smallest possible radius at which neutrino heating is taking place is called the "gain radius" (see Janka 2012). This is smaller than the shock radius, allowing neutrinos to deposit heat behind the shock and power its expansion.

Yet even the foregoing efforts proved to not be enough. 1D spherical supernovae models still failed to explode even after including calculations of energy deposited from neutrino interactions with material behind the shock. After it was realized that convection could transport the neutrino deposited energy to the stalled shock, Wilson (1985) successfully produced an explosion. Though the finger-like instabilities which Wilson proposed likely do not occur in supernovae, heating of the fluid by neutrino absorption is thought to be a dominant power source of turbulent convection[2] which could transport energy to the shock as desired (see Burrows 2012). This has motivated a swarm of multidimensional supernovae studies (e.g. Muller et al. 2012a; 2012b; Bruenn et al. 2013; Couch & Ott 2012; Merek & Janka 2009, Couch 2013, Nordhaus et al. 2010, Hankle et al. 2012), Couch & O'Connor 2014), many of which observe that when explosions do result, they tend to be weaker (10^{50} erg) than those observed in nature. This process is summarized schematically in Figure 1.4.

The stellar explosions that we model do not include a self-consistent calculation of these processes. Ad hoc methods for exploding stars exist, such as depositing large amounts of heat or outward momentum (a piston method) in the central regions of the star. The method employed at Los Alamos is carried out in a 1D Lagragian code SASN that models collapse and bounce of the

---

[2] Note that natural instabilities in the standing shock (standing shock instability or SASI) and proto-neutron star convection, or the convection of the upper layers of the proto-neutron star due to large neutrino gradients, can also be contributing sources of turbulence.

core with a nuclear equation of state and models energy deposition due to neutrinos using a heat bomb method. Details of these calculations will be included in the next chapter.

1.3.2 Hearts of Darkness and Hearts of Antimatter

While some Pop III stars ended their lives as white dwarfs, neutron stars, or black holes, in some cases with core-collapse supernova explosions, very massive Pop III stars would have died more exotically and spectacularly. Rakavy and Shaviv (1967) proposed that stars larger than 140 solar masses die in pair-instability supernovae (PI SNe). In these scenarios, core temperatures of the star during oxygen burning exceed about a billion degrees Kelvin, and thermal photons are converted into electron-positron pairs. This robs the core of radiation pressure, causing the core to contract and its temperature to rise. Explosive oxygen and silicon burning result. Whereas less massive stars die with the collapse of their core, these stellar cores explode in a powerful nuclear explosion some 100 times more energetic than core-collapse supernovae. The energy release completely unbinds the star in a brilliant explosion. PI SNe synthesizes up to 40 solar masses of ^{56}Ni whose subsequent radioactive decay can power the luminosities of these SNe for up to 3 years (Whalen et al. 2013a). The idea of a star with a core so hot that it creates antimatter may seem like science fiction, but a few PI SN candidates have now been found in the local universe (see Pan et al. 2012b).

Previous studies have examined the visibility of $140 - 260$ $M_\odot$ Pop III PI SNe to future telescopes (e.g., Whalen et al. 2013a), but new work has shown that rapidly rotating stars can encounter the pair instability at somewhat lower masses (Chatzopoulos and Wheeler, 2012). Rapid rotation mixes the star's layers and effects homogenous nuclear fusion throughout the star. This leads to a buildup of a larger oxygen core, which can trigger the pair instability at lower stellar masses. Lower-mass Pop III stars would have been much more common than their very high mass counterparts, and so we will investigate the observability of these newly discovered SNe.

Primordial stars between about 25 and 60 $M_\odot$ may die as hypernovae (HNe). These supernovae

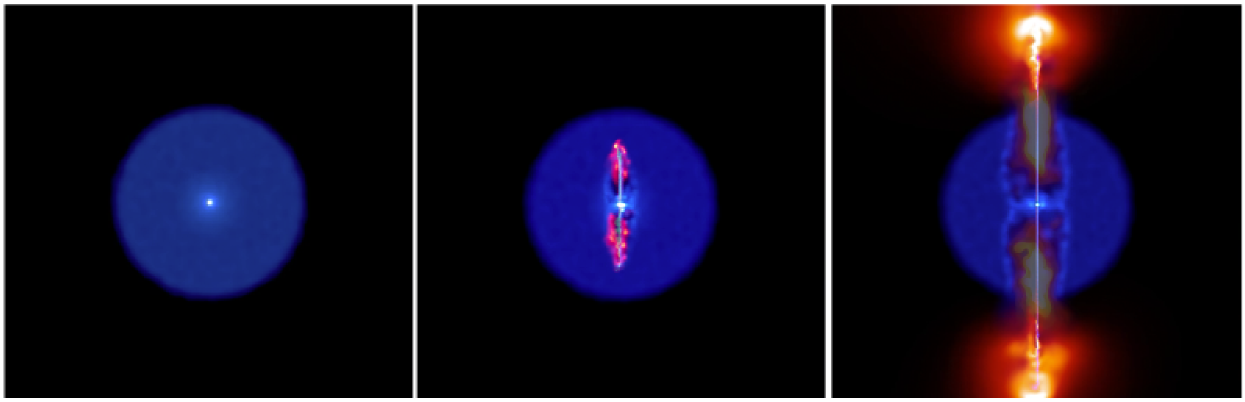

Figure 1.4 Low resolution (100,000 particle) smoothed particle hydrodynamical (SPH) hypernova simulation of a stellar explosion driven by a momentum dominated jet carried out by the author. We plot cross-sectional slices of the calculation for clarity. A black hole forms from the collapsed core which drives jets through the stellar interior. Though this calculation lacks much of the relevant physics, it illustrates the zeroth order effects. Density appears in darker, cooler hues and internal energy is overlaid in warmer colors. Though our actual radiation-hydrodynamical simulations which are used to calculate light curve are carried out in 1D (see chapter 2), we are attempting to model what may be a highly aspherical event.

were not as energetic as PI SNe but were still luminous and likely sufficiently energetic to be observed in upcoming surveys. Although HNe have been observed (e.g., Nomoto et al. 1998), their central engines are not yet well understood. A prominent model is the collapsar model (Woosley 1993), in which the core of a rapidly rotating star collapses to a black hole surrounded by an accretion disk. Rapid infall onto the black hole drives a relativistic jet into the outer layers of the star, which are still collapsing. The jet breaks through these outer layers in a highly asymmetric explosion that is very luminous along the line of sight of the jet. Fallback onto the star's newly formed and rotating "heart of darkness" powers these spectacular, beamed, events.

Finding these early cosmic explosions will open our first direct window on the primeval universe. If Pop III SNe are detected in sufficient numbers, the fact that distinct types of supernovae occur over different intervals of stellar mass could soon allow observers to determine how Pop III stars were distributed in mass. To some degree, the mass of the progenitor can be inferred from the light curve of its explosion. Primordial SN rates could also constrain star formation rates in the early universe. These events could also pinpoint the positions of primitive galaxies on the sky, especially if the galaxy is too dim to otherwise be detected. Likewise, the failure to detect Pop III SNe could imply lower star formation rates or less massive Pop III stars, either of which would also be important discoveries. The observation of Pop III supernovae by future telescopes will be a landmark achievement in astronomy in the coming years.

1.4 The Rise of Massive Black Holes

At the heart of virtually every large galaxy resides a supermassive ($M_\bullet > 10^6\,M_\odot$) black hole. Their presence in their host galaxies may be manifest in the character of the orbits of stars, in brilliant, high-energy emission near a galaxy's center, or in the presence of spectacular, kiloparsec-scale jets which can rival the extent of the host galaxy itself. Large black holes can be the brightest objects in the universe, their accretion powering ultra-luminous quasars visible from across the cosmos.

The impressive size of massive black holes bespeaks their ancient origin. The now-supermassive black holes which reside in the hearts of galaxies must have begun life much smaller in the distant past, gradually accreting material, growing through cosmic time to become the monsters observed today. The question of where they came from may initially seem straight-forward. One might assume that a very large star in the early universe ended its life with the collapse of its core, leaving behind a stellar-sized black hole ($\sim 1 - 100 M_\odot$). Such a star may have served as a *massive black hole seed* which may have subsequently accumulated material through billions of years to emerge in the modern universe as a supermassive black hole.

This intuitive origin story is fraught with its difficulties, however. If a black hole seed was born in the cataclysmic collapse of a massive star, the resulting supernova would have likely evacuated the young black hole's gas supply and the object is liable to have been "born starving." Some primordial halos may have been completely destroyed in the explosion (Whalen et al. 2012). It is further unclear on what timescale a sizeable gas supply would be available to fuel the black hole's growth. Additionally, black holes cannot[3] feed arbitrarily fast. Infalling material will heat up and radiate as it gives up gravitational potential energy and interacts with additional infalling matter. If the accretion rate becomes sufficiently large, the radiation from the infalling material will become so substantial that it will begin to impart outward momentum to the accretion flow. This pressure can ultimately impede the infall of matter onto the black hole. Thus there exists a well-defined accretion rate limit (called the *Eddington Accretion Limit*) where the rate of infalling matter and outward radiation pressure balance. Stellar-sized black holes are limited in the rate at which they

---

[3] The Eddington Accretion Limit technically applies only to spherical flows though it is applied to accreting systems indiscriminately. Thick (radiation-dominated) accretion disk theory and accompanying numerical simulations do not place a firm upper limit on accretion rates with some authors achieving rates orders of magnitude larger than that of Eddington (e.g. Jiang, Stone & Davis 2015). Nevertheless, the Eddington Limit appears to be respected in nature, by and large.

can grow even in the presence of a large gas supply.

While the above may strongly suggest the possibility of growing a supermassive black hole from a small stellar-sized black hole unlikely, data from perpetually deeper surveys render it all but impossible. In 2011, a young quasar ULAS J1120+0641, now known to the community as the *Mortlock Quasar*, was observed at redshift $z = 7.1$ (roughly 1 billion years after the Big Bang) with an estimated mass of 10^9 $\mathrm{M}_\odot$ (Mortlock et al. 2011). Subsequently the supermassive black hole in SDSS J010013.02+280225.8, a quasar observed from redshift $z = 6.1$ (about 1.2 billion years after the Big Bang) weighed in at 1.2×10^{10} $\mathrm{M}_\odot$ (Wu et al. 2015). The scenario where a stellar-sized black hole produced around redshift $z = 15$ or 500 million years after the Big Bang accretes continuously to achieve masses of $10^6 - 10^9$ $\mathrm{M}_\odot$ *cannot* explain these observations. The community has expended substantial efforts in exploring alternate pathways to massive black holes to achieve billion mass black hole by one billion years after the Big Bang.

Understanding the histories of supermassive black holes will shed critical light on processes of large-scale structure formation in general. How the universe makes very large things is still an active area of research, but the growth of massive black holes appears to intimately tied to the formation of galaxies. Cryptic but robust correlations between black hole masses and the velocity dispersions of galaxies[4] strongly suggest that massive black holes and their host galaxies have evolved together[5]. If black hole and galaxy evolution are coupled, constraining massive black hole formation can provide insight into the origins of galaxies in addition to the growth of structure throughout the cosmos.

---

[4] Velocity dispersion is defined loosely as the spread in velocities in the bulge of the galaxy. The precise definition varies from author to author, but it is universally related to the standard deviation of the line profile.

[5] One might initially suppose that the reason the velocity dispersion (which characterizes stellar speeds in the galactic nucleus) and black hole masses are correlated is that the central black hole asserts a gravitational influence on these stars. However, the central black hole constitutes only $\sim 1\%$ of the total mass of the nucleus and so its gravitational influence can be neglected. Yet the stars of the nucleus “know” about the mass of the black hole despite being gravitationally uncoupled.

Halos with masses of 10^6 $M_\odot$ are massive, but scenarios can be contrived where halos grow much larger before collapse. If a halo in the early universe was kept free from heavy elements (hereafter we will say "metals") even as surrounding halos underwent star formation, these surrounding halos could provide a background of Lyman-Werner[6] photons which could keep the metal-free halo also free of molecular hydrogen[7]. If this takes place, nothing can stop the halo from growing to a mass of $\sim 10^8$ $M_\odot$, corresponding to virial temperatures of 10,000 K. At these temperatures, the Lyman series becomes collisionally excited and the massive halo cools catastrophically through Lyman-α. The subsequent evolution of the gargantuan collapsing halo has been the subject of numerous studies (e.g. Johnson et al. 2013, Whalen et al. 2014), some suggesting that the cloud gives rise to a super-massive ($\sim 10^5$ $M_\odot$) "quasi-star" (e.g. Regan et al. 2012) which quickly (on the timescale of Myr) implodes to form a similarly massive black hole. Direct collapse of the cloud to black hole without in intermediate stage of stellar-like activity is also probable. Some studies, suggest that such a supermassive star could in rare circumstances undergo a general-relativistic instability and explode with 10,000 times the energy of canonical core collapse events. Whether such a star forms which subsequently explodes to become a black hole or whether only a black hole forms in the collapsing cloud, a very large $\sim 10^5$ $M_\odot$ black hole emerges from the process which could serve as a very effective seed for supermassive black holes observed 1 Gyr after the Big Bang.

The scenario we have just proposed is called the *direct collapse hypothesis*. Alternate scenarios have been proposed including collisional run-aways in stellar clusters (for a review see Regan et al. 2012). In each proposed process, the goal is the same: create larger black hole seeds so that the

---

[6] Lyman-Werner photons are photons with the energy required to dissociate molecular hydrogen.

[7] Note that we don't expect *ionizing* radiation to escape the star-forming halos. These will be trapped behind ionization fronts in primordial HII regions surrounding those star-forming regions. Because Lyman-Werner only dissociates molecular hydrogen and because molecular hydrogen is so rare at this point, Lyman-Werner luminosity can influence neighboring halos at a much larger range.

black hole has sufficient time to grow to sizes observed in quasars in deep surveys.

Until recently, observational evidence for objects undergoing direct collapse or for population III structures in general has been lacking. Recent surveys (Sobral et al. 2015) have brought to light some objects with characteristics strongly suggestive of these processes.

In the coming chapters, we will explore the character of the emissivity of direct collapse black holes and a subset massive population III star explosions. In both cases we will determine what signatures may be observed at high redshift and make predictions for upcoming instruments and surveys.

CHAPTER

TWO

ESTIMATING EMISSIVITY FROM ANCIENT SUPERNOVAE

> *Everyone knows that dragons don't exist. But while this simplistic formulation may satisfy the layman, it does not suffice for the scientific mind.*
>
> Stanislaw Lem

> *A [model] is a sketch, not a painting completed in full.*
>
> James E. Talmage

2.1 Supernova Light Curves: An Introduction

To understand the era of the first stars and galaxies, we need to search for the universe's most luminous events, events that might be detected nearly an entire universe ($\sim 13.5 \times 10^9$ lyr) away. Supernovae from massive first generation stars could fill this role, and we describe here our efforts to constrain their detectability to future instruments. This process involves modeling supernova blasts, constraining emission or light curves (the luminosity of the supernova as a function of time), and determining their apparent magnitudes after geometric dilution and extinction of the light.

It was worth mentioning that calculating supernova light curves has a range of applications extending far beyond modeling early universe explosions. A sizable subset of all supernova have some distinguishing characteristic in their light curves or spectrum, leading to the temptation to pigeon hole many supernovae as "special" events (see Filippenko 1997 for a review). With large all-sky surveys currently in operation and with upcoming instruments like LSST coming online soon, supernovae will soon be discovered at rates of thousands per year. With this flood of data, a means of quickly characterizing light curves will be necessary to distinguish well-understood events from those deserving of followup study. This has motivated the creation of large databases of supernova light curve calculations which can be used in an automated supernovae classification pipeline (e.g. Bayless et al. in prep). The Los Alamos Supernova Light Curve Project (Frey et al. 2013) has undertaken the modeling of local universe events including ASSAN15-lh (Chatzopolous et al. 2016, in review) and 2010jl (Wiggins et al. in prep).

A supernova "light curve" (hereafter contracted to "lightcurve") is the luminosity (power emitted in electromagnetic radiation) by a supernova as a function of time. Lightcurve shapes can vary substantially from event to event, but an idealized supernova explosion (a spherical blast into a vacuum) is expected to contain at least the following features (see Figure 2.1).

1. *Shock breakout:* a very brief, high-luminosity, high-energy pulse of light corresponding to the time when the supernova shock bursts through the photosphere of the star. This event takes place on the timescale of the light cross time of the star and is rarely observed.
2. *Expansion and Cooling:* The supernova remnant subsequently expands and cools due to both adiabatic expansion and the loss of energy from radiation escaping the thinning medium.

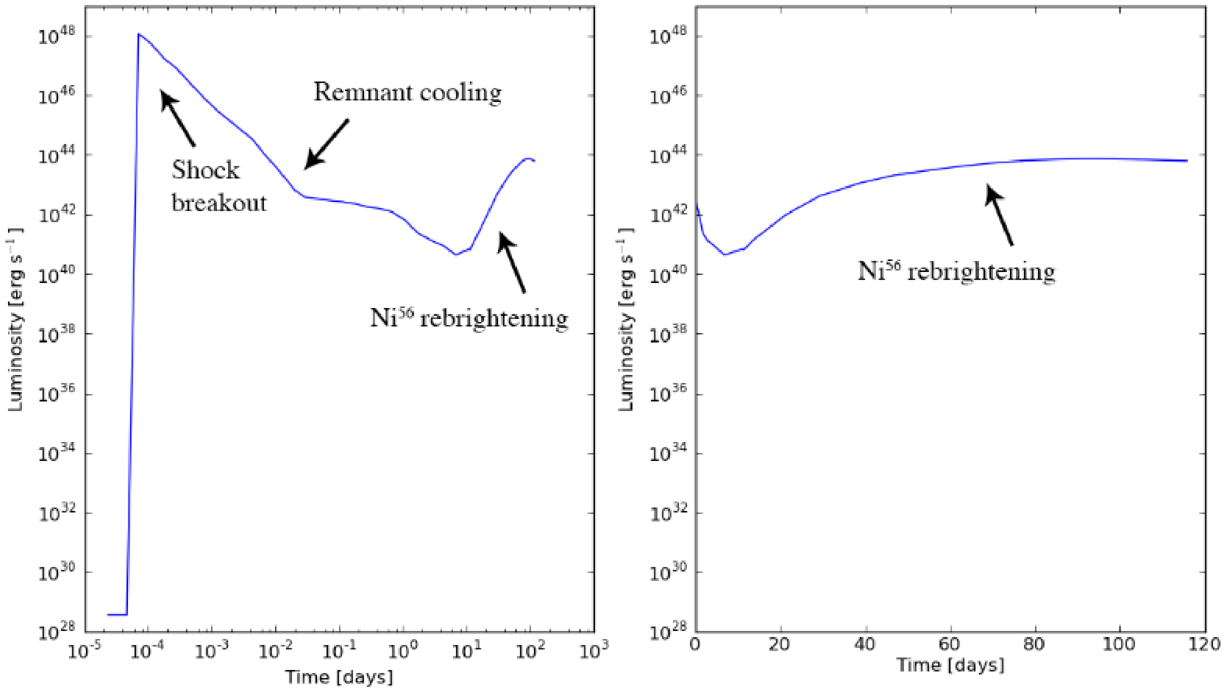

Figure 2.1 A "vanilla" lightcurve from the Los Alamos Supernova Lightcurve Project with several features labeled plotted in log Time (left panel) and linear time (right panel). One immediately observes that ^{56}Ni rebrightening dominates the majority of the timescale of the transient while shock breakout disappears on the timescale of minutes to hours.

3. *Nickle-56 rebrightening:* supernova light curves are powered at late times by β^+ decay of Nickle-56 (^{56}Ni)[1]. This results in the emission of a gamma ray. This energy serves to not only heat the supernova remnant, but as the supernova becomes optically thin, these rays become an important source of light.

Additional components to a supernova light curve might exist, including features related to pre-supernova outbursts or shock heating the circumstellar material. We explore the effects of these processes of lightcurve morphology later in this chapter.

---

[1] The decay is given by

$$^{56}\mathrm{Ni} \rightarrow ^{56}\mathrm{Co} + e^+ + \nu_e + \gamma$$

.

A number of codes for modeling supernova emission in the literature including SuperNU (Wollaeger & van Rossum 2014) and SEDONA (Kassen et al. 2006) calculate the lightcurve assuming the supernova remnant is homologously expanding or in a free expansion phase of sorts. For all emission taking place after shock breakout for supernovae expanding into a vacuum, this approach is appropriate. The methods just mentioned calculate emission in multiple dimensions via a Monte Carlo transport scheme. Implicit in these models is the assumption that radio-active decay of ^{56}Ni is the dominant source of power in light curves. Approaches such as those taken above, effectively separate radiation from the hydrodynamics which is appropriate for the model the authors have adopted. The Los Alamos Supernova Lightcurve Project brings several assets to the table for modeling these events. These are described in detail in section 2.

There are events,however, that cannot be modeled with the free expansion assumption, including the moment of shock breakout. In this event, a second source of energy for the supernova is manifest, namely shock heating. As the supernova shock travels through the star, light becomes trapped behind the shock adding a source of radiation pressure to the flow. When the shock reaches the photosphere, two effects take place simultaneously: (1) as the shock bursts into the stellar atmosphere a fraction of the photons which were previously trapped behind the shock stream free and (2) the shock accelerates in the diffuse medium, which is heated and begins to glow. The combined effect is a pulse of light that signals shock breakout. The reader will note that capturing the effect requires modeling the radiation field *and* the hydrodynamics as the two decouple and operate as separate entities in the event. A very similar argument can be formed regarding the modeling emission of supernova remnant shocks in the circumstellar medium. Only radiation hydrodynamics can address this problem, and our method, detailed in section 2 below, employs such a scheme. We combine these radiation hydrodynamics methods with a post-processing code to calculate a detailed (14,900 point) spectrum by solving the equation for radiative transfer with the LANL OPLIB database (Magee et al. 1995). The details of this process are including in the

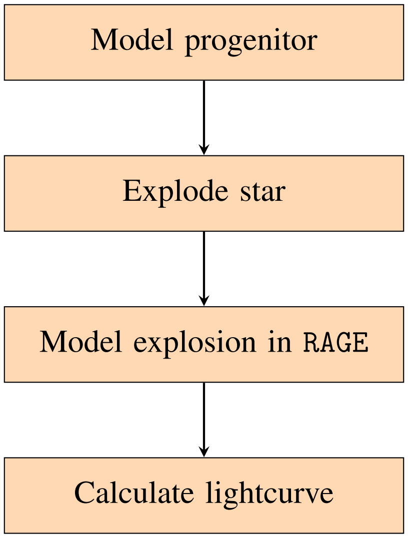

Figure 2.2 General lightcurve pipeline of the Los Alamos Supernova Light Curve Project. This pipeline is adapted to the nature of the explosions to be modeled (see text and cross reference Figure 2.13).

next section.

2.2 Computational Tools

Modeling supernova light curves for the Los Alamos Supernova Light Curve Project is multi-stage endeavor, utilizing several codes and collaborations (see Figure 2.2). Los Alamos light curves provide detailed spectra from opacity data, which is a strong function of material composition. Full stellar evolution codes including Kepler (Weaver et al. 1978) or MESA (Paxton et al. 2013) are required to calculate composition, temperature, density and radial velocities as a function of radius. These stellar progenitors are provided by collaborators. These stars are evolved up until the onset of collapse where they are mapped into Chris Fryer's code SASN (Young & Fryer 2007), a Lagrangian hydrodynamics code which includes a scheme for depositing energy from neutrino absorption. This energy deposition is the trigger for exploding the star. The stellar profile is then mapped into `RAGE`, a radiation hydrodynamics code to evolve the explosion of the star and its transition to a supernova remnant. Data dumps created by `RAGE` are subsequently post-processed to determine supernova lightcurves. We discuss some of the relevant modeling tools and stages below.

2.2.1 `RAGE`

`RAGE` (Radiation Adaptive Grid Eularian) is an adaptive mesh refinement (AMR) radiation hydrodynamics code developed at Los Alamos (Gittings et al. 2008). `RAGE` couples a 2nd order Godonov scheme to gray or multi-group flux-limited radiation diffusion and tracks multiple mass fractions per cell. The code allows ions, electrons and radiation to assume different temperatures (a so-called “3T” scheme), though our calculations are carried out in 2T (with matter and radiation being allowed to decouple). This multi-temperature capability is utilized in modeling key supernovae events including shock breakout, as we shall discuss below. The full, 3-temperature radiation hydrodynamics model is `RAGE` has the form:

$$
\begin{aligned}
\frac{\partial}{\partial t}\rho + \nabla\cdot\rho\mathbf{u} &= 0 && (2.1)\\
\frac{\partial}{\partial t}\rho\mathbf{u} + \nabla\cdot(\rho\mathbf{u}\otimes\mathbf{u} + \mathsf{P}_e + \mathsf{P}_i) + \frac{1}{3}\nabla E_r &= 0 && (2.2)\\
\frac{\partial}{\partial t}\rho E + \nabla\cdot(\rho E\mathbf{u} + \mathsf{P}\cdot\mathbf{u}) &= c\sigma_a(E_r - aT_e^4) - \frac{1}{3}\mathbf{u}\cdot\nabla E_r && (2.3)\\
\frac{\partial}{\partial t}\rho e_i + \nabla\cdot(\rho e_i\mathbf{u}) + \mathsf{P}_i : \nabla u &= \gamma_{ei}(T_e - T_i) && (2.4)\\
\frac{\partial}{\partial t}\rho e_e + \nabla\cdot(\rho e_e\mathbf{u}) + \mathsf{P}_e : \nabla u &= -\gamma_{ei}(T_e - T_i) + c\sigma_a(E_r - aT_e^4) && (2.5)\\
\frac{\partial}{\partial t}E_r + \frac{4}{3}\nabla\cdot(\mathbf{u}E_r) - \nabla\cdot\left(\frac{c}{3\kappa}\nabla E_r\right) &= -c\sigma_a(E_r - aT_e^4) + \frac{1}{3}\mathbf{u}\cdot\nabla E_r - \kappa c E_r && (2.6)
\end{aligned}
$$

where $\rho, \mathbf{u}, E$ are fluid density, velocity and specific total energy, $\mathsf{P} = \mathsf{P}_e + \mathsf{P}_i$ is the fluid pressure with P_e and P_i being the electron and ion pressures respectively, E_r is the frequency-averaged radiation energy density, e_i, e_e are the ion and electron specific internal energies, T_i, T_e are the ion and electron temperatures, and κ is opacity.

The first three equations in the model are Euler's equations for fluid dynamics, which are statements of mass, momentum and total energy conservation. Equations (2.4) and (2.5) evolve the internal energies or temperatures of the ions and electrons separately and (2.6) evolves the energy density of the radiation field E_r under the assumption that radiation propagates through diffusion, an approximation which is acceptable in optically thick regimes.

When first encountered, equations (2.1) – (2.6) may appear dense, so we motivate their form with a brief introduction to radiation hydrodynamics. We expect a fluid to conserve mass, momentum and energy. Suppose we divide a volume into a number of discrete cells or zones. To maintain, say, mass conservation, we expect that the amount of matter in a cell changes in accordance with the amount of matter flowing into or out of that volume. Mathematically we say, e.g.

$$\frac{d}{dt}\int_V \rho \, dV = -\int_\partial \rho \mathbf{u} \cdot d\mathbf{A},$$

where ρ and $\mathbf{u}$ are fluid density and velocity as before. In other words, we say that the rate of change of mass m in a given volume V ($m = \int_V \rho \, dV$) is equal to the flow of material over the boundary ∂. Applying Stoke's Theorem allows us to change the surface integral on the right hand side into a volume integral, i.e.

$$\frac{d}{dt}\int_V \rho \, dV = -\int_V \nabla \cdot (\rho \mathbf{u}) \, dV,$$

Because we expect that this will hold for every cell or every dV, we drop in the integration symbols to arrive at the first of Euler's equations,

$$\frac{d}{dt}\rho + \nabla \cdot (\rho \mathbf{u}) = 0. \tag{2.7}$$

A similar argument can be made for the momentum equation. The total momentum p in a given volume is

$$p = \int_V \rho \mathbf{u} \, dV,$$

and momentum changes in a volumes changes according to the amount of momentum entering or leveling the volume, i.e.

$$\frac{d}{dt}\int_V \rho\mathbf{u}\,dV = -\int_\partial \rho\mathbf{u}\otimes\mathbf{u}\cdot d\mathbf{A},$$

which gives

$$\frac{d}{dt}\rho\mathbf{u} + \nabla\cdot(\rho\mathbf{u}\otimes\mathbf{u}) = 0.$$

This conservation law is not complete, however. The time derivative of momentum is force, so we expect that fluid forces will appear on the right-hand-side of this conservation law. The momentum equation includes gradients of pressure. This is demonstrably a force because the force due to pressure F_p is

$$F_p = \int_\partial P\,d\mathbf{A},$$

which, as a volume integral is

$$F_p = -\int_V \nabla P\,dV.$$

We include this force in the momentum equation with

$$\frac{d}{dt}\rho\mathbf{u} + \nabla\cdot(\rho\mathbf{u}\otimes\mathbf{u}) - F_p = 0.$$

or

$$\frac{d}{dt}\rho\mathbf{u} + \nabla\cdot(\rho\mathbf{u}\otimes\mathbf{u}) + \nabla P = 0. \tag{2.8}$$

It is worth noting here that if the fluid experiences additional forces, these would also be included here. Indeed, the extra term ($\frac{1}{3}\nabla E_r$) in (2.2) is such a force from gradients in radiation pressure, but we discuss this term in detail when we introduce `RAGE`'s simplified radiation hydrodynamics model. Also note that in this derivation, we have assume that pressure is a *scalar*. In general, pressures may be rank-2 tensors and are represented in three dimensions as 3×3 matrices. The pressures P_i in equations (2.1) – (2.6) are tensors[2]. We can represent our *scalar* pressure in tensoral

---

[2] We represent tensors here in san seriff font.

form by $\mathsf{P} = P\mathsf{I}$ for identity matrix I. The allows us to reproduce forms of the Euler equations which closer resemble those in the `RAGE` model.

The Euler conservation law for energy (2.3) is less trivial to derive, but the interested reader can consult chapter 2 of Castor (2003). In summary, Euler's equations take the form

$$\begin{aligned} \frac{\partial}{\partial t}\rho + \nabla \cdot (\rho \mathbf{u}) &= 0, && (2.9) \\ \frac{\partial}{\partial t}\rho \mathbf{u} + \nabla \cdot (\rho \mathbf{u} \otimes \mathbf{u} + \mathsf{P}) &= 0, && (2.10) \\ \frac{\partial}{\partial t}\rho E + \nabla \cdot (\rho E \mathbf{u} + \mathsf{P} \cdot \mathbf{u}) &= 0. && (2.11) \end{aligned}$$

We now proceed to discuss the two-temperature matter model in `RAGE` which is represented in equations (2.4) and (2.5) above. The left-hand side of (2.4) and (2.5) resembles equation (2.3) as these equations describe the evolution of energy in the electrons and ions. The right-hand side of both equations include a term of the form $\gamma_{ei}(T_e - T_i)$ which acts to be bring electron and ion temperatures into equilibrium. An analogous term appears in equation (2.5), $c\sigma_a(E_r - aT_e^4)$ which acts to bring the "temperature" of the radiation and the temperature of the electrons into agreement. As expected, a corresponding term appears in (2.6).

The `RAGE` model maintains that a temperature difference between the radiation field and the protons will be communicated by an equilibration between the radiation and the electrons first after which the joint population of electrons and the radiation field will equilibrate with protons. This is seen by observing that the protons and electrons are coupled with the radiation field being coupled only to the electrons. While this model is more general than single temperature prescriptions, we still only describe the energy distribution of electrons, ions and spectrum of radiation with temperatures. This is acceptable in optically thick regimes where collisions are expected to dominate and thermalize each species. The reason the 3T prescription works in the optically thick regime is that it is expected that electrons and ions will thermalize with themselves before thermalizing with the other populations due to the mass difference: it requires many collisions with a electrons for massive ions to change substantially in energy. When the medium becomes optically thin, ions and electrons may take on much more complex energy distributions than those which can be characterized by a single temperature. The model assumes that the medium in question is sufficiently optically thick that the respective energies of ions, electrons and photons can be described with Maxwell-Boltzmann distributions.

We now attempt to justify the form for the last equation in our model which follows the evolution of the radiation field E_r. The equation of radiative transport is

$$\frac{1}{c}\frac{\partial I_\nu}{dt} + \mathbf{n}\cdot\nabla I_\nu = \varepsilon - \kappa I \tag{2.12}$$

where I_ν is the intensity of the radiation field at frequency ν, and ε and κ is the local emissivity and opacity respectively. We recall that the energy density in radiation E_ν is

$$E_\nu = \frac{1}{c}\int_{4\pi} I_\nu d\Omega,$$

and that

$$\mathbf{F}_\nu = \int_{4\pi} \mathbf{n} I_\nu d\Omega,$$

and that

$$\mathsf{P}_\nu = \frac{1}{c}\int_{4\pi} \mathbf{n}\otimes\mathbf{n} I_\nu d\Omega,$$

where $\mathbf{F}$ and P are the flux and radiation pressure respectively. We now take two moments of the radiative transfer equation which is carried out by iteratively multiplying terms by 1 and $\mathbf{n}$ and then integrating over solid angles Ω. We obtain

$$\frac{\partial E}{\partial t} + \nabla\cdot\mathbf{F} = 4\pi\varepsilon - \kappa c E \tag{2.13}$$

$$\frac{\partial}{\partial t}\mathbf{F} + c\nabla\cdot\mathsf{P} = -\kappa\mathbf{F}, \tag{2.14}$$

where we have suppressed the frequency dependence of the variables. If we take higher moments *ad inifitum*, one runs into the trouble that they always have one fewer equations than unknowns.

Some prescription for P is necessary to close the equations. In our case, we use the Eddington approximation, which requires that the radiation pressure be everywhere isotropic, i.e.

$$\mathsf{P} = \frac{1}{3}E\mathsf{I},$$

where I is again the identity. With this in hand, equations (2.13) and (2.14) are equivalent to

$$\frac{\partial E}{\partial t} + \nabla\cdot\mathbf{F} = 4\pi\varepsilon - \kappa c E \tag{2.15}$$

$$\frac{\partial}{\partial t}\mathbf{F} + \frac{c}{3}\nabla E = -\kappa\mathbf{F} \tag{2.16}$$

where the emissivity term in equation (2.16) has integrated to zero. In one formulation of the diffusion approximation, we set $\frac{\partial}{\partial t}\mathbf{F} = 0$ in equation (2.16). This approximation, that the rate of change in flux density $\mathbf{F}$ would immediately imply that

$$\mathbf{F} = -\frac{c}{3\kappa}\nabla E.$$

This can be substituted into (2.15) to yield a single equation for radiative transport in the diffusion limit

$$\frac{\partial E}{\partial t} - \nabla\cdot\left(\frac{c}{3\kappa}\nabla E\right) = 4\pi\varepsilon - \kappa c E. \tag{2.17}$$

The term of the form $\nabla\cdot(\mathbf{u}E_r)$ on the left hand side in equation (2.6) is an advection term, accounting for the amount of energy in radiation which leaves a given zone due to flow of the fluid. The factor of $\frac{1}{3}\mathbf{u}\cdot\nabla E_r$ on the right hand side of equation (2.6) and (2.3) is the amount of work done on the fluid by the radiation field.

One may wonder why the terms $4\pi\varepsilon$ which appears in equation (2.17) do not appear in (2.6). The term $4\pi\varepsilon$ is a source term, meaning it characterizes how much radiation field is added by the gas. In LTE, this emissivity is $c\sigma_a a T_e^4$, which appears in the `RAGE` model.

2.2.2 SPECTRUM

`RAGE` does not contain the capability to estimate emission from a simulation domain self-consistently. One-dimensional supernovae calculations carried out in `RAGE` must be post-processed to estimate supernova luminosity as a function of time.

While emissivity could be estimated by assuming radial transfer of light through the star (see the following subsection), the effects of limb darkening and processes giving rise P-signi profiles[3] in the stellar/supernova spectrum cannot be captured without a multidimensional model. To process the 1D `RAGE` data with `SPECTRUM`, the data are fanned into a 2D half-disk domain with azimuth-spacing uniform in $\mu = \cos\theta$ (see Figure 2.3). This partition of the spherical domain is convenient as individual cells which represent rings of stellar material when revolved around the x-axis each contain equal volume at a given radius. This may be demonstrated explicitly by representing volume V of the ring as a volume integral, e.g.

$$\begin{aligned} V &= \int_0^{2\pi} \int_{\theta_i}^{\theta_{i+1}} \int_{r_i}^{r_{i+1}} r^2 \sin\phi \, dr \, d\phi \, d\theta \\ &= \int_0^{2\pi} \int_{\cos^{-1}\mu_i}^{\cos^{-1}\mu_{i+1}} \int_{r_i}^{r_{i+1}} r^2 \sin\phi \, dr \, d\phi \, d\theta \\ &= \frac{2\pi}{3}(r_{i+1}^3 - r_i^3)(\mu_i - \mu_{i+1}) \end{aligned}$$

where the quantity $(\mu_i - \mu_{i+1})$ is constant for any choice of i by construction. It follows that for any fixed radial partition bounded by r_i and r_{i+1}, the volume of the ring and its mass is constant. Note also that it also follows immediately that the outward surface area is also constant for cells at a given radius. These properties render this angular partition convenient for calculating emission as we shall see below.

In `SPECTRUM` we assume local thermodynamic equilibrium (LTE) and that Kirchoff's law holds, i.e., that the amount of luminosity entering a small volume is equal to the amount leaving it. The

---

[3] P-signi profiles are line profile shapes arising from expanding or contracting shells of material. Such effects can only be recovered in two or three dimensions.

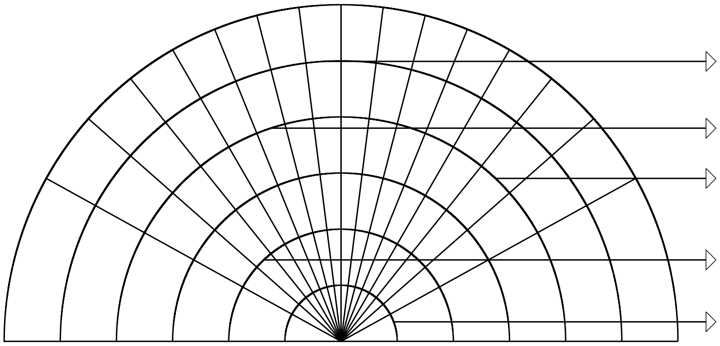

Figure 2.3 Schematic of `SPECTRUM` grid. The domain is partitioned uniformly in $\mu = \cos\theta$ so that each cell (which represents a ring of material when rotated about the x-axis) contains equal volume and hence equal mass. Arrows indicate the direction of radiation propagation to a viewer situated at some large positive x.

source function S_ν takes the form

$$S_\nu = B_\nu, \tag{2.18}$$

where B_ν is the Planck function and the total emissivity of a parcel of fluid of mass m being

$$j_\nu = m\kappa_\nu B_\nu, \tag{2.19}$$

for absorption opacity $\kappa_n u$.

The radiation will be attenuated as it passes through the supernova remnant. Optical depth $\tau_\nu = \sum_i \rho_i \kappa_{\nu,i} \Delta x_i$ for a given cell is summed along rays parallel to the x-axis and diminished by a factor of $e^{-\tau}$. This process is carried out for each cell and accumulated as a function of wavelength to construct a spectrum for the snapshot in question. Doppler effects that shift emission in frequency space between radial layers of the supernova remnant are also taken into account. `SPECTRUM` uses LANL OPLIB opacities to create a 14,900 point spectrum for each data dump (see Figure **??**) which is integrated over energy to compute the lightcurve.

`SPECTRUM` operates under several assumptions. One of the more apparent is the assumption of LTE which is not expected to be good out to late times when the remnant becomes diffuse. As a

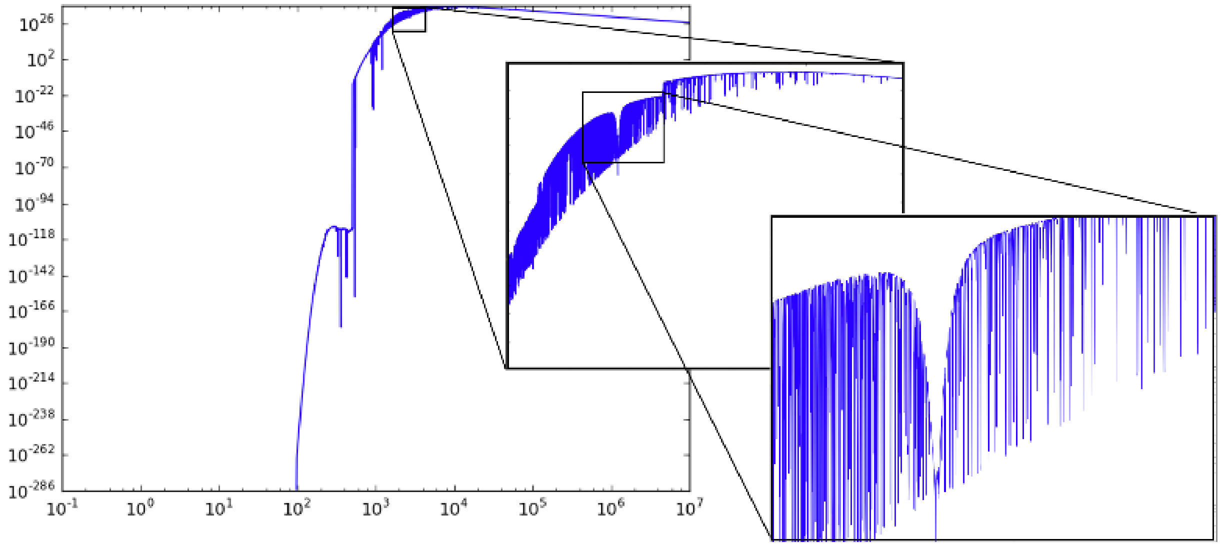

Figure 2.4 `SPECTRUM` and AURORA both calculate 14,900 point spectra for each `RAGE` data dump. This figure demonstrates the resolution offered in such an approach. This spectrum is generated from a lightcurve calculation of a supernova in a dense, metal-rich circumstellar shell carried out by AURORA. The complex line structure is captured in exquisite detail.

corollary, `SPECTRUM` cannot account for non-LTE processes giving rise to emission, e.g., plasma effects, recombination emission or synchrotron emission. Another perhaps more subtle but important point is that `SPECTRUM` also assumes that all the emission of a given fluid parcel is directed toward the observer (see Figure 2.3). In some rare instances this can cause the algorithm to predict *limb-brightening* as opposed to *limb-darkening*, the latter being expected. Most importantly, the algorithm assumes that supernova emission is dominated by *volume* emission, i.e., that the medium is everywhere optically thin. It is easy to see that `SPECTRUM` recovers trivially the solution to the equation of radiative transfer in the optically thin case. The solution to the equation of radiative transfer without scattering over an optical depth τ where $S_\nu = B_\nu$ and ρ are constant is

$$I(\tau) = I(0)e^{-\tau} + (1 - e^{-\tau})B_\nu. \tag{2.20}$$

For small τ, we Taylor-expand and approximate $e^{-\tau}$ as $1-\tau$. This gives us

$$I(x_1) \approx B_\nu \tau = B_\nu \kappa_\nu \rho \Delta x, \tag{2.21}$$

where we have assumed ρ is constant over arclength Δx and have adopted $\Delta x = x_1 - x_0$. Integrating (2.21) over surface area and solid angle gives the expected luminosity L over some volume $V = \Delta x \Delta y \Delta z$ with emissivity B_ν and density ρ, i.e.

$$L = \pi B_\nu \kappa_\nu \rho_n u V = \pi B_\nu \kappa_\nu m, \tag{2.22}$$

the factor of π coming from Lambert's cosine law in the solid angle integration. We have also assumed that $I(0) = 0$, as we are currently only considering the luminosity of a single cell. This corresponds precisely to the emissivity calculated by `SPECTRUM` (c.f. equation(2.19)). However, if τ is large, equation (2.20) approaches

$$I(x_1) = B_\nu, \tag{2.23}$$

which is given in units of power per unit solid angle per unit surface area, which implies the presence of surface emission. `SPECTRUM` at present contains no terms for surface emission which become important in the optically thick limit.

Finally, `SPECTRUM` assumes instantaneous transfer of emission through the simulation domain. This naturally breaks down with large domains and features in supernova light curves very sensitive to the radius of the star, including the duration of shock-breakout which must at least be as long as the light-crossing time of the star, are not captured.

`SPECTRUM`'s systematic calculation of emission is also somewhat expensive. The number of operations in `SPECTRUM` scales roughly like the number of radial zones multiplied by the number of angular bins chosen for the `SPECTRUM` grid. This in part motivated the creation of *RainbowDash*, a python wrapper around `SPECTRUM` which takes `RAGE` dumps and attempts to reduce the number of radial cells before `SPECTRUM` is called. `SPECTRUM` calculations remain costly, however, with CPU hours which rival the total cost of the `RAGE` runs themselves. Fortunately, the calculation is stupidly parallel, allowing SPECTRUM runs to be carried out in days where full RAGE runs require weeks to months. Code comparisons of SPECTRUM with competing codes (e.g. FLASH, STELLA, SuperNu) motivated the creation of a code to cross-check SPECTRUM results and to improve upon some of its aspects. We discuss the philosophy of my transfer code AURORA in the next subsection.

2.2.3 AURORA

While RAGE and SPECTRUM are LANL code bases which have been employed in the Los Alamos Light Curve Project, AURORA was written by the author as part of this dissertation.

The equation for radiative transfer without scattering in terms of optical depth τ is

$$\frac{dI_\nu}{d\tau} = S_\nu - I_\nu, \tag{2.24}$$

for intensity I at frequency ν and source function S. In spatial coordinates we have

$$\frac{dI_\nu}{dx} = \kappa_\nu \rho S_\nu - \kappa_\nu \rho I_\nu, \tag{2.25}$$

where κ and ρ are the opacity and density respectively. Assuming the rays are radial and that spherical symmetry and Kickoff's Law obtain, we can integrate over surface area and solid angle to obtain a corresponding expression for the luminosity (e.g. Hatchett, Buff & McCray 1976), i.e.

$$\frac{dL_\nu}{dr} = -\kappa_\nu \rho L_\nu + 4\pi^2 r^2 B_\nu \kappa_\nu \rho, \tag{2.26}$$

where $B_\nu \kappa_\nu \rho$ is the emissivity per unit volume. Note the extra factor of π from Lambert's cosine law from the solid angle integration. We wish to integrate this over some $\Delta r = r_2 - r_1$. With appropriate choice of integration factor ($\mu = e^{\int \kappa_\nu \rho dr}$), it is easy to show that

$$\begin{aligned} L(r_2) &= L(r_1) e^{-\kappa_\nu \rho (\Delta r)} \\ &+ 4\pi^2 B_\nu \Pi(\Delta r, \kappa_\nu, \rho), \end{aligned} \tag{2.27}$$

with

$$\begin{aligned}\Pi(\Delta r,\kappa_\nu,\rho) &= r_2^2-\frac{2r_2}{\kappa_\nu\rho}+\frac{2}{(\kappa_\nu\rho)^2} \\ &- e^{-\kappa_\nu\rho(\Delta r)}\left[r_1^2-\frac{2r_1}{\kappa_\nu\rho}+\frac{2}{(\kappa_\nu\rho)^2}\right].\end{aligned} \tag{2.28}$$

Note that this solution is the *exact* luminosity of spherical shell with luminosity at the lower boundary $L(r_1)$ assuming ρ, T, κ are constant over the radial zone. Higher order schemes where do not assume these variables are constant can be easily constructed if one is, for instance, running a `data_binned.txt` profile in which information has been lost and a type of interpolation over these quantities is needed. In many cases, one can integrate a simpler expression based on the formal solution to the equation of radiative transfer which assumes $4\pi r^2$ is constant over the zone if the size of a radial zone at r is small compared to the curvature of the $r+1$th sphere, i.e. one can solve a simpler expression

$$L(r_2)=L(r_1)e^{-\kappa_\nu\rho(\Delta r)}+4\pi r_2^2B_\nu(1-e^{-\kappa_\nu\rho(\Delta r)}), \tag{2.29}$$

e.g. Hatchett, Buff & McCray (1976). When logarithmic spacing is used, this is *not* the case and such schemes will systematically over predict luminosity in optically thin problems. In the case of supernova light curve calculations, either equation (2.27) is recommended or a scheme which iteratively divides thick shells to maintain small $\Delta r/r$.

Equation (2.27) has several pleasing properties. One observes that in the case of optically thick media, we recover $L(r_2)=4\pi^2B_\nu r_2^2$ which when integrated over all frequencies is $4\pi r^2\sigma T^4$ as required. By neglecting terms of second and higher order and noting that $e^{-\tau}\approx 1-\tau$ for small τ, one can also discern a recovery of the expected emission in the optically thin limit. An additional point is that (2.27) can be used recursively to calculate the luminosities of spherically symmetric data. Such integration strategies need only visit each radius once. This leads to remarkable speed ups in spherical light curve calculations. A 14,900 point spectrum of 150 `RAGE` dumps requires

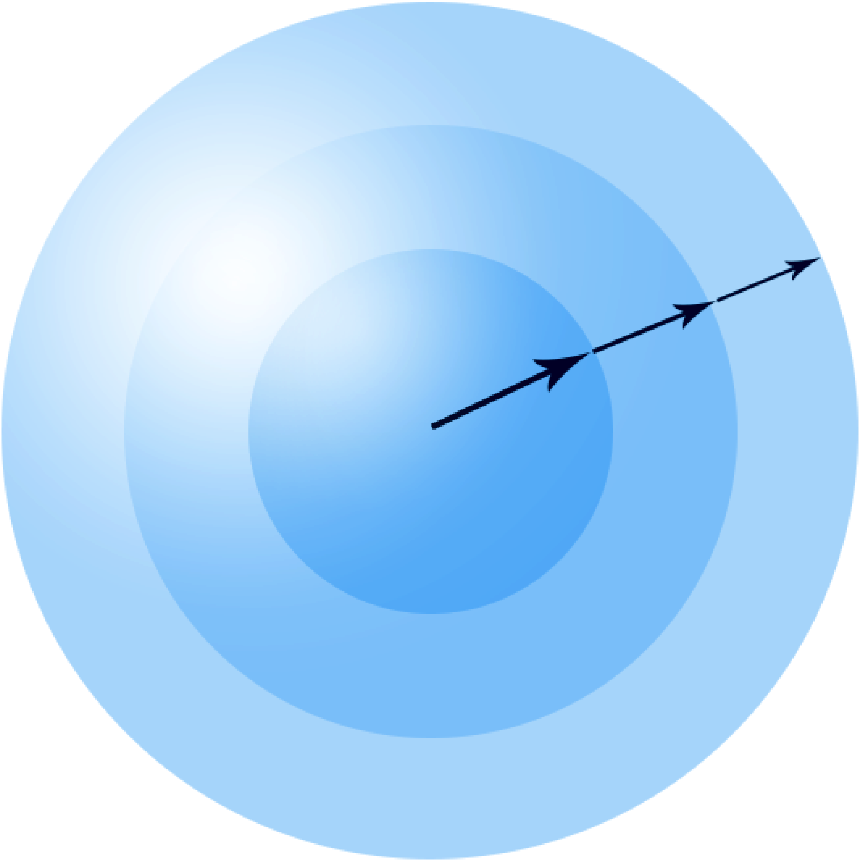

Figure 2.5 Schematic of spherical AURORA grid. Black arrows indicate transferring radiation. The equation for radiative transfer is solved in spherical geometry; a single 14,900 group spherical "ray" is propagated from the center of the domain to large radius under the assumption that light propagates radially. Because the equation for radiative transfer is used, AURORA trivially recovers surface emission in the optically thick limit.

only about an hour on a single processor. This figure includes time used in setting up the grid, reading in RAGE dumps and opacity tables and writing output spectra.

This method has drawbacks. The effects of limb darkening, P-signi profiles, etc. are not included when constructing spectra or calculating bolometric luminosity of explosion events. One would use this option with the good assumption that such effects do not contribute meaningfully to the total luminosity of the supernova explosion. These effects can be recovered through use of an additional option which still must faster than a traditional SPECTRUM calculation or one my resort classic SPECTRUM if desired. We again emphasize that the total luminosity of the light curve is still calculated by summing up energy bins in the calculated spectrum as was done in SPECTRUM.

One will notice that (2.27) contains factors of $\kappa_\nu \rho$ in denominator positions which become cumbersome to deal with numerically. In particular, in optically thin regimes one will be subtracting very large numbers and face associated difficulties there. In practice, the geometric coefficient $4\pi r^2$ is lagged but checks are implemented in the code to determine if $\Delta r/r$ is large. If this is the case, lagging the $4\pi r^2$ coefficient could lead to the growth of unacceptable errors, in particular, in over-estimating luminosity from a given shell. When $\Delta r/r > \varepsilon$ the cell is sub-divided until each $\Delta r/r \leq \varepsilon$ for user-chosen ε.

This discretization of the equation for radiative transfer is almost entirely independent of the formalism which appears in Frey et al. (2013), minus the use of identical opacities. This provides an opportunity for code comparison and a means to cross-check SPECTRUM calculations.

AURORA inherits some shortcomings of SPECTRUM including the assumption of instantaneous transfer of radiation and LTE. In addition, AURORA cannot produce the geometric effects modeled by SPECTRUM including P-signi effects and limb-darkening (when AURORA is used in 1D). Nevertheless, AURORA offers substantial speed ups over SPECTRUM for similar accuracy which may render it a useful tool for lightcurve calculation.

Basic Code Design

AURORA is a very small code (< 1000 lines) written in `C` and `Fortran`. In this section, we briefly describe AURORA's code structure and function. The general code process is summarized schematically in Figure 2.6.

Both `SPECTRUM` and AURORA use Los Alamos National Laboratory OPLIB opacities to calculate spectra. Each binary table corresponds to a given element with opacities varying as a function of gas density, temperature and frequency. Frequencies are defined for temperatures and densities given in arrays included in the dataset, i.e., `dlist` and `tlist`. The first object of the code is to read in these opacity tables. `SPECTRUM` must read the opacity data for each data dump which is processed. In AURORA, which is coded to accept multiple files simultaneously, all opacity data is read in at the beginning of a calculation, and no further reads are required through the entirety of the light curve calculation. This alleviates former performance struggles of `SPECTRUM`, when multiple instances of `SPECTRUM` may have been running and simultaneously attempting to access the same data address.

Following reading the catalogs, the `data_binned.txt` files are opened for post-processing in serial. The `data_binned.txt` files contain the density, radial velocity, temperature and composition information for the supernova remnant at a given time as a function of radius. For each radial zone, the indices m_ρ, k_T which are defined such that

$$T = \texttt{tlist}[k_T],$$

$$\rho = \texttt{dlist}[m_\rho],$$

which we have used equality loosely here to indicate that we find the indices in the arrays `dlist` and `tlist` corresponding to the temperature and density in a given cell. To accomplish this quickly we use an ordered search scheme from Press et al. (2012). Note again that these indices are determined *prior* to calculating emission, another walltime-saving step which is not carried out in

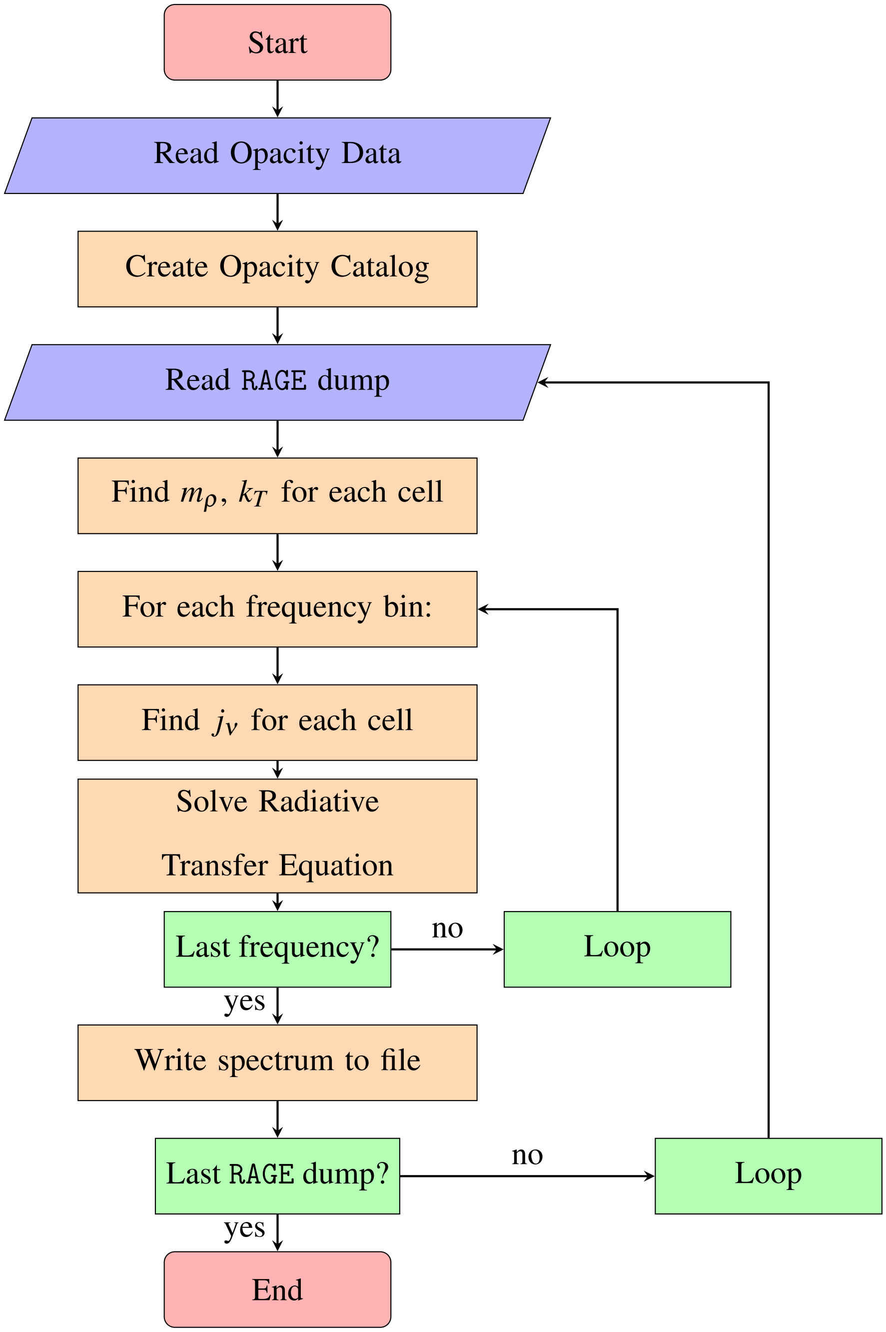

Figure 2.6 Code diagram for AURORA. The code is capable of processing multiple `RAGE` dumps with a single execution, reading in binary opacity data only once per light curve (see text).

`SPECTRUM`.

Unfortunately, the chosen frequency bins in the opacity data are not consistent over temperature. In particular, as temperature increases, the frequency bins shift to higher energies to capture interesting characteristics in the opacity data. The dependence of frequency structure on temperature is given by a simple, piece-wise linear function which is found in `SPECTRUM`. In AURORA, however, we build a `catalog` array which returns the index i in a given opacity data set corresponding to the frequency of interest ν and the gas temperature T so that

$$i = \texttt{catalog}[j_\nu][k_T],$$

with

$$\nu = \texttt{freq}[j_\nu],$$

for array `freq` which contains the frequencies at which we wish to sample the supernova spectrum. In this way, for a given frequency $\nu = \texttt{freq}[j_\nu]$, temperature $T = \texttt{tlist}[k_T]$ and density $\rho = \texttt{dlist}[m_\rho]$ may be retrieved simply by

$$\kappa = \texttt{opacity}[k_T][m_\rho][i],$$

where `opacity` is just the array into which we read opacity data.

Most `RAGE` calculations contain more than one material, with supernovae calculations containing usually 15 or 31 elements. In this case, data is read into a 4D opacity array so that opacity κ_n from a given material n is calculated via

$$\kappa_n = \texttt{opacity}[k_T][m_\rho][i][n],$$

where n is an index ranging over materials. The total opacity of a given cell is simply

$$\kappa = \sum_n X_n \kappa_n,$$

where X_n is the mass fraction.

In practice, however, retrieving opacities for each cell is not so straight-forward. A potential problem arises if light is Doppler-shifted into or out of a given frequency bin at which we wish to calculate total luminosity. To remedy this, we consider the opacity (and emission) which will be Doppler shifted into the frequency bin of interest. The frequency at which we search the opacity array ν' is related to the frequency of interest ν via

$$\nu' = \frac{\nu(1+\beta)}{\sqrt{1-\beta^2}},$$

for $\beta = v/c$. Because we assume that this new frequency is fairly close to ν, we use a "hunt" scheme (as opposed to a "search" scheme; Press et al. 2012) to search the `opacity` array corresponding to this new frequency. While this is done for every cell at every frequency for a given data dump, we do not notice substantial performance issues with this operation.

As with `SPECTRUM`, we only consider thermal emission. In this case, we are solving

$$\frac{dI_\nu}{d\tau} = -I_\nu + B_\nu,$$

before integrating over solid angle and surface area. The Planck function has the from

$$B_\nu = \frac{2h\nu^3/c^2}{e^{h\nu/k_BT}-1}d\nu,$$

which has units of power per unit surface area. In our code, frequency is in units of $h\nu$ in keeping with the convention of our opacity tables. The Planck function in these units is

$$B_x = \frac{2}{c^2h^3}\frac{x^3}{e^{x/k_BT}-1}dx,$$

where $x = h\nu$ and c, h are in units to give B_x units of eV s^{-1} cm^{-2}. This figure is converted to erg s^{-1} during the integration of the equation of radiative transfer.

The spectrum is written not in energy/frequency space but as a function of wavelength. The conversion from $x = h\nu$ to Angstroms for the ith frequency bin is straight-forward:

$$\lambda_i = \frac{ch}{x_i} \approx \frac{12398.0}{x_i}.$$

Naively, one might assume that $L_\lambda(\lambda_i) = L_x(x_i)$, i.e. that one need only transform the x-axis of the spectrum without consideration for transforming $L(x_i)$. This is only permissible if $dx = d\lambda$ which is not the case. One must transform the spectrum while respecting

$$\int L_x dx = \int L_\lambda d\lambda,$$

or that the area in each bin is conserved. While `SPECTRUM` does not carry this out when writing its spectra, this omission is not reflected in the light curves it generates as luminosity is summed over the spectrum *prior* to this point. This *can*, however, give the incorrect shape for the spectrum, including a wrong location for the peak black body luminosity. AURORA carries out this transformation correctly and so is able to recover these morphological features.

Basic Testing

We first test our code in scenarios of very simple opacities. We consider the opacity of a single, idealized spectral "line" whose appearance is independent of temperature or density. We consider an idealized sphere of temperature T_0 and uniform density. Provided the sphere is sufficiently hot and optically thin, we expect that the line will appear in emission. This is verified in Figure 2.7. We next enclose an emitting sphere $T < T_0$ in a cold, non-emitting, optically thick shell of material. In this case, the spectral feature appears in absorption (see Figure 2.8) as expected.

We test the ability of the code to shift spectral lines as predicted for relativistic Doppler effects. We next setup a idealized star composed of 2 layers of hydrogen gas. The outer layer is Doppler shifted by $0.1c$ with respect to the layer beneath it. This causes each line to appear twice in the emergent spectrum (see Figure 2.9) with the lines emerging from the outermost layer of hydrogen appearing more luminous. This is in agreement with expectations.

The code also contains the ability to "image" 3D setups. We construct a 3D 128^3 Cartesian grid a place an optically thick, hot sphere surrounded by cold, non-emitting material. We solve the equation of radiative transfer on a 128^2 grid perpendicular to a coordinate axis to estimate

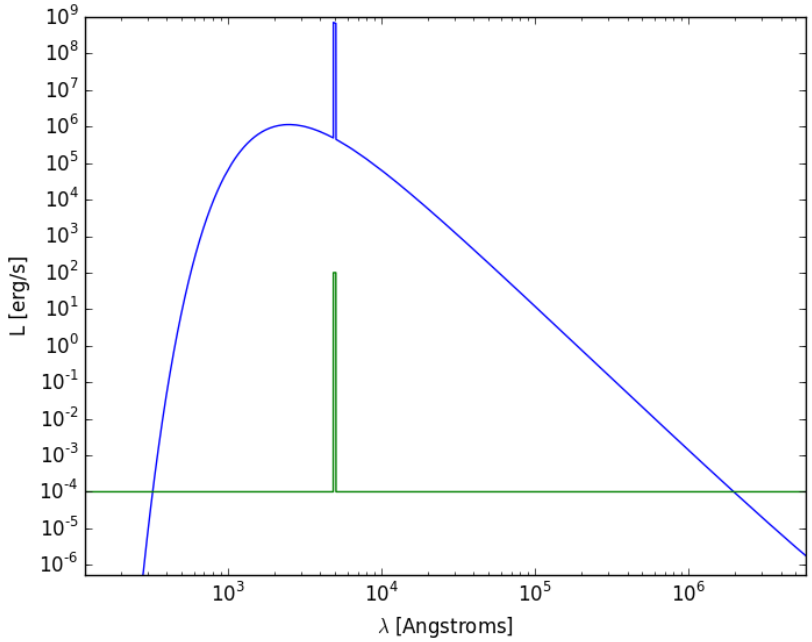

Figure 2.7 Spectrum of an emitting sphere (blue curve) emitting at a single temperature T_0. The spectral feature as characterized by the opacity (overlayed in green) appears in emission as desired.

the appearance of the sphere on a similarly positioned CCD. Our results appear in Figure 2.10, left panel. The effects of limb-darkening are apparent, the regions toward the edge of the disk suffering more extinction than those near the center. As a second test, we surround an optically thin, cold sphere of gas by a hot, optically thin shell which is subsequently placed in an optically thin, cold environment. One expects to see a ring of light at the radius of the hot shell (and not a sphere of light) as the amplification path toward the CCD is thickest in these regions. This is observed in our tests (see Figure 2.10, right panel).

Most importantly, it is important to benchmark the code against existing light curve codes including `SPECTRUM`. In Figure 2.11, we compare `SPECTRUM` and AURORA light curves in log-time to emphasize differences in the two codes. Notably, AURORA's $t = 0$ luminosity is $L_\nu \approx 10^{35}$ erg s^{-1}, much higher than that predicted by `SPECTRUM` ($\sim 10^{28}$ erg s^{-1}). `SPECTRUM` neglects

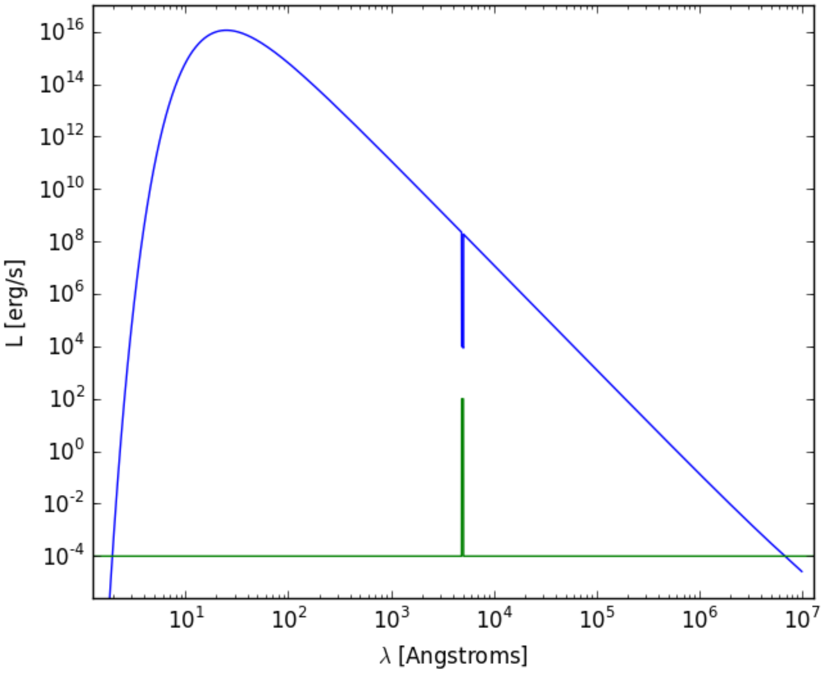

Figure 2.8 Spectrum of an emitting sphere (blue curve) emitting with a non-emitting spherical shell. The spectral feature as characterized by the opacity (overlayed in green) appears in absorption as expected.

surface emission, i.e. `SPECTRUM`'s solution to the equation of radiative transfer does not converge to $4\pi\sigma T^4$. It thus routinely *under-predicts* luminosities for optically thick scenarios. This particular supernova progenitor is a large star ($\sim 8-10 M_\odot$) which one might expect to have a total luminosity $L_* \simeq 10-100 L_\odot$. AURORA is in better agreement with this estimate ($L_\odot \sim 10^{33}$ erg s^{-1}).

One immediately notes that `SPECTRUM` predicts a brighter peak luminosity than AURORA. The most likely source of discrepancy here is that `SPECTRUM` takes into account effects of relativistic beaming when estimating the emissivity of each zone, that is, the emissivity ε_ν is enhanced such that

$$\varepsilon_\nu = \kappa(\nu) B_\nu \frac{(1-\mu\beta)^2}{\sqrt{1-\beta^2}},$$

where $\mu = \cos\theta$ is the angle between the viewer and the velocity vector of the fluid. For velocities

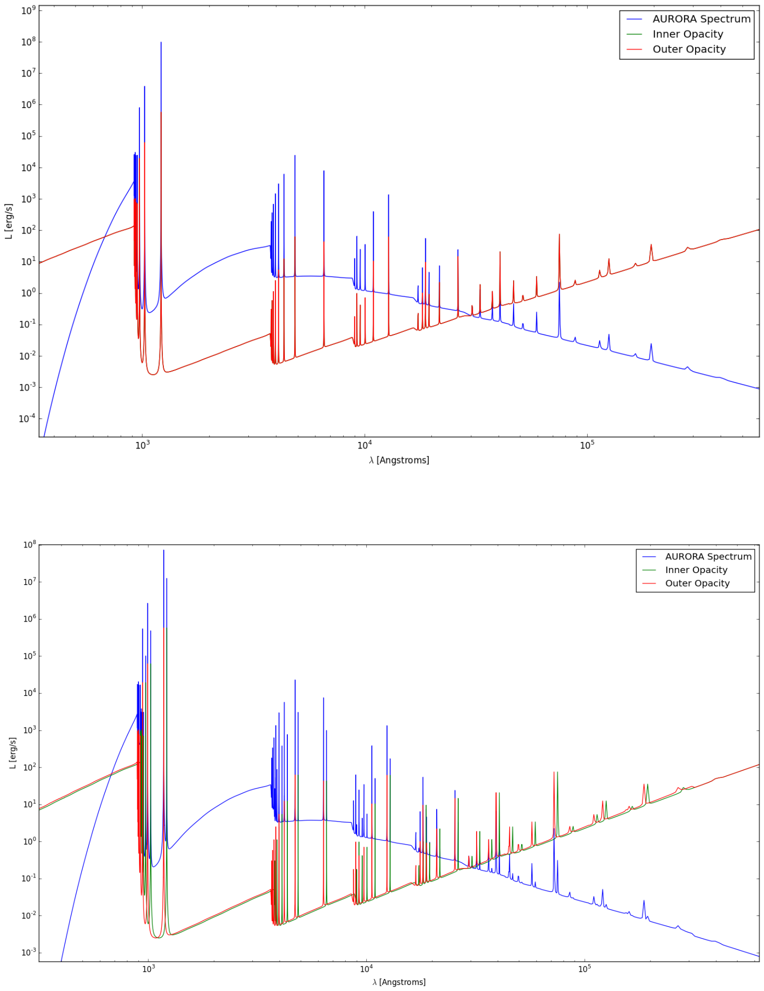

Figure 2.9 *Top panel:* Spectrum of two layers of optically thin hydrogen gas with identical temperatures and density. The spectrum (blue curve) reflects the outer and inner opacities (red and green curves) which are identical. *Bottom panel:* Same as upper panel, except that the upper-most layer of hydrogen is Doppler shifted with respect to the first layer by $0.1c$. Features appear in pairs with the lines associated with the outer layer being more luminous as we expect.

approaching the viewer ($\mu\beta < 0$) and in particular, relativistic approaching velocities ($\mu\beta \approx -1$), the $\frac{(1-\mu\beta)^2}{\sqrt{1-\beta^2}}$ factor can become arbitrarily large, enhancing the emissivity of the zone. This effect is most likely to be important at shock breakout when the shock moves at a substantial fraction of

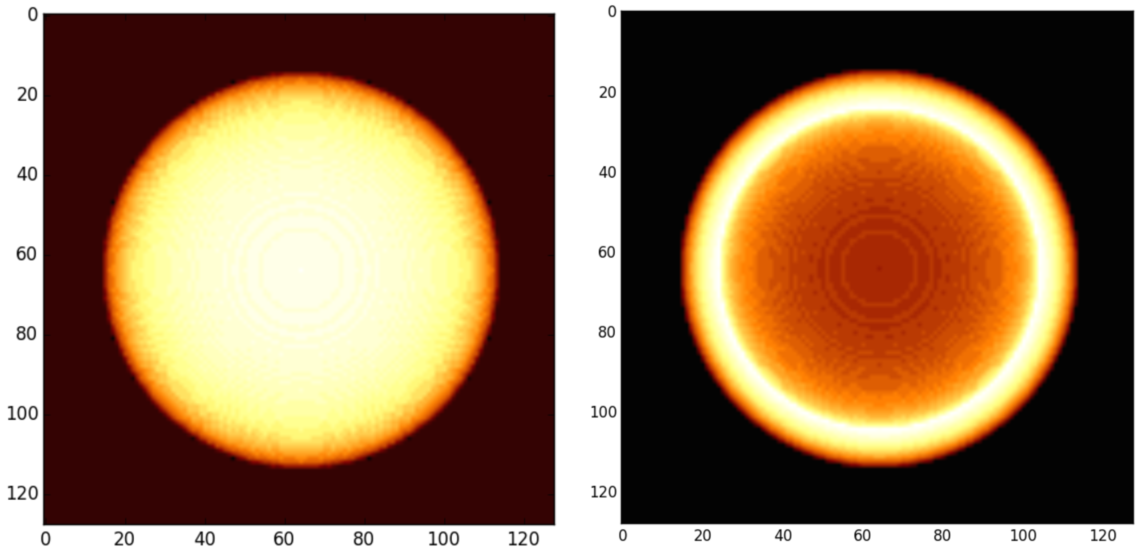

Figure 2.10 AURORA can carry out imaging of 3D structures by solving the equation for radiative transfer along rays perpendicular to a virtual CCD. Axes are labeled by pixel number. *Left panel:* An optically thick, hot (emitting) sphere is placed in an optically thin, cold gas. Plotted is the logarithm of luminosity as a function of position. *Right panel:* A sphere consisting of two, optically thin layers, the first being cold with the outer layer being hot. The observer sees a ring as expected.

the speed of light which is observed in our `RAGE` calculations. Because of these effects which are included in `SPECTRUM` and not in AURORA, we expect `SPECTRUM` to yield a higher peak luminosity, corresponding to this moment of shock breakout. This factor has since been added to AURORA as a user option. We find that this boosts luminosity meaningfully in regimes just described, in agreement with `SPECTRUM`.

AURORA compares well with `Spectrum` and `SuperNu` (Walleager 2013) at late times, when emission is dominated by the decay of radioactive Ni-56 in the core of the remnant, now visible as the remnant expands and becomes optically thin (see Figure 2.12). Of the light curve calculations presented, AURORA is the most luminous. There are several possible explanations for this. The integration scheme in AURORA lags the geometric term $4\pi r^2$ in its integration though it breaks large cells into smaller cells to reduce the error from this simplification. This leads to AURORA

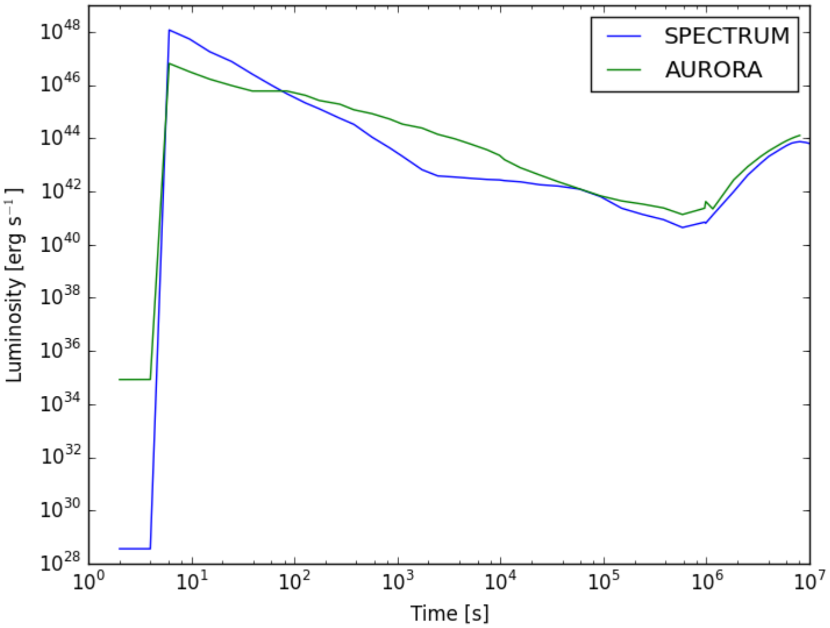

Figure 2.11 AURORA and `SPECTRUM` log-time light curve comparison for the a140 supernova blast. The codes agree over a significant portion of the light curve domain ($t > 10^6$ s). Difference between the codes arise from important differences in light curve calculation (see text).

systematically over-predicting luminosity when the remnant is optically thin. It is further worth pointing out that the version of `SPECTRUM` used to calculate this light curve suffered from a bug which artificially diminished emission from the back half of the supernova remnant which would operate to render the light curve somewhat under luminous in optically thin regimes. It is worthwhile to note, however, that all the codes agree within a factor of 2-4 over the majority of the light curve. Given differences in light curve calculation approaches between curves, agreement within an order or magnitude in luminosity is acceptable.

While the above may not necessarily constitute a series of robust code tests, they build sufficient confidence to proceed in addressing supernova light curve problems. It should be mentioned here that a primary purposes of developing AURORA was (1) create a fast, inexpensive alternative to

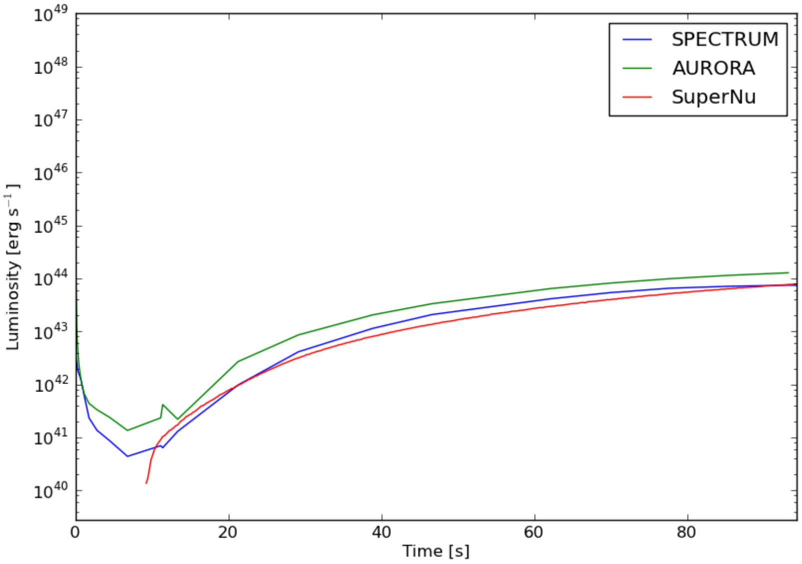

Figure 2.12 AURORA, `SPECTRUM` and `SuperNu` (Wollaeger 2013) light curve comparison for the a140 supernova blast. The agreement between the codes is remarkable. AURORA is the most luminous of the supernova light curve codes owing to the manner in which it integrates the equation of radiative transfer in the optically thin limit (see text).

`SPECTRUM` for creating light curves by integrating spectra as determined by the equation of radiative transfer and LANL OPLIB opacities and (2) cross-check `SPECTRUM` calculations. In this process, several bugs in the `SPECTRUM` have been identified. In particular, it was found that `SPECTRUM` artificially shifts opacities in frequency space at very low temperatures (not typically encountered in supernova problems) which causes substantial extinction of light which one expects to escape. This bug resulted in `SPECTRUM` under-predicting bolometric emission in calculations involving very cold and dense circumstellar shells. Building AURORA has assisted in identifying and rectifying such issues in the former code in addition to providing a useful exercise for the author.

2.3 The Observability of Low-mass Pair-Instability Supernovae and Hypernovae

2.3.1 Modeling Hypernovae and Pair-Instability Supernovae

We have modeled 12 PI SNe of rotating stars with masses from 90 to 140 solar masses in increments of 5 solar masses. We have also simulated six HNe. Observationally, hypernovae have been inferred to have explosion energies from 10 to 50 foe (Smidt et al. 2014), where 1 foe $= 10^{51}$ erg is the typical energy of a Type II SN. To explore the parameter space of likely Pop III HNe, we consider 10, 22, and 52 foe explosions of two hypernovae progenitors of 25 and 50 solar masses, respectively.

A thorough discussion of the Los Alamos Supernova Light Curve Project can be found in Frey et al. (2013). This source may be consulted for more technical details regarding our study.

Following Collapse and Explosion

Our procedure differs in the modeling of PI SNe and HNe. We will describe the modeling of HNe and PI SNe in turn. Figure 2.13 provides a schematic which may assist the reader as we discuss our method below.

The energy and luminosity of a SN can depend strongly on the structure of the star prior to the explosion. To obtain the final profiles for the progenitor star, we evolve it from birth to the onset of collapse in the Kepler (Weaver et al. 1978) or MESA (Modules for Experiments in Stellar Astrophysics) (Paxton et al. 2013) stellar evolution codes. Because hypernovae are observed to be Type Ib/c SNe with no hydrogen lines in their spectra, we then strip off the hydrogen layer from both stars (recall we only have a 25- and a 50-solar mass progenitor) before transferring it to a one-dimensional Lagrangian core collapse code (Fryer 1999). This code follows the collapse of the star through the time when the core stops contracting and bounces, at which point energy

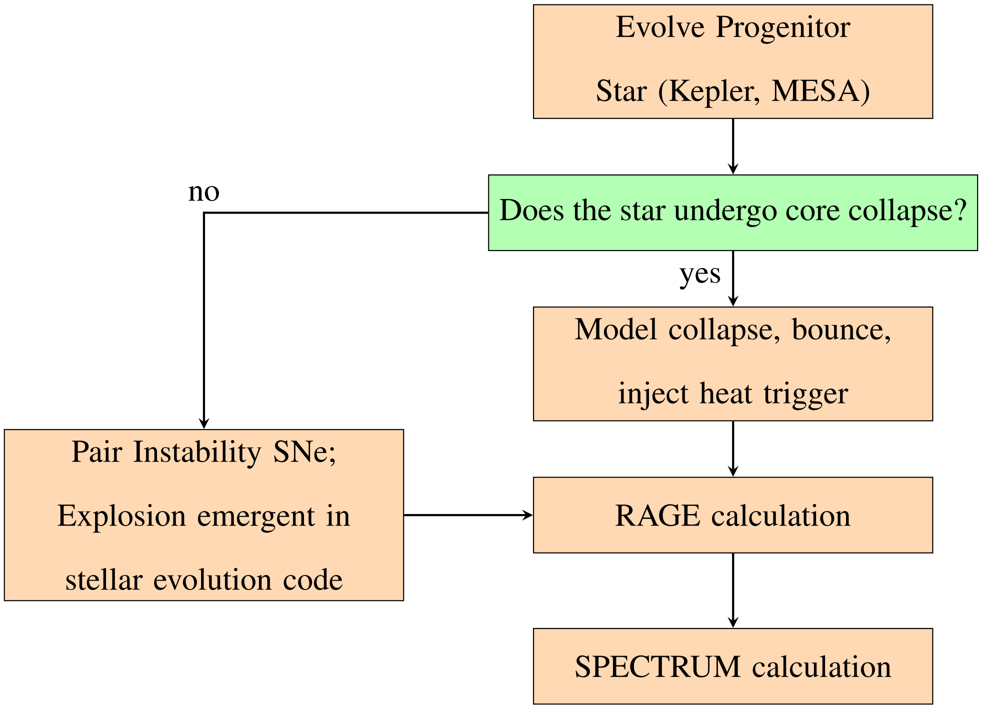

Figure 2.13 Schematic of the simulation pipeline through various LANL codes. To model hypernovae (HNe), we model core collapse and bounce and inject energy to trigger the explosion. To model pair-instability supernovae (PI SNe), this step is not required as the formation of a shock in PI SNe is emergent from the stellar evolution code. All simulations required `RAGE` and post-processing with SPECTRUM.

due to neutrino absorption is artificially injected into the inner layers (the innermost 15 cells) to drive a range of explosion energies (see Young and Fryer 2007 for additional details on this code). We note that both stellar evolution and explosive nuclear burning must be modeled with extensive nuclear reaction networks that are self-consistently coupled to hydrodynamics to capture both energy production and nucleosynthetic yields. After nuclear burning is complete, which takes a few hundred seconds in the frame of the star, the HN is then evolved in `RAGE` to follow the evolution of the shock wave as it travels through the star, bursts through its surface, and expands into the surrounding medium. The Kepler calculations require on the order of 24 hours on Los Alamos National Laboratory (LANL) platforms.

Our pair-instability progenitors were similarly modeled in Kepler and MESA, but there is no need to model core collapse and bounce or inject energy to drive the explosion. Pair production, core contraction, and explosive oxygen and silicon burning in PI SNe are emergent features of the stellar evolution model and do not have to be artificially triggered. Nuclear burning is usually finished in $10-30$ seconds in PI SNe, after which it is transferred to `RAGE`.

Although `RAGE` can follow the evolution of SN flows and radiation coming from them, it cannot calculate light curves or spectra for the explosion (which are what would actually be observed by astronomers). To calculate the observational signatures of these explosions, we post process snapshots of the flow from RAGE with the Los Alamos SPECTRUM code. SPECTRUM calculates luminosities for the SN in 14,900 wavelength bins, which can then be summed to create light curves. SPECTRUM uses the LANL OPLIB (OPacity LIBrary) opacity database (Magee et al. 1995) to determine from which regions of the flow photons can escape to an external observer. SPECTRUM can also calculate the intensities of emission and absorption lines and take into account redshifting and blueshifting of photons due to relativistic expansion of SN ejecta. Spectra in the frame of the SN at very early times must then be cosmologically redshifted and subtracted by absorption in the intervening gas to determine light curves for the event in the Earth frame ("cosmological redshifting" refers to the stretching of photon wavelengths by the expansion of the universe over cosmic time as light from the event reaches Earth). The `SPECTRUM` runs required to calculate a single light curve require as many CPU hours as a `RAGE` run but can be executed in much shorter wall clock times because they can be run in parallel (usually only 1–2 days are required per light curve).

All the simulations in this chapter are performed in one dimension and therefore exclude multi-dimensional effects that can break spherical symmetry such as hydrodynamical instabilities, magnetic fields, and turbulence. Our simulations also cannot capture orientational effects, which are thought to be important for some SNe. In some cases, mixing and dredging increases the luminosities. Over large enough sample sizes, however, the simulations do give results sufficiently robust to estimate detection limits for Pop III SNe in redshift. Our `SPECTRUM` calculations (and the LANL OPLIB opacities on which they rely) also assume that matter is in local thermodynamic equilibrium, which may break down at later times when the supernova ejecta becomes diffuse. Our one-dimensional models of HNe also treat these highly asymmetric explosions as spherical events, but we inject enough explosion energy over the entire sphere to approximate the energy emitted along just the jet. Our simulations therefore should produce reasonable estimates of HN luminosities.

Our procedure for modeling hypernovae may raise the question as to how sensitive are our results to be to the magnitude of the explosion energy injected through neutrino absorption. Although no alternative to injecting energy over the whole sphere is possible in a one-dimensional hypernova simulation, we must consider how sensitive our results are to small variations in explosion energy. Our experiment is naturally set up to bracket this, as our six hypernovae explosions are created by varying explosion energy on only two progenitors from 10 to 52 foe. The variation in our results over a given progenitor will directly shed light on this issue. In general, we find that a twofold increase in explosion energy results in an approximate twofold increase in peak luminosities.

Evolution of the Supernova Remnant in RAGE

After explosive nuclear burning is complete, output is fed to `RAGE` to model the radiation hydrodynamical evolution of the shock wave. The code captures the effects of radiating matter, which is in turn heated and accelerated by light. As the shock bursts through the surface of the star in an event called “shock breakout”, light trapped behind the shockwave streams freely into space. The accelerating shockwave heats material surrounding the star to white-hot temperatures, setting it ablaze with light (see Figure 2). The grand effect is a sharp, brilliant pulse of light. The remnant can rebrighten at later times as radioactively decaying ^{56}Ni is exposed in the expanding remnant and heats the stellar material. All of these effects are modeled in `RAGE`.

The `RAGE` simulations in our study have a root grid with 100,000 cells and allow up to 4 levels of refinement for up to 16 times more resolution. Opacities for radiation transport are derived from Los Alamos OPLIB database for the diffuse densities ($\sim 10^{-20}$ g/cm^3) typical of astrophysical scenarios. Although `RAGE` has three-temperature physics capability, in which ions, electrons, and photons can all have distinct temperatures, we use two-temperature physics, in which matter and radiation temperatures, though coupled, are evolved separately to better capture shock breakout.

Since Pop III stars are thought to die in low-density HII regions (Whalen et al. 2004) but may be enveloped by a low-density wind following the expulsion of its their hydrogen layer, we join a simple r^{-2} wind density profile with an initial density of 2×10^{-18} g/cm^3 to the surface of the star with an intervening bridge that has an r^{-20} density profile. The bridge mitigates numerical instabilities in the radiation solution in `RAGE` that would otherwise arise if the density at the surface of the star were abruptly dropped to that of the diffuse wind. We take the speed of the wind to be 1000 km/s and its composition to be primordial, 76% hydrogen and 24% helium by mass. When the wind falls to a number density of 0.1 particles per cubic cm, it is replaced by a uniform density profile similar to that of the ambient HII region.

`RAGE` runs require about 20,000 hours of CPU time on Los Alamos supercomputers and evolve

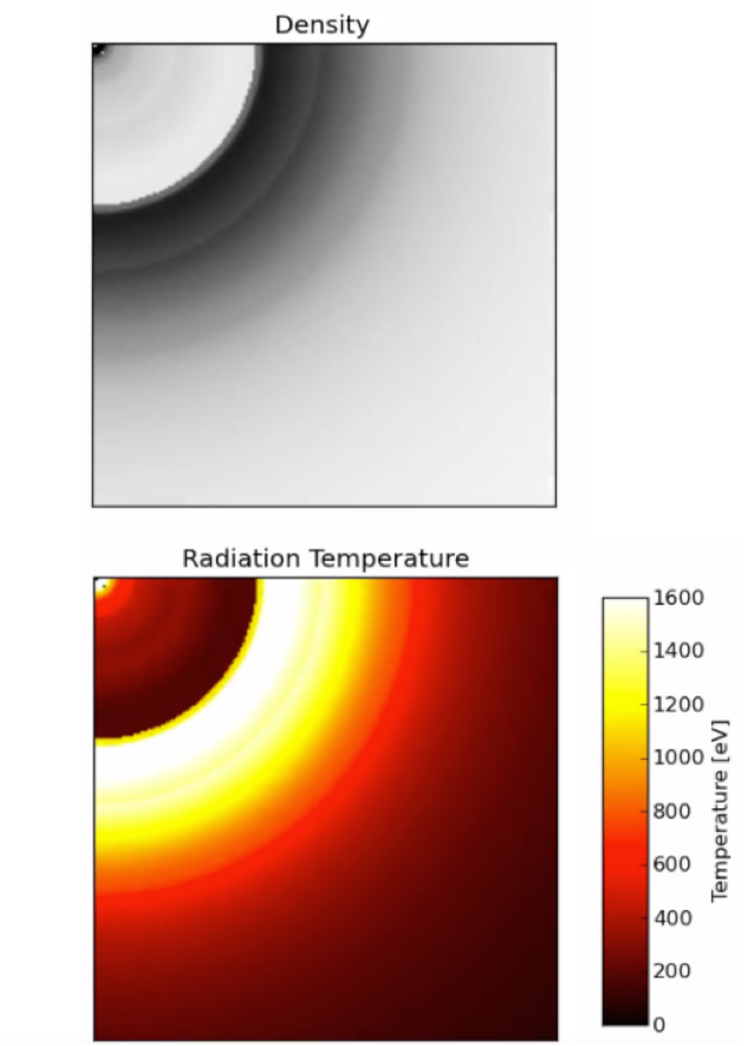

Figure 2.14 Snapshot of a `RAGE` hypernova simulation sometime following the moment when the shockwave breaks through the surface of the star and plows through the ambient medium. `RAGE` simulations are carried out in one dimension, so the extra dimension visualized here serves only to emphasize structure and provide a feel for the phenomenon. In the upper panel, relative density is indicated, black being regions with the most material. At this stage, the star has been almost completely disrupted into a ring (or a sphere in three dimensions) of glowing material. Matter has fallen back onto the central black hole (upper lefthand corner), which is radiating as observed in the bottom frame. Note that though the scale bar in the lower panel only indicates temperature up to 1600 eV, regions of this panel are tens of thousands of eV.

the explosions out to three years.

2.3.2 Results and Discussion

The total luminosity (energy/sec) as a function of time is plotted in Figure 3 for our HNe (upper panel) and some of our PI SNe (lower panel). Shock breakout is evident in all 11 events as the brief luminous pulse that lasts for about 1000 s (or about 20 min). They have about the same duration because the stars have similar radii. The peak luminosity increases with explosion energy. Although shock breakout is the brightest stage of the explosions, it will not be visible today. Most of the photons at this moment are x-rays or hard ultraviolet (UV) that are absorbed by neutral hydrogen in the early universe before they can reach earth. Those that are not absorbed would be redshifted into the extreme UV by the time they reach the Milky Way and would be stopped in its outer layers. Rebrightening due to ^{56}Ni decay is also visible in most of the light curves at $10^6 - 10^7$ seconds, or at about 3 weeks to 3 months. The degree of rebrightening is proportional to the Ni mass, which generally scales with explosion energy. The least energetic SNe exhibit little or no rebrightening because they do not form much Ni.

Future observations will not measure the total luminosities of these events nor are these stars in the local universe, so Figure 3 by itself does not give us much information regarding how observable these events will be today. Observations will instead provide fluxes in specific observing bands in the near infrared (NIR) at 2–4 microns. Surveys will hunt for the first SNe in the NIR because any wavelengths in the rest frame of the SN that are shorter than those redshifted into the NIR today will be absorbed by the early universe.

We show NIR light curves for the 50-solar mass 52-foe HN and the 120-solar mass PI SN in Figures 4 and 5. It is clear that HNe will not be visible at redshifts beyond 10–15, or about 800 million years after the Big Bang. In Figure 5, we see that PI SNe with masses below 140 solar masses will only be visible at lower redshifts still ($z \sim$ 3–8). While such events will not reveal

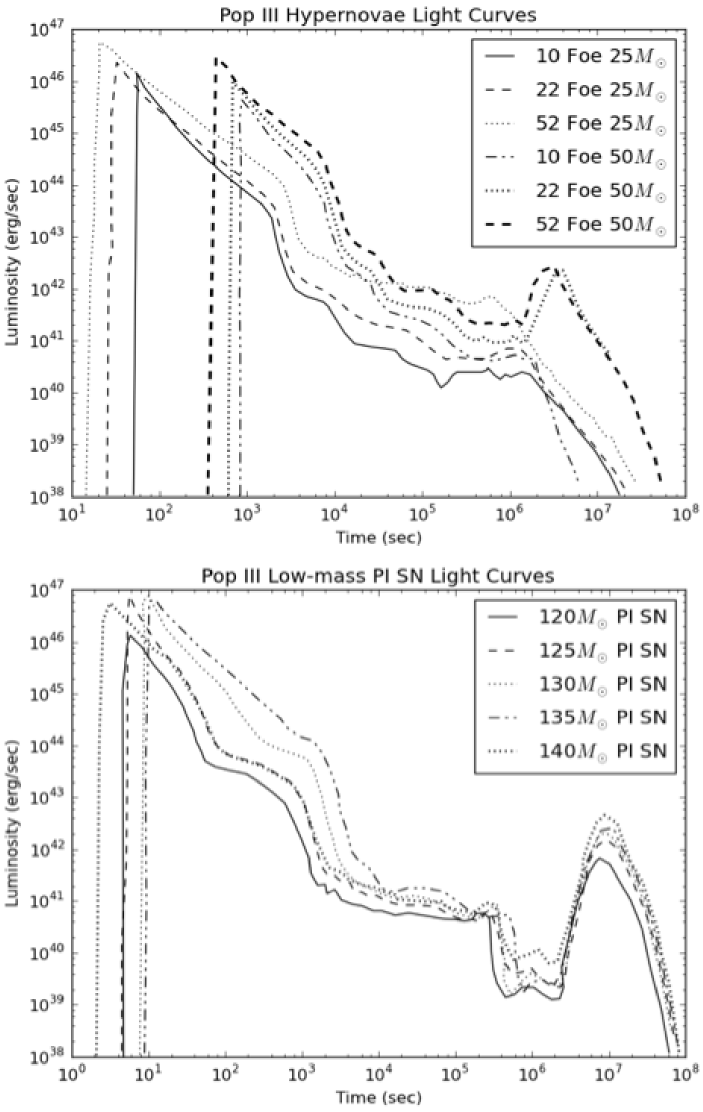
Pop III Hypernovae Light Curves

Pop III Low-mass PI SN Light Curves

Figure 2.15 The upper panel contains light curves (total luminosity over all wavelengths as a function of time) for our hypernova runs. In the lower panel, we present light curves for the 5 most massive pair instability supernovae (120-140 solar masses). These light curves are calculated in the frame of the star (i.e., they do not account for cosmological redshift and obscuring gas along the line of sight). Note the bump in the light curves around 10^6–10^8 seconds, which is due to radioactive decay of ^{56}Ni.

the properties of the first stars, they will probe the stellar populations of the first galaxies, which form at these somewhat lower redshifts. Why are these highly energetic explosions only visible at much lower redshifts than only slightly more energetic 140- to 260-solar mass PI SNe, which can be detected in the first generation of stars? It is primarily because the progenitor has a lower mass and smaller radius at the time of the explosion. The fireball cools at earlier times (and hence smaller radii) and therefore is not as luminous in the bands that are eventually redshifted into the NIR in the Earth frame. We find that this is a general property of highly energetic explosions of compact Pop III stars (Smidt et al. 2014a, 2014b).

But even if a telescope is sensitive enough to detect a primordial SN, there is no guarantee that it will actually come across one in its own lifetime. This depends on the field of view of the instrument and the number of events per square degree on the sky over some interval in redshift. The event rate in turn depends on the Pop III star formation rate. Telescopes like JWST are very sensitive but have very narrow fields of view. NIR missions such as Euclid and the Wide-Field Infrared Survey Telescope (WFIRST) are less sensitive but will survey the entire sky. These instruments could, in principle, harvest large numbers of ancient SNe.

Perhaps the greatest challenge to detecting Pop III SNe is the low star formation rate during the era of the first stars. Another is that the first SNe are efficient at chemically enriching the early universe. A single PI SNe would spew its heavy elements deep into space, altering the chemistry of large regions of the universe, so there may be a relatively narrow window in redshift in which a SN can be guaranteed to be truly a Pop III event (Wise et al. 2011; Muratov et al. 2013). Both factors limit the total number of Pop III SNe on a given patch of the sky. In lieu of direct observations of Pop III stars, we must rely on cosmological simulations of early star formation for SN rates. Unfortunately, differences in physics between the computer models can cause their predictions of star formation rates to vary by factors of 100 or more (see Whalen et al. 2014a). In particular, Johnson et al (2013b) found that HN rates could be as large as 1000 per year, with most occurring

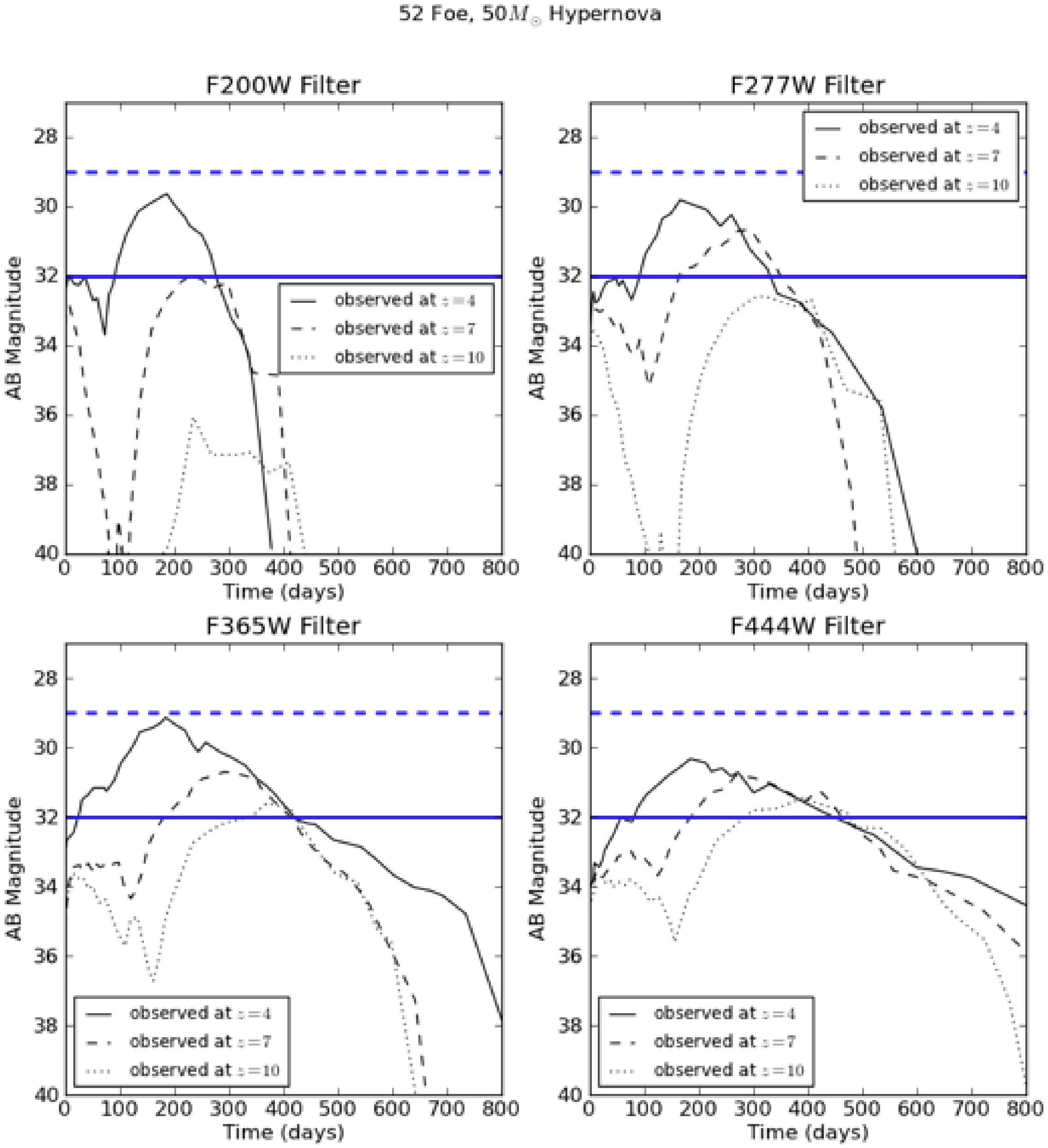

Figure 2.16 Light curves for the 50-solar mass 52-foe hypernova corrected for redshift and absorption by intervening neutral hydrogen from various redshift distances ($z = 4$ being the closest and $z = 10$ being the most distant). The different panels correspond to 4 NIRcam long-wavelength filters on the James Webb Space Telescope (JWST). The dashed horizontal lines represent the detection limit of Wide-Field Infrared Survey Telescope (WFIRST) after spectrum stacking, and the solid horizontal line is the detection limit for the JWST. This hypernova would, in principle, be visible out to $z = 10$ in some filters.

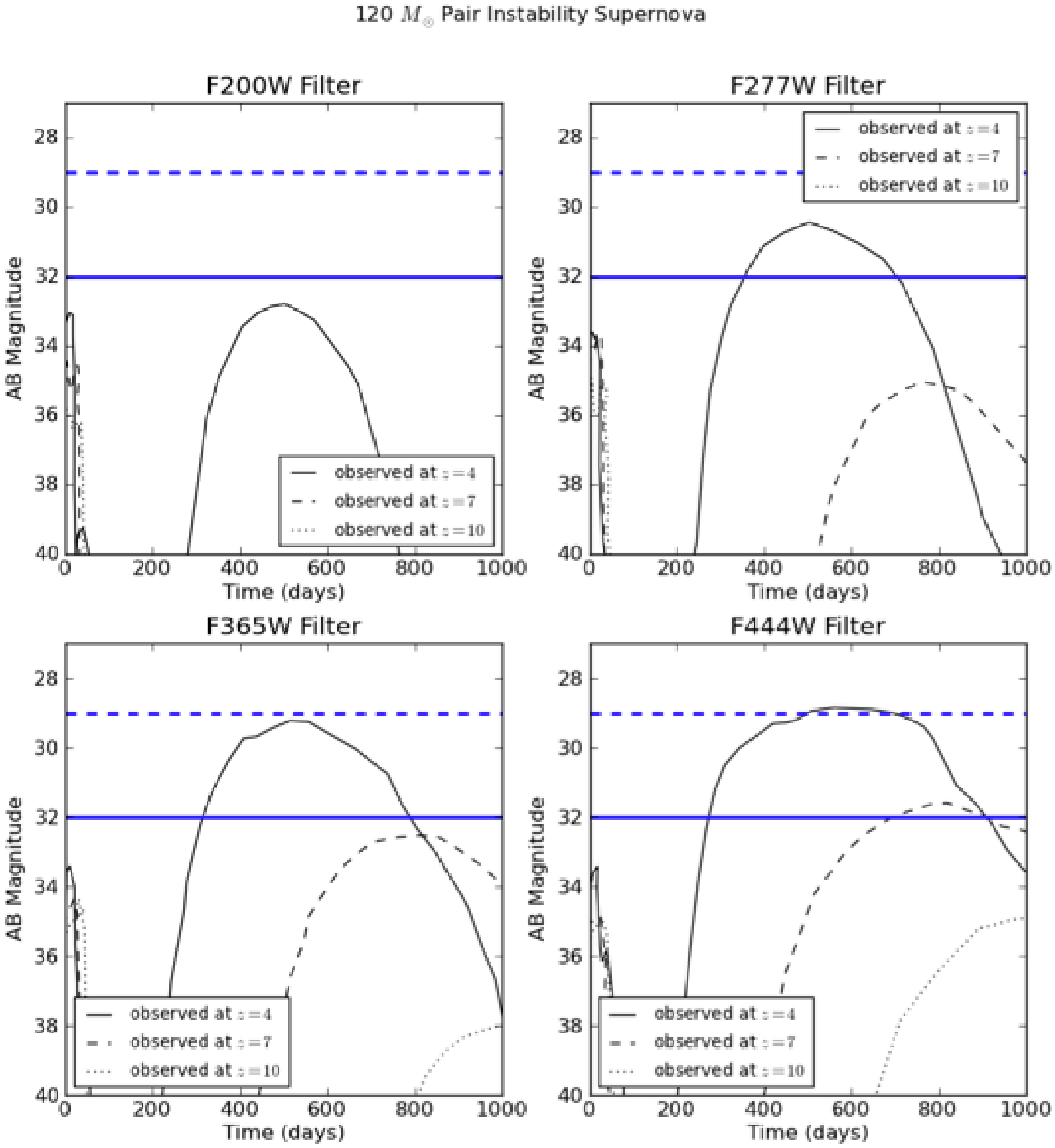

Figure 2.17 Light curves for the 120-solar mass pair instability supernova corrected for redshift and absorption by intervening neutral hydrogen from various redshift distances ($z = 4$ being the closest and $z = 10$ being the most distant). The different panels correspond to 4 NIRcam long-wavelength filters on the James Webb Space Telescope (JWST). The dashed horizontal line represents the detection limit of Wide-Field Infrared Survey Telescope (WFIRST) after spectrum stacking, and the solid horizontal line is the detection limit for the JWST.

fairly late in the era of the first stars ($z < 10$ or about 13.3 billion years ago). Campisi et al. (2011) found a more conservative estimate of about 100 HN events per year across this era. We note that even the failure to detect Pop III SNe in future surveys would be useful because it would rule out the cosmological models with the most optimistic star formation rates.

Could Pop III HNe be found by radio telescopes in surveys? Meiksin and Whalen (2013) have analyzed simulations of Pop III explosions in cosmological halos carried out with the ZEUS-MP code to estimate radio fluxes from HN and core-collapse SN remnants. They find that energetic HNe could be as bright as a few microJanskys in the L and 3-GHz bands, well within the detection limits of existing radio telescopes such as eMerlin and the Jansky Very Large Array (JVLA) Back-of-the-envelope calculations reveal that as many as two radio HNe could be present in a square degree of sky at any given time. To achieve $\sim$ 3-microJansky sensitivity in the L band requires the JVLA to dwell on a single region of the sky for nearly 100 hours. Roughly eight such episodes would be required to reject the claim of two hypernovae per square degree with $\sim 95\%$ confidence, bringing the total project time for such an undertaking up to a staggering 800 hours on the world's premier radio telescope. Further, if a supernova candidate were identified, follow-up over the space of years would be required to uniquely identify the event as a primordial explosion. Such surveys are possible, however. The VLA has carried out a capabilities test of the VLA with a 1000-hour survey on a single patch of sky in L band that will take place over years. The survey will achieve sensitivities that would otherwise only be attainable by future radio telescope arrays like the Square-Kilometer Array, which will be built in South Africa and be able to detect Pop III core-collapse SNe in addition to HNe. Efforts to find the first cosmic explosions could piggyback on such current surveys. The detection of a primordial supernova will be among the landmark achievements in astronomy in the coming decade.

2.3.3 The Outlook for Pop III Hypernovae and Low-mass Pair-instability Supernovae

In this chapter, we have described recent efforts by the Los Alamos Light Curve Project to assess the observability of some types of primordial SNe. We have considered the PI SN explosions of compact 90- to 140-solar mass Pop III stars and 25- and 50-solar mass Pop III HNe. We find that these events, although highly energetic, will not be bright enough to be seen at Cosmic Dawn by next-generation telescopes but may be visible in the earliest galaxies. They will complement other types of Pop III SNE as probes of the early universe.

CHAPTER

THREE

LYMAN-α EMISSION FROM MASSIVE BLACK HOLES IN THE EARLY UNIVERSE

3.1 Lyman-α Emitter CR7

One of the most intriguing observations of the high-redshift Universe is the detection of the extraordinarily bright Lyman-α emitting object in CR7, which exhibits some of the principal characteristics predicted for a galaxy composed solely of pristine primordial gas (Sobral et al. 2015). Among these characteristics are bright He II 1640 angstrom emission, which is indicative of a hot nebula powered by radiation with a particularly hard spectrum (e.g. Bromm et al. 2001; Tumlinson et al. 2001; Oh et al. 2001; Schaerer 2002); the absence of emission features from elements heavier than the helium produced during Big Bang nucleosynthesis; and a nearby (~ 5 kpc) metal-enriched galaxy, ultraviolet (UV) radiation from which could have suppressed star formation, and the resultant metal enrichment from supernovae, in its progenitor dark matter (DM) halos. These characteristics are consistent with two possibilities for the sources of the radiation powering CR7: a massive ($> 10^7$ $M_\odot$) cluster of Population III stars formed from the rapid collapse of primordial

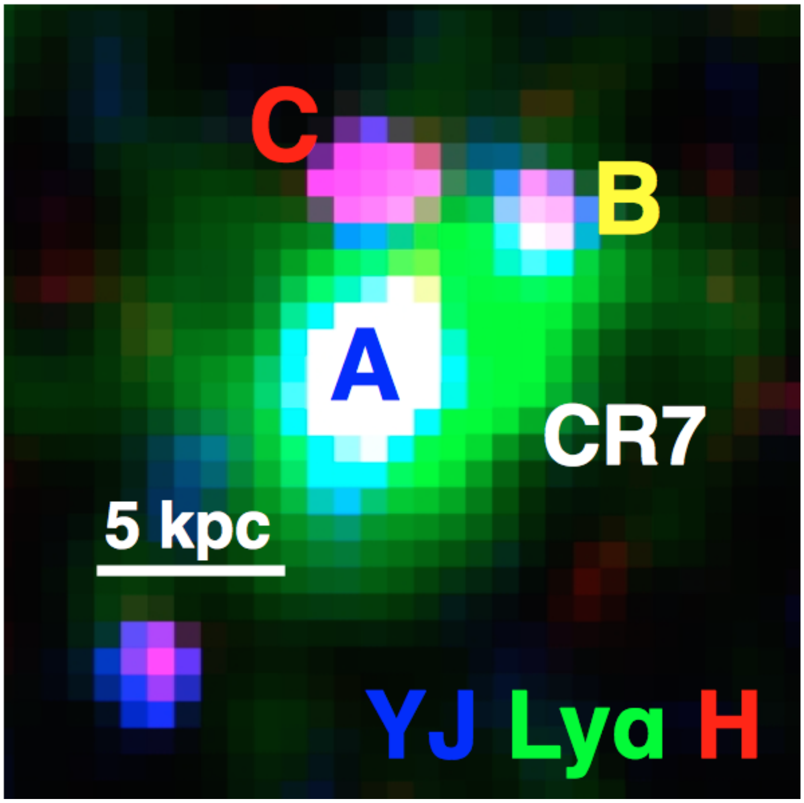

Figure 3.1 HST image of Cosmos Redshift 7 (CR7) from Sobral et al. 2015. Blue colors indicate UV emission, green corresponds to Lyman-α and red, H-α. The CR7 system has three distinct components, A appearing to be the primary Lyman-α source. Lyman-Werner radiation was observed by Sobral et al. from clump A and so indicate that the other clumps may also be Lyman-Werner producers. Image credit: Sobral et al. (2015).

gas photo-heated by the neighboring galaxy (Johnson et al. 2010; Visbal et al. 2016), and an accreting black hole (BH) with a mass $> 10^6$ $M_\odot$ (Pallottini et al. 2015) which may drive a strong outflow that imprints features in the Lyman-α line profile (Smith et al. 2016; Dijkstra et al. 2016).

Sobral et al. (2015) noted a large line ratio between the He II 1640 emission and the Lyman-α flux ($L_{\mathrm{He}} = 0.2L_\alpha$). Nebular He II 1640 emission is recombinatory in character, representing a $3 \rightarrow 2$ transition. The ionization energy for He is $\sim$ 24 eV, hotter than what could be provided by hot O type stars (Hartel et al. 2015). This suggests that CR7 is powered by a very hard, ionizing spectrum more characteristic of an AGN than a pop III stellar population. Indeed a very bright ionizing source could prevent star formation by keeping gas sufficiently hot to prevent instances of proto-stellar collapse.

Among the defining characteristics of the direct collapse scenario is one or more neighboring halos to provide a Lyman-Werner background to keep the prospective halo for direct collapse from cooling and collapsing to form stars. In the case of CR7, it appears likely that the neighboring galaxy may have produced sufficient Lyman-Werner radiation for the BH to have been born with a mass $\sim 10^5$ $M_\odot$ via direct collapse (Agarwal et al. 2015; Hartwig et al. 2015); if so, this may be the first instance of direct collapse observed in nature (for reviews see Volonteri 2012; Haiman 2013; Johnson & Haardt 2016).

In this chapter, we present the first cosmological hydrodynamic simulations aimed directly at modeling the Lyman-α emitting object in CR7, under the assumption that it is indeed powered by accretion of primordial gas onto a supermassive black hole which is seeded at higher redshift ($z \sim 15$).[1] In the next Section, we describe our *Enzo* radiation hydrodynamic simulations of the growth and radiative feedback from the BH. In Section 3, we present our modeling of the nebular emission powered by the accretion process at the observed redshift $z \sim 6.6$ of CR7. Finally, we conclude with a brief discussion of our results in Section 4.

3.2 Cosmological Simulations

The simulations were preformed using Enzo, a publicly available AMR code for modeling astrophysical fluid flows (Bryan et al. 2013), that contains the necessary modules for hydrodynamics, radiation, primordial chemistry and black hole physics required in this calculation. The initial conditions were generated by MUSIC (Hahn and Abel (2011)), also an open source cosmology

---

[1] While our simulations do not capture every process contributing to the formation of a CR7-like object, starting from the Big Bang, they are *ab initio* in the sense that they track the key processes impacting the formation of such an object starting from realistic cosmological initial conditions.

code, using the Planck 2015 TT,TE,EE+lowP+lensing+ext best fit parameters (Planck collaboration). MUSIC was run using the Eisenstein & Hu transfer function with second-order perturbation theory enabled and an initial redshift of $z = 200$.

To find the optimal halo, several 4 Mpc/h boxes with 256^3 resolution were generated with MUSIC. These boxes were then run in Enzo with both baryons and dark matter down to z = 6.6 with one level of AMR refinement everywhere in the box. YT's (Turk et al. 2011) HOP halo finder was used on several redshift snapshots for each box to find a halo with the right final mass and stability properties: since a future nested-refinement simulation was to be run, it is important that the halo remain stationary on the grid down to the final redshift with no large mergers from other halos that would be formed off the nested grid. One box containing a $3 \times 10^{10}\ M_{\odot}$ halo, roughly consistent with estimates for the halo mass from the literature (Agarwal et al. 2015; Hartwig et al. 2015), with these stability properties was chosen to be the simulation described in the rest of this paper.

With this vetted cosmological box in hand, MUSIC was rerun with nested grids to create a central fine-grid region, extending 25% across the box centered on the known halo, with an effective resolution of 1024^3 and the same random seeds as before to reproduce the aforementioned halo with better resolution. This central fine-grid region contains $9.11 \times 10^{10}\ h^{-1}$ $\mathrm{M}_{\odot}$ of matter with a dark matter particle mass resolution of 4305.74 h^{-1} $\mathrm{M}_{\odot}$ and a baryon mass resolution of 803.9 h^{-1} $\mathrm{M}_{\odot}$. These initial conditions became the basis for our production run.

These initial condition were evolved in *Enzo* with 9-species primordial chemistry and cooling (H, H+, He, He+, He++, e-, H2, H2+ and H-) allowing up to nine levels of AMR refinement in the fine-grid region triggered by overdensities in dark matter or baryons and the additional criteria of 32 cells across a Jean's length. Nine levels of refinement represents a spacial resolution of $\sim$ 30 pc/h. The simulation was run until our candidate halo reached 10^8 $\mathrm{M}_{\odot}$ around $z \sim 15$. At this point a massive black hole seed was inserted in the center of the halo and radiation feedback using an X-ray spectrum taken from Johnson et. al (2011; see also e.g. Kuhlen & Madau 2005) was emitted from the seed as feedback. This spectrum was binned into four equal bins representing the first through fourth 25% bins of energy of that spectrum. The accretion onto the black hole was regulated by the subgrid alpha disk formalism of DeBuhr et al.(2010) and a Lyman Werner background of $J_{21} = 10^4$ (in units of 10^{-21} erg s^{-1} cm^{-2} Hz^{-1} sr^{-1}) was turned on, in order to mimic the radiative feedback from the galaxies nearby CR7 (e.g. Agarwal et al. 2015).

A few different initial black hole seeds were attempted. The reason being is that large black hole seeds, the 10^{4-5} $M_\odot$ suggested in the direct collapse model, reach 10^7 $M_\odot$ rather quickly and then loiter in that region with significantly sub-Eddington accretion. On the other hand, 10^3 black hole seeds take much longer to grow to 10^7 $M_\odot$ and thus are closer to the near-Eddington accretion proposed in the literature. We find that candidates that are still within a factor of a few from Eddington at $z = 6.6$ have line ratios that match the observations best with our best seed presented in this paper being 3160 $M_\odot$. It must be stressed however that this seed is dependent on the dynamics of the halo chosen. For example, had we simulated a halo that arrived at 10^8 $M_\odot$ later on through mergers, a larger black hole seed more like 10^{4-5} $M_\odot$ may have been needed. Given our simplified approach to modeling the Lyman Werner radiation field, which in the CR7 system is likely dominated by nearby star-forming galaxies, our simulations do not capture details of the initial collapse of the primordial gas in the formation of the black hole seed which relate to the anisotropic radiation field produced by nearby sources (e.g. Dijkstra et al. 2008; Ahn et al. 2009; Agarwal et al. 2014; Regan et al. 2014; Visbal et al. 2014; Chon et al. 2016; Habouzit et al. 2016; Valiante et al. 2016) or to the impact of higher energy radiation, which can alter the chemistry of the primordial gas (e.g. Inayoshi & Omukai 2011; Regan et al. 2015, 1016). That said, given that a black hole does in fact form, our simulations track the impact of the radiation produced in the accretion process, which we expect to play a dominant role in determining the chemical and dynamical state of the gas in the host halo.

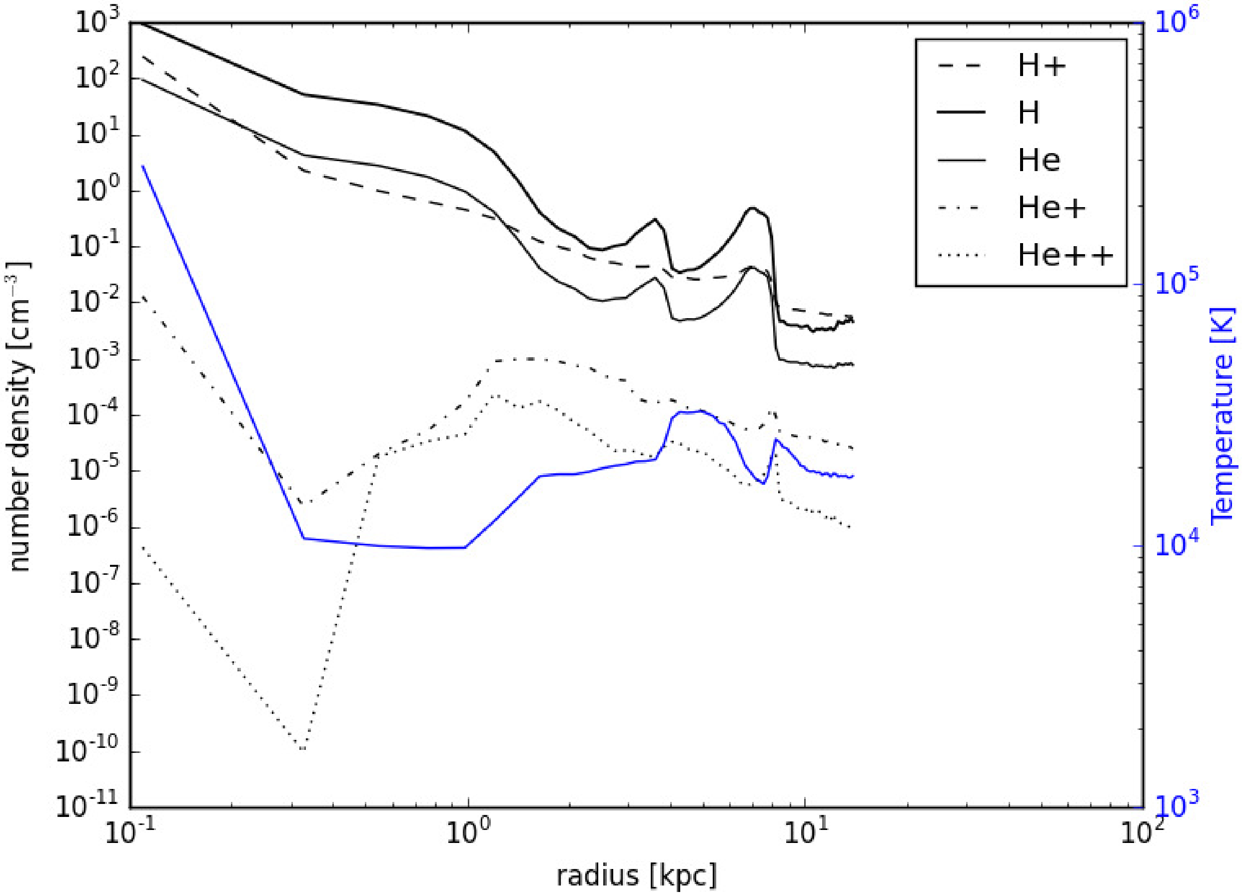

Figure 3.2 Azimuthally-averaged number densities for chemical species (black) and gas temperature (blue) as a function of distance from the central BH.

Figure 3.2 shows profiles of the halo at $z = 6.6$. We show the recombinatory Lyman-α emissivity as a function of position (a rough measure of density and temperature) in Figure 3.3.

3.3 Post-process

In primordial galaxies, Lyman-α primarily originates from a sequence of de-excitations in atomic hydrogen following recombination. If the ionizing spectrum is harder than that produced by massive Pop III stars, soft x-rays ($\sim$ 1 Kev) can escape largely ionized regions and be absorbed in the

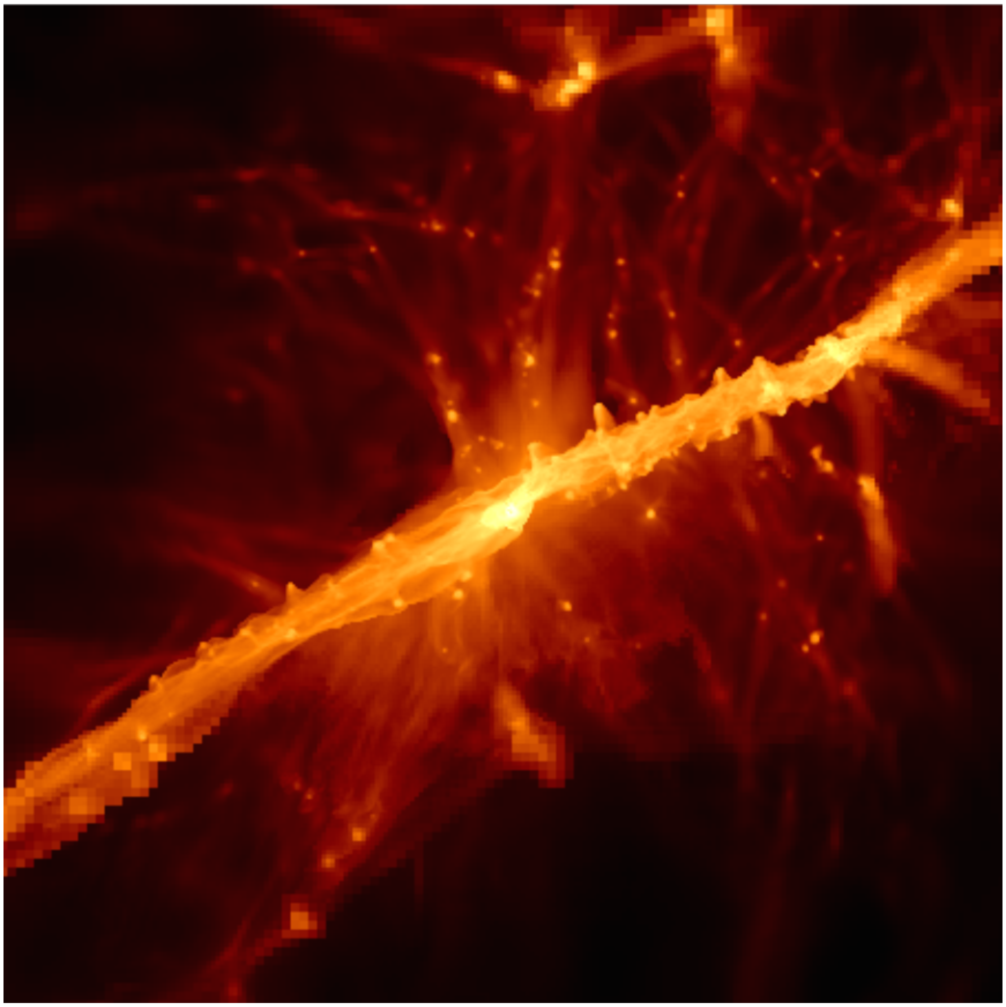

Figure 3.3 CR7 model as calculated by *ENZO* and post-processed with AURORA (see Chapter 2) to show regions of nebular (recombinatory) Lyman-α emission. CR7 is fed strongly aspherically along a filament. Apparent pixelation near the edges of the image is an artifact of *ENZO*'s adaptive mesh refinement (AMR) scheme which resolution is adapted only in regions where it is needed. This frame is $\sim$ 100 Kpc on a side.

neutral IGM. Ionizations by high energy photons result in correspondingly energetic free electrons which can serve to also ionize and excite additional neutral hydrogen. Up to 30% of an electron's energy in such scenarios can result in Lyman-α luminosity (Baek & Ferrara 2013, Valdes & Ferrara 2008). We note that this scenario will not take place with a softer ionizing spectrum as ionizing photons are liable to be absorbed in a larger HII region and electron enegies only contribute to heat the gas through electron-electron scatterings.

ENZO+MORAY treats secondary ionizations (Wise & Abel 2010). The Lyman-α emissivity in the frame of the fluid $\varepsilon(\nu)$ of a parcel of gas of volume V with electron and proton number densities n_e and n_p from radiative recombinations is just

$$\varepsilon(\nu) = C n_e n_p \alpha_B E_{\text{Ly-}\alpha} \phi(\nu) V, \tag{3.1}$$

where C is the fraction of recombinations resulting in the Lyman-α transition, α_B is the case-B recombination coefficient, $E_{\text{Ly-}\alpha}$ is the energy of the $2 \rightarrow 1$ transition, and $\phi(\nu)$ is the Voygt line profile which takes into account the effects of thermal doppler broadening and is normalized to 1. The escape fraction f_{esc} of Lyman-α photons for a BH scenario is ~ 0.5 and ~ 0.1 for primordial stellar populations respectively (see Hartwig et al. 2015). Our process also takes into account contributions from collisional excitation and the effects of collisional de-excitation.

Lyman-α is a resonate line, so line strengths and widths must be calculated with a method which takes into account scattering. Our Monte Carlo (MC) Lyman-α transfer calculation, facilitated by the HOT framework (Warren & Salmon 1995) is identical to that found in Djistra (2014) but we do not take into account energy losses from recoil (e.g. Barnes 2014) or relativistic effects which are negligable at these energies. Our MC process further takes into account destruction of Lyman-α via collisional de-excitations and photo-ionization of excited hydrogen which can be effective in metal-free environments (Dijkstra, Gronke & Sobral 2016). We calculate Lyman-α spectra via a peel-off method (e.g. Zheng & Mirald-Escude 2002) and accelerate the scheme with the prescription in Barnes (2009). We further assume steady-state transfer, i.e. we post-process only a single data dump at $z = 6.6$.

HeII 1640 Å emission may also be recombinatory, but at temperatures $10^5 - 10^6$ K, emission from collisional excitations dominate. To derive HeII 1640 Å emission, we use the method in Yang et al. (2005). Such emission is not resonant, so will only be thermally and kinematically broadened by bulk fluid motions.

3.4 Monte-Carlo Lyman-α Transfer

3.4.1 Theory

Because Lyman-α (2p $\rightarrow$ 1s) emission signals the decay to a ground state (1s), it is *resonant*, which means that it will likely be absorbed and re-emitted many times before it leaves the cloud. The Einstein coefficient for spontaneous decay ($A_{\text{Ly-}\alpha}^{-1}$ 10^{-9} s) imposes a very small timescale between aborption and reemission which suggests that the concept of "Lyman-α resonant scattering" is appropriate. It is further true that because re-emission takes place through a random angle[2] and because the Lyman-α scatters on an atom with some deviation from the bulk-fluid velocity, Lyman-α photons can change substantially in frequency as they escape. Indeed, to escape a cloud, Lyman-α *must* migrate from its emitted frequency to avoid near immediate re-absorption.

We characterize the Lyman-α profile $\phi(x)$ with the familiar definition:

$$\phi(x) = \frac{1}{\sqrt{\pi}v_D} e^{-x^2}, \ |x| < x_{\text{crit}} \qquad \phi(x) = \frac{1}{\sqrt{\pi}v_D} \frac{1}{\sqrt{\pi}x^2}, \ |x| > x_{\text{crit}} \tag{3.2}$$

where $v_D = v_{\text{th}} \nu_0 / c$ is the Doppler width of the line, $v_{\text{th}} = \sqrt{2k_B T / m_p}$ is atomic velocity dispersion at temperature T times $\sqrt{2}$. The quantity x taken as an argument for our line profile is related to

---

[2] The probability density function of re-emission angle from Lyman-α is not isotropic but follows a dipole distribution. We discuss this in greater detail below.

photon frequency ν by

$$x = \frac{\nu - \nu_0}{\nu_D},$$

where $\nu_0 \simeq 2.466 \times 10^{15}$ s^{-1} is the central line frequency. These so-called “doppler units” for frequency[3] are convenient for calculating scattering, etc. In principle, we would much rather adopt the Voigt profile for $\phi(x)$ which carries the form

$$\phi(x) = \frac{1}{\sqrt{\pi}\nu_D}\frac{a}{\pi}\int \frac{e^{-y^2}}{(x-y)^2 + a^2}\,dy, \tag{3.3}$$

which itself is a convolution of the Lorentz and Gaussian profiles. Here a is the Voigt parameter which has the form

$$a = \frac{A_\alpha}{4\pi\nu_D} \simeq \frac{4.7 \times 10^{-4}}{\sqrt{T/10^4 \text{ K}}}. \tag{3.4}$$

The Voigt profile is, however, somewhat cumbersome to evaluate in practice. The piece-wise definition given above is sufficient for our purposes.

With our characterization of our line profile we are now prepared to define the cross-section σ for absorption of Lyman-α by neutral hydrogen, i.e.

$$\sigma = f_{12}\pi c r_e \phi(x) \tag{3.5}$$

with $f_{12} = 0.4167$ is the oscillator strength and $r_e = 2.82 \times 10^{-13}$ is the electron radius. We plot σ as a function of frequency x for temperatures of 10,000 K in Figure 3.4.

From σ we assemble the optical depth τ which takes the familiar form

$$\tau = \int n_H(s)\sigma(s)\,ds, \tag{3.6}$$

where n_H is the neutral hydrogen number density and s is position. The probability P that a photon travels τ before absorption is simply

$$P = e^{-\tau}.$$

---

[3] Note that x is dimensionless.

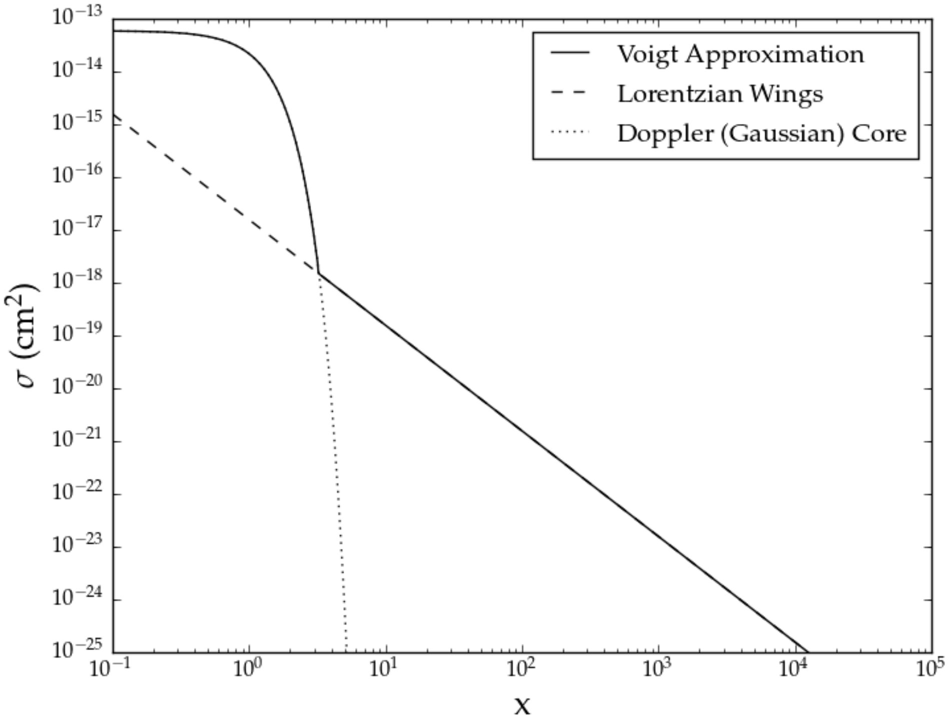

Figure 3.4 Lyman-α absorption cross-section σ at 10,000 K as a function of frequency $x = (\nu - \nu_0)/\nu_D$ in Doppler units (see text). For the line profile $\phi(x)$ we have adopted an approximation for the Voigt profile. This piece-wise defined approximation gives good results for small x.

Photons which are absorbed by neutral hydrogen are re-emitted at the same frequency with which they were absorbed in a random direction. However, because the absorbing/reemitting atom has some 3D velocity with respect to the bulk flow of the fluid, with photon will be Doppler shifted during the scattering. Lyman-α transfer, then, involves *partially coherent*[4] scatterings, where the incoming and outgoing frequencies of the photons are related by only these Doppler effects. Functions which map incoming and outgoing frequencies of a scattering are called *redistribution functions* $R = R(x_{\text{in}}, x_{\text{out}})$, and can be quite involved especially if the scattering is incoherent. Redistribution functions describing partially coherent scatterings are termed type-II redistribution functions to distinguish them from their more general counterparts which describe incoherent scattering (type-I). Our redistribution function takes the form

$$x_{\text{out}} = x_{\text{in}} + \frac{\mathbf{v}_a \cdot (\mathbf{n}_{\text{out}} - \mathbf{n}_{\text{in}})}{v_{th}}, \tag{3.7}$$

where $\mathbf{v}_a$, $\mathbf{n}_{\text{out}}$, $\mathbf{n}_{\text{in}}$ are the velocity of the scattering atom, the outgoing and incoming photon's directions respectively. Note that x_{out} and x_{in} are in the frame of the bulk motion of the fluid $\mathbf{v}_f$. Our method of calculating these quantities is detailed in the next section, but we plot a family of redistribution functions for various choices of x_{in} for temperatures of 10 K as generated via Monte Carlo sampling by our code in Figure 3.5. Our redistribution functions largely agree with of those presented for Lyman-α in the literature (see e.g. Dijkstra 2014). Deviations between our redistribution functions and those formerly presented may be due to different choices of temperature (redistribution functions are sensitive to the choice of a) and the fact that we use an accelerated scheme for sampling the scattering atom's velocity $\mathbf{v}_a$ which involves shortcuts to speed success in a rejection-type method (see below). The evolving morphology of the redistribution function with increasing x is worth discussing and we address this at the conclusion of this subsection.

We now discuss the method for assigning scattering atom velocities $\mathbf{v}_a$. We might initially

---

[4] This is in contrast to *coherent* scatterings where photons do not change frequency during the scattering and *incoherent* scattering where the relationship between incoming and outgoing frequencies is more complicated.

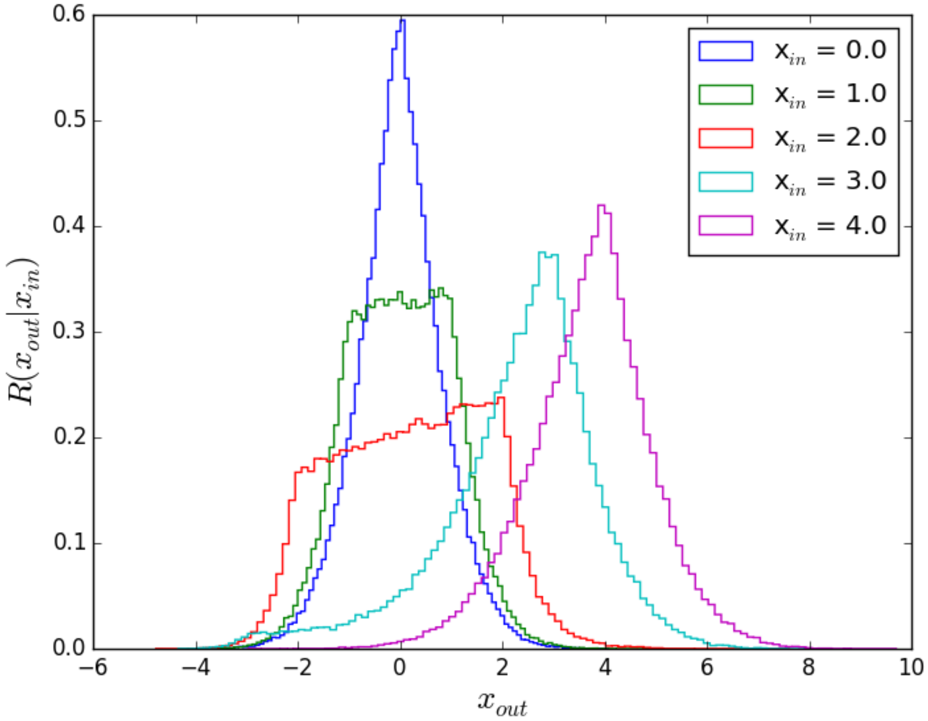

Figure 3.5 Redistribution functions $R(x_{\rm in}, x_{\rm out})$ as defined in equation (3.7) for various choices of $x_{\rm in}$. These redistribution functions are defined for $T = 10$ K, using the rejection method in Zheng & Miralda-Escude (2002) with Barnes' (2009) definition of μ_0 and neglecting recoil. Compare with Behrens & Niemeyer (2013), their Figure B.1.

assume that we could simply draw the atom's velocity from a Boltzmann distribution. However, the scattering atom has certain restrictions on the parallel component of its velocity. In particular, the atom's velocity must be such that its absorption frequency "aligns" with the frequency of the incident photon. The probability distribution for the parallel component of the velocity is given by

$$P(u) = \frac{\pi}{a} \frac{e^{-u^2}}{(x-u)^2 - a^2} \frac{1}{\phi(x)} du \tag{3.8}$$

where I have defined $u = v_{||}/v_{th}$ as the parallel component of the atom's velocity in Doppler units. The remaining perpendicular components of the atom's velocity may be drawn from the Boltzmann distribution. We discuss our method for drawing velocities from these distributions below.

In principle, the scattering of Lyman-α photons is not purely elastic: the frequencies of the absorbed and reemitted photons should differ by the momentum imparted to the atom through recoil. These effects are safely ignored at Lyman-α frequencies. If recoil effect is accounted for, one expects that the angle of incidence and angle of reemission will be related via a dipole distribution. In practice, accounting for this angular dependence does not noticeably improve results. For this work we adopt

$$P(\mathbf{n}_{\text{out}}|\mathbf{n}_{\text{in}}) = \text{constant},$$

or that the angle of reemission is isotropic.

The fact that the redistribution function evolves strongly with x_{in} suggests that photons which are in the Doppler core ($|x| <\sim 3$) are liable to be scattered back toward $x = 0$, while photons in the Lorentz wings will likely be scattered away. In a sense, photons inside the Doppler core experience a type of "restoring" force, so that only photons scattering off of high velocity atoms ultimately escape. This can be seen by considering the scattering of a Lyman-α photon in the frame of the atom. In Figure 3.6, we plot the probability P of a photon with x_{in} being seen by an atom at x_{atm} . In the case of $x_{\text{in}} = 2.5$, the distribution is strongly peaked in around $x_{atm} = 0$, meaning that at $x_{\text{in}} = 2.5$, the probability is high that the photon was absorbed by an atom for which this photon

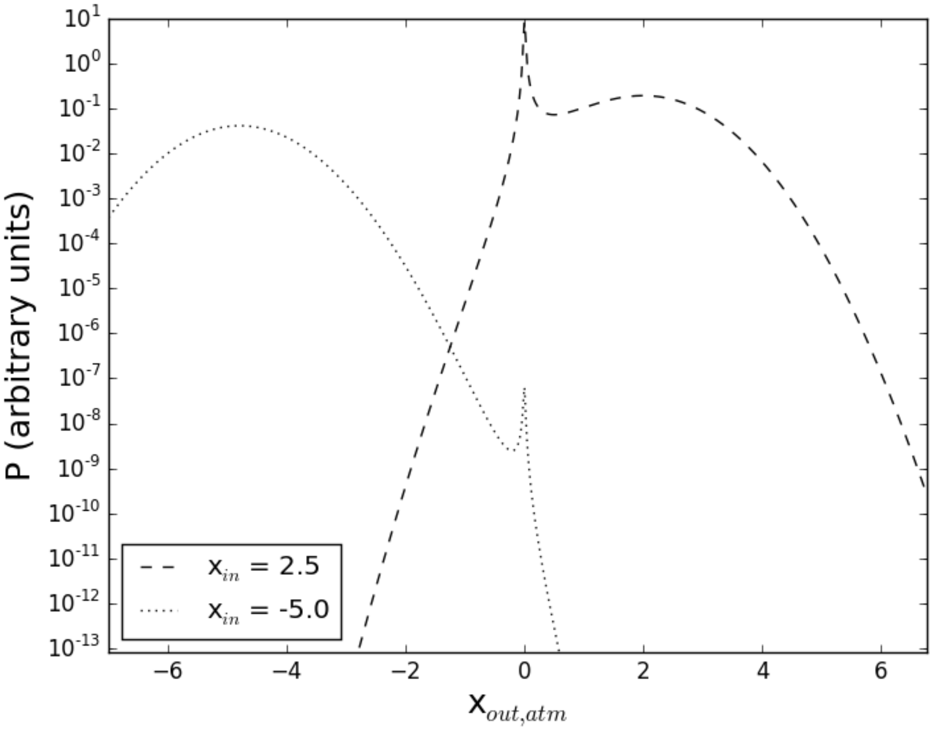

Figure 3.6 $P(x_{atm}|x_{\text{in}})$, the probability that a scattering atom will receive a photon with x_{in} at x_{atm} in its own frame. When $x_{\text{in}} = 2.5$, the distribution is strongly peaked around 0, indicative that there are many atoms available which can absorb the photon in the core of the line. As $|x_{\text{in}}|$ becomes large, few atoms are moving at speeds sufficiently high to absorb the atom in its core and it becomes much more probable that the atom will absorb the photon in its wing.

appeared precisely in its line center. This is because at $x_{\text{in}} = 2.5$ which corresponds to an atom's velocity of $2.5v_{th}$, there are still a large number of atoms moving at these speeds to which can scatter the photon in the core of its own absorption line. As $|x_{\text{in}}|$ becomes larger, this probability becomes small and in the case of $x_{\text{in}} = -5.0$ in Figure 3.6, it becomes much more probable that if absorbed, a photon will be absorbed in the Lorentz wings, enhancing its probability of escape.

So far, we have neglected any processes which can destroy Lyman-α. Absorption by dust is considered dominant in high metallicity environments, but in dust-free scenarios such as those arising in the early universe, processes still exist which can reduce Lyman-α luminosities (see e.g.

Dijkstra 2016a, 2016b). Lyman-α can be destroyed if a photon is absorbed by a hydrogen atom and collisionally de-excited to the 2s state. The probability of this taking place per scattering is

$$P_{\rm dest} = \frac{n_p C_{2p2s}}{n_p C_{2p2s} + A_\alpha},$$

where

$$C_{2p2s} = \frac{8.63 \times 10^{-6}}{\sqrt{T}} \Omega e^{-E_\alpha} kT$$

is the collisional coefficient from the 2p to 2s levels. For the densities in our problem ($\sim 10^3$ g cm^{-1}), we find this effect negligible in agreement with previous studies (Dijkstra 2016a). We further consider destruction of Lyman-α via photo-ionization. A Lyman-α photon can be absorbed by an excited hydrogen atom which leads to its ionization, a process which can effectively destroy Lyman-α. At our densities and our Lyman-α luminosities, this effect is also negligible when a full non-LTE treatment of the level populations is carried out. These effects are safely ignored in this study.

3.4.2 Numerical Scheme

Our Monte Carlo treatment may be summarized in the following steps. Note that the R_i's below are uniform random numbers drawn from [0, 1).

1. Draw $\tau = -\ln R_1$ to determine the optical depth penetrated by the photon of interest. Because our optical depth varies as a function of position along a ray (on a grid-based domain), we integrate optical depth cell-by-cell along the ray, subtracting accumulated optical depth from τ. At the beginning of each integration, it is determined if the photon has sufficient τ to cross the cell, given its position and direction. If not, the distance achieved by the photon with its remaining optical depth is determined and the photon has arrived at the location where it is scattered. Checks are carried out to see when the photon leaves the grid. Departing photons are eliminated from the calculation.

2. We choose an exit direction of the reemitted photon $\mathbf{n}_{\text{out}}$.

3. We determine the components of the scattering atom's velocity. Components of the velocity perpendicular to the direction of the incoming photon are selected from a Gaussian distribution via a Box-Muller transform. This provides atom velocity in doppler units. The parallel component of the velocity is selected via a scheme detailed in Zheng & Miralda-Escude (2002). The numerical implementation of their method is laid out explicitly in the last paragraph of their appendix and so we do not include it here. The only element of their prescription which is not included is their definition of μ_0, which we have taken from Barnes (2009).

4. The new photon frequency (in the frame of the fluid) is calculated via equation (3.7). In our code, we choose to carry out the calculation on the plane spanned by the incident photo direction and the atom's velocity. In this plane, there is a parallel component of the velocity u and a perpendicular component w. This allows us to calculate the outgoing frequency x_{out} via

$$x_{\text{out}} = x_{\text{in}} - u + u\mu + w\sqrt{1-\mu^2}, \tag{3.9}$$

where $\mu = \cos\theta$ and θ is the angle between $\mathbf{n}_{\text{out}}$ and $\mathbf{n}_{\text{in}}$.

5. Deboost into the lab frame with

$$x = x_{\text{out}} + \frac{\mathbf{v}_f \cdot \mathbf{n}_{\text{out}}}{v_{th}}.$$

Steps 1-5 are repeated until a satisfactory number of photons leave the simulation domain.

Note that the above scheme does not take into account any processes which destroy Lyman-α. Some of these processes are present even in metal-free and dust-free environments and methods for treating these will be detailed below. This scheme also assumes steady-state Lyman-α emission, partially evidenced in the fact that we have taken no thought to calculate differences in arrival times of photons, etc.

We calculate the Lyman-α spectra via a next-event estimator or a “peel-off” method. In this method, a virtual CCD is placed with some orientation to the simulation domain. This CCD has a size such that the positions of all photons which have not escaped the simulation domain may be projected onto this surface. At each scattering, we calculate the probability that the photon will be able to arrive at the CCD via

$$P = e^{-\tau},$$

where τ is calculated from the photon’s position through the simulation domain to the CCD. In our case, we place the CCD parallel to a coordinate axes with a pixel count equal to the base resolution[5] of the simulation domain (256×256) where each pixel has a 100 bin spectrum. While the position of the photon on the CCD is trivial to calculate in our case, the photon’s frequency must be determined via (3.7) with $\mathbf{n}_{\mathrm{out}}$ in the direction perpendicular to the CCD at each scattering. The contribution of a photon to its pixel at a given frequency is given by its probability.

3.4.3 Test Problems

A number of basic tests for Lyman-α codes exist. In this section, we demonstrate the code’s capability in classic static slab test and we mention that the reproduction of the redistribution function in Figure 3.5 constitutes a standard test in the literature.

We test our code for the static slab test case. Details of this test are included in Zheng & Miralda-Escude (2002) and are frequently summarized in studies involving Lyman-α transfer. Photons are placed in the x, y plane in the line center $\nu_0 = 2.466 \times 10^{15}$ Hz. Photon packets are given randomly oriented directions in 3D space. The entire domain is held at 10 K with no bulk fluid velocity. We set the density of the fluid n_H such that $\tau_0 = \sigma_0 n_H \Delta x = \sigma(x = 0, 10K) n_H \Delta x = 10^4, 10^5, 10^6$, where Δx is the half-thickness of the slab, i.e. the distance between the emitting center plane and the edge of the simulation domain. The quantity τ_0 is the line-centered optical

---

[5] i.e. without AMR

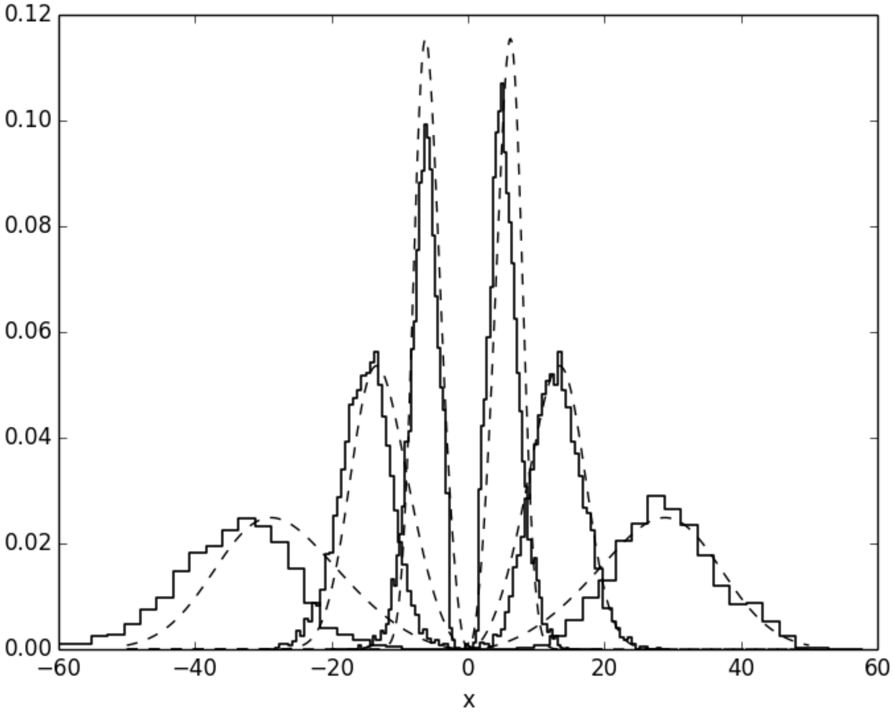

Figure 3.7 Static slab lyman-α transfer test. The numerical solution for $\tau_0 = 10^4$ (innermost peaks), $\tau_0 = 10^5$ (next innermost) and $\tau_0 = 10^6$ (outermost peaks) appears in solid, step style with the exact solution from (3.10) superimposed as dashed curves. The agreement is acceptable with deviations appearing at greater optical depths.

depth from the edge of the domain to the emitting center plane. Clearly n_H is only unique up the arbitrary choice of Δx. We set $\Delta x = 1$ for our test case.

The static slab problem enjoys an analytic solution for choice of domain temperature T (and hence a via equation (3.4)) and problem line-centered optical depth τ_0. The solution $J(x)$ in doppler coordinates x was determined by Harrington (1973) to be

$$J(x) \propto \frac{x^2}{1+\cosh(\sqrt{\pi^3/54}|x|^3/a\tau_0)}, \tag{3.10}$$

which can be integrated and normalized. In Figure 3.7, we plot the numerical solution for $\tau_0 = 10^4$ (innermost peaks), $\tau_0 = 10^5$ (next innermost) and $\tau_0 = 10^6$ (outermost peaks) superimposed on the analytic solution (dashed lines). The agreement is acceptable with deviations appearing at greater optical depths.

3.5 Discussion and Conclusions

CR7 is the brightest Ly-α emitter known at $z > 6$. At a redshift of $z = 6.6$ it is estimated to have a Ly-α luminosity $L_{\mathrm{Ly}\alpha} > 8.0 \times 10^{43}$ erg s^{-1} with a narrow line width of $\sim 266 \pm 15$ km s^{-1}. The HeII 1640 Å line is luminous $L_{\mathrm{HeII}} \simeq 2.0 \times 10^{43}$ erg s^{-1} with a width of 130 ± 30 km s^{-1}. This implies a large $L_{\mathrm{HeII}}/L_{\mathrm{Ly}\alpha}$ ratio $\simeq 0.22$ (Sobral et al. 2015) which is strongly suggestive of a hard ionizing spectrum (Pallottini et al. 2015).

By $z = 6.6$, our halo has acquired 3×10^{10} M$_\odot$ and the 3162 M$_\bullet$ initial seed has grown to 3.23×10^7 M$_\odot$. In our cosmological model, CR7 is situated on a major filament and is fed strongly aspherically (see Figure **??**). Recombinatory Lyman-α emissivity originates from the inner ~ 3 kpc while HeII 1640 Å emission appears in the direct vicinity of the BH. In Figure 3.2, we plot azimuthally averaged number densities of primordial species as a function of radius and overlay gas temperature in blue. Throughout the halo, temperatures and gas pressures are prohibitive for

Table 3.1. Observations vs. Simulation

	Observations		Simulation	
Line	Luminosity	FWHM	Luminosity	FWHM
Lyman-α	$> 8.3 \times 10^{43}$	266 ± 15	1.0×10^{44}	310
HeII 1640 Å	2.0×10^{43}	130 ± 30	2.4×10^{43}	210

Note. — Line luminosities and length widths (FWHM) are given in erg s^{-1} and km s^{-1} respectively. Observed line widths and strengths adopted from Sobral et al. (2015).

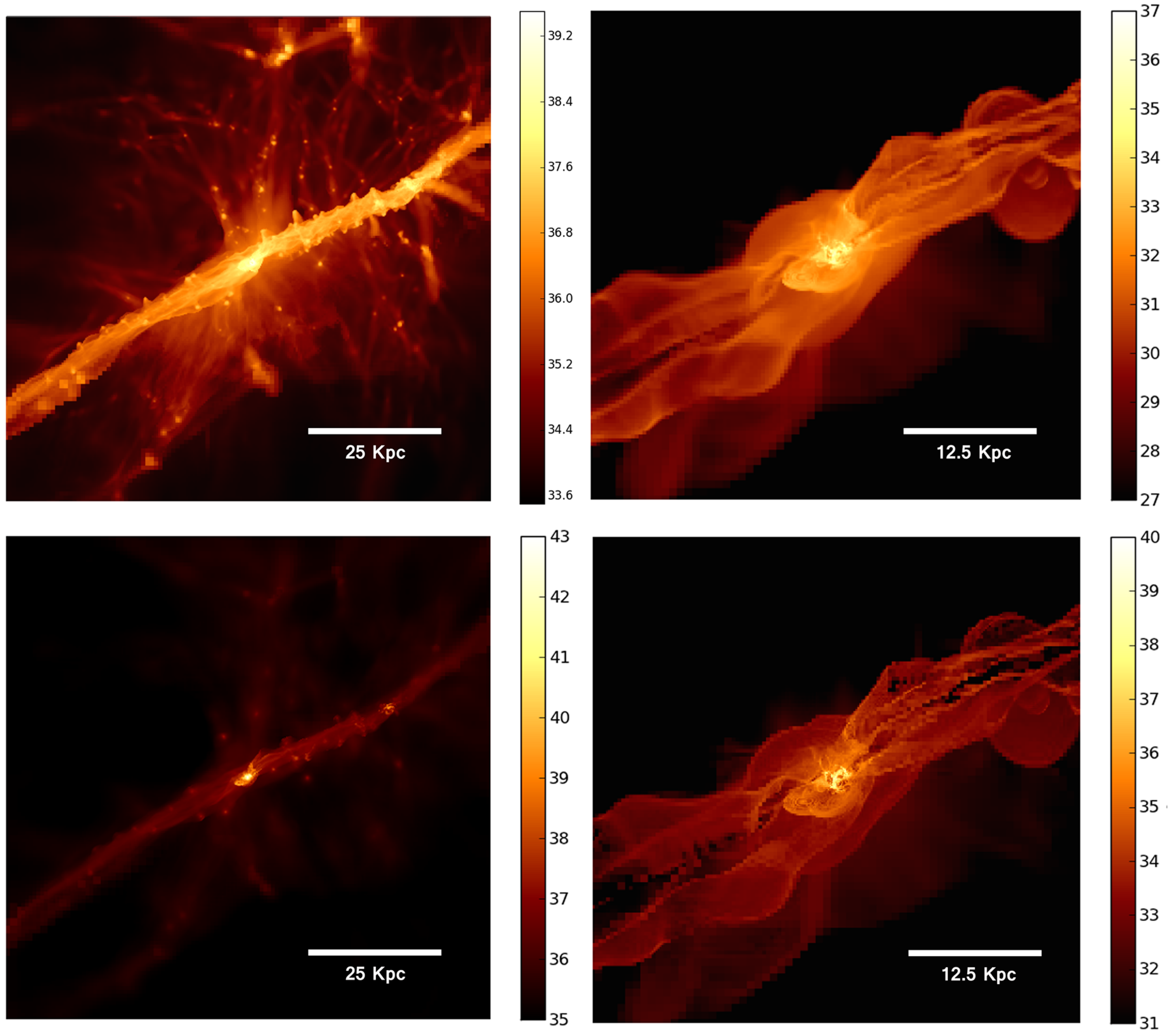

Figure 3.8 Projection of logarithm of emissivity [erg s^{-1}] in Lyman-α (left panels) and HeII 1640 Å (right panels). In the top panels, we plot emissivity due to radiative recombination. In the bottom panels, we plot emissivity due to collisional excitations. Note the difference in color scales.

star formation.[6]

---

[6] We note, however, that, using somewhat different prescriptions to model accretion and radiative feedback, Aykutalp et al. (2014) find that star formation may occur in some cases.

We summarize our results in Table 3.1. At at $z = 6.6$, the instantaneous Lyman-α emissivities in our model due to recombination and collisional excitation are 7.6×10^{43} and 4.2×10^{44} erg s^{-1}, respectively. The total Lyman-α after taking into account collisional de-excitation and photo-ionization of excited hydrogen by Lyman-α and He II 1640 angstrom luminosities are 2.4×10^{43} and 1.0 $\times 10^{44}$ erg s^{-1}, respectively. This renders our model a luminous Lyman-α source with 12.9% of the total AGN luminosity becoming Lyman-α. In principle, Lyman-α efficiencies of up to $\sim 30\%$ may be achieved in AGN environments (Baek & Ferrara 2003). The FWHM of the HeII 1640 Å line is 210 km s^{-1} which is broader than observations (130 ± 30 km s^{-1}) while Lyman-α exhibits a width of 310 km s^{-1} after MC post-process which is in rough agreement with observed values of $\sim 266 \pm 15$ km s^{-1} (see Figure **??**). This is achieved with $M_\bullet = 3.23 \times 10^7$ $M_\odot$, $\dot{M}_\bullet = 0.16$ $M_\odot$ yr^{-1} and $L_\bullet = 7.87 \times 10^{44}$ erg s^{-1}.

The HeII 1640 Å and Lyman-α lines in CR7 are offset in velocity space by $\Delta v = +160$ km s^{-1} (Sobral et al. 2015). 1D calculations by Smith et al. (2016) are able to reproduce this offset by demonstrating that a luminous central source with a hard spectrum drives an outflow which would separate HeII and Ly-α emission in velocity space. Our model does not incorporate feedback from Lyman-α, but we are able to reproduce an offset by selecting a fortuitous viewing angle of our 3D model which has a complex bulk-fluid velocity and density field. The Lyman-α spectrum varies from effectively single (solid line) to double-peaked (dashed line) depending on the orientation of observations. The major feature in the spectrum which agrees best with the observed spectrum of CR7 (solid line) is asymmetric and offset with respect to the HeII 1640 Å emission as is observed (Sobral et al. 2015) though our offset (+305 km s^{-1}) is larger than CR7's (+160 km s^{-1}). An expanding shell of material is not evident in our model. There are several possible explanations for this. Our CR7 model is largely ellipsoidal, not spherical, being compressed along the direction of the angular momentum vector. This strong flattening of the system allows for radiation to escape CR7 through higher angles of latitude.

We note that Population III stars are expected to produce nebular Lyman-α emission principally from recombination, and not from collisional excitation as is the case for the harder X-ray spectrum emitted from an active black hole. We estimate an upper limit for the Lyman-α luminosity of 1.14×10^{44} that could be generated by recombination emission powered by Population III stars, by assuming both that the gas within the halo is fully ionized.[7] This is only luminous enough to explain the CR7 luminosity if the Lyman-α escape fraction is $f_{\rm esc}\simeq 0.8$, much higher than previously estimated (e.g. Hartwig et al. 2015). This, along with the extremely high star formation efficiency of $\simeq 0.1$ that is required for Population III stars to explain the observed emission (Visbal et al. 2016; Smith et al. 2016), poses a strong challenge to this alternative model for CR7.

While Ly-α is extended on the kpc scale, much of the helium emission in our model originates from the vicinity of the BH. We find that to maintain line widths ~ 100 km/s in agreement with CR7 requires that the line be only broadened by virial velocities of bulk fluid motion and thermal broadening. Our models with more massive BHs both diminish and broaden HeII 1640 Å emission, in some cases giving rise to a double-peaked profile which characterizes line observations of expanding shells of gas. The complex line profiles are not observed in CR7 which suggests an upper limit on BH luminosity in models of CR7 powered by an accreting BH.

Could CR7 be detected in the radio? Our estimate of the accretion rate (0.25 Eddington) suggests the BH is accreting within the "thin disk" regime or "quasar mode" (e.g. Dubois et al. 2011) where the prospects of launching a relativistic jet and powering radio lobes remains unclear. Yet radio synchrotron emission could originate on scales of 100s of Schwarzschild radii from relativistic accretion shocks. For our values of $M_\bullet$ and $\dot{M}_\bullet$ in the analytic model by Ishibashi &

---

[7] For this estimate we have adopted the density field extracted from our simulation. If the gas is significantly more dense in the halo in the case of Population III star formation, then the luminosity in recombination lines could be higher due to the higher recombination rate. That said, the strong photoionization feedback from massive Population III stars would likely drive down the density of the gas very quickly after the formation of the stars (e.g. Whalen et al. 2004).

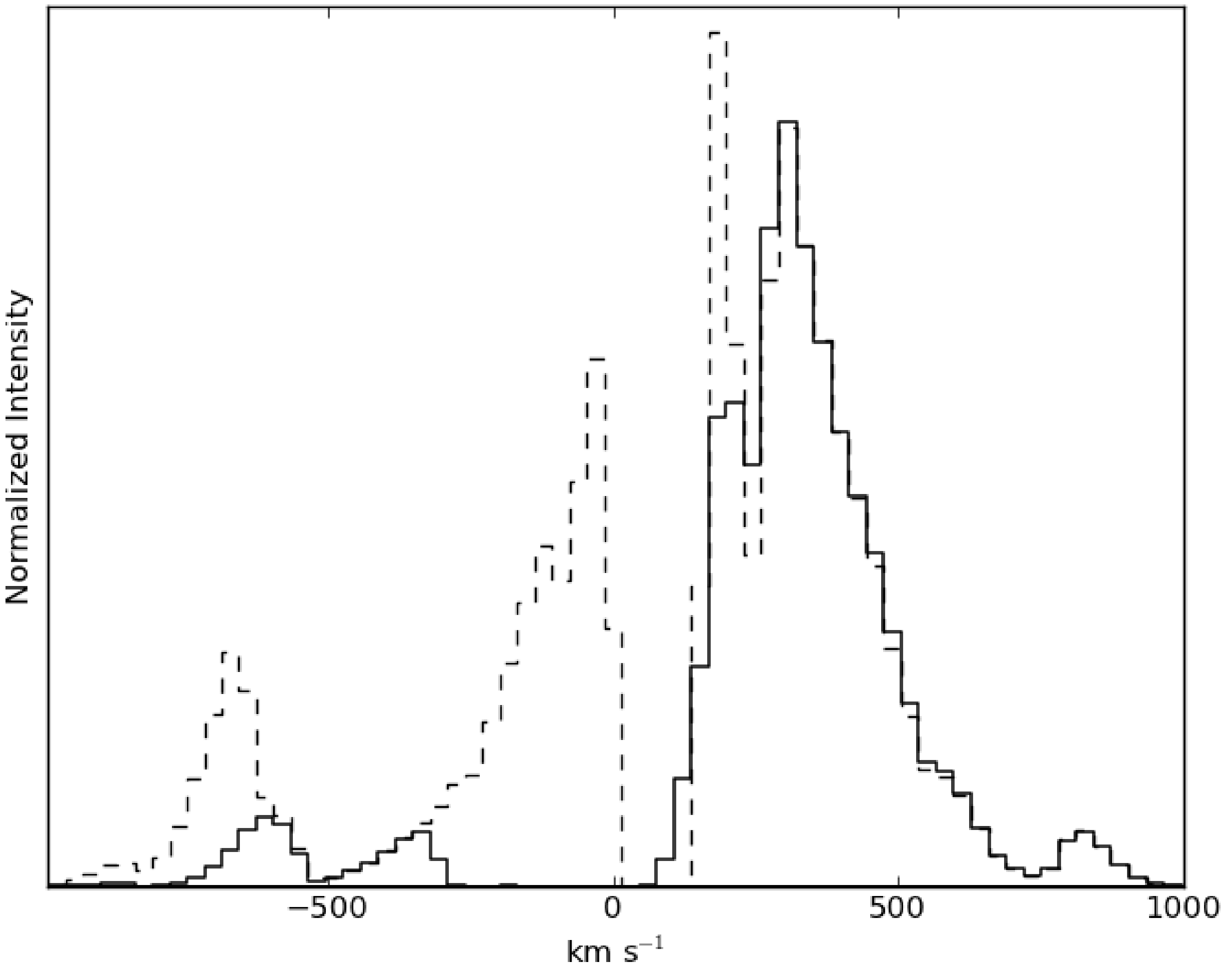

Figure 3.9 Lyman-α line profiles for two perpendicular viewing angles of the CR7 model after Monte Carlo radiative transfer post-processing through the simulation domain assuming steady state emission (i.e., we only post-process a single data dump at $z = 6.6$), with a peel-off scheme (e.g. Zheng & Miralda-Escude 2002). The spectrum most closely resembling CR7 (solid line) has only a single peak while from other viewing angles, two peaks might be observed (dashed line). The major, offset Lyman-α feature has a FWHM of 310 km s^{-1} in approximate agreement with observations. Though our model predicts a velocity offset, we do not obtain the observed 160 km s^{-1} offset for Lyman-α with respect to the HeII 1640 Å line. (see text).

Courvoisier (2014) and adopting the authors' estimates for electron spectral index p and ambient magnetic field B, we estimate a synchrotron luminosity of $\sim 1.0 \times 10^{39}$ erg s^{-1} arising from subgrid scales. The total observed radio flux density S_ν of CR7 integrated over the source is

$$S_\nu = \frac{P_{\nu_0}}{\nu_0 \cdot 4\pi D_L^2 (1+z)^{\alpha-1}} \tag{3.11}$$

where P_{ν_0} is the power radiated at frequency ν_0, D_L is the luminosity distance, ν is the frequency of observations related to the emitted frequency ν_0 by the doppler shift. We take $\alpha \approx 1.5$, accounting for the $z \sim \alpha$ correlation for steepening radio spectral indices with increasing redshift ($\alpha \simeq 0.7$ at $z = 0$; see Cavagnolo et al. 2010; Condon 1992) for emitted frequencies at 10.0 GHz. For sensitivites of a few μJy per beam in L-band ($\nu \simeq 1.3$ GHz), this imposes a detection limit of $P_{\nu_0} \simeq 10^{41}$ erg s^{-1}. This quantity is mildly sensitive to the choice of α; for local-universe values, the detection limit becomes $P_{\nu_0} \simeq 10^{40}$ erg s^{-1}.

Scaling relationships for accretion, jet power and radio luminosity exist in the literature. If we insert our active galactic nuceli (AGN) luminosity in X-rays and $\mathrm{M}_\bullet$ into a model by Merloni et al. (2003) which is based on a thoery of scale-invariant jets (Heinze & Sunyaev 2008), we obtain a log-mean radio luminosity of $P \approx 1.4 \times 10^{40}$ erg s^{-1} though their model suffers from very large scatter, spanning a few orders of magnitude. If we apply our data to the models of Meier (2001), adopting the thin disk regime for the Schwarzschild case (his equation 4), we obtain a jet power of $\sim 1.0 \times 10^{41}$ erg s^{-1}. If we utilize the relation between jet power and radio output found in Cavagnolo et al. (2010), this corresponds to a radio luminosity of only 10^{35} erg s^{-1}. Our BH is accreting at an appreciable fraction of Eddington, and such disks can be unstable and oscillate between low, hard (LHS) state where radio brightness is expected to increase and high, soft (HSS) state. At a reduced accretion rate of 0.1 Eddington, jet power for a rotating black hole would be $> 10^{44}$ erg s^{-1} corresponding to a radio luminosity of $P_{\nu_0} \simeq 2.0 \times 10^{42}$ erg s^{-1} which would be detectable in μJy observations. Such jets may drive outflows and could be responsible for the 160 km s^{-1} offset of the Ly-α line from the systemic velocity. Any luminous radio emission from CR7 is likely to be evidence of AGN activity, as synchrotron emission in star formation regions primarily arises from supernova remnants which are thought to be absent in CR7 from the lack of observed metals.

Our work provides important additional support for the massive BH model of CR7 via detailed radiation hydrodynamic cosmological simulations.

CHAPTER

FOUR

THE HYDROXYL-WATER MEGAMASER CONNECTION

> *If there is magic in this world, it is contained in water.*
>
> Loren Eiseley

4.1 Introduction

MASERs (microwave amplification by simulated emission of radiation) are monochromatic, intense radio sources originating from population inversion in clouds of molecular gas. Masers occur astrophysically and are typically associated with star formation, YSOs (e.g. Johanson, Migenes & Breen 2014; see session 5, IAU Symp. 242, 2007) and late type stars in our local galaxy (e.g. Vlemming et al. 2005). Luminous masers which are observed at extragalactic distances are termed *megamasers*, and widely appear in either hydroxyl (OH; mostly 1665 MHz and 1667 MHz from the hyperfine levels in the ground rotational state $^2\Pi_{3/2}(J = 3/2)$) or water (22.23508 GHz; $6_{16} \rightarrow 5_{23}$) molecules[1], and are typically associated with mergers, starbursting and active galactic

---

[1] Although the detection of a methanol megamaser has been recently reported, e.g. Chen et al. (2015)

nuclei (AGN) activity (for a review, see Lo 2005).

Megamasers are remarkable probes of extragalactic phenomena. The parsec-scale environments around supermassive black holes have been probed (e.g. Greenecet al. 2013; Kuo et al. 2011; Reid et al. 2009) and Hubble's constant has been constrained (e.g. Humphreys et al. 2013; Reid et al. 2013; Kuo et al. 2013; Braatz et al. 2010; Herrnstein et al. 1999) through observations of extragalactic water. Hydroxyl (OH) megamasers have been utilized to trace star formation and to estimate the galaxy merger rate (e.g. Darling 2002). Megamasers further possess the exciting potential to be diagnostics of galaxy evolution at high z where other properties of the host galaxy cannot be resolved (Pihlström 2007).

Unfortunately, megamasers are rare and the precise relationship between megamasers and global galactic processes remains enigmatic. So far, over 4000 galaxies have been searched for 22 GHz water emission with only 150 detections and nearly 500 galaxies have been surveyed for hydroxyl emission with 120 detections (see Wagner 2013 and references therein). Many attempts to link megamasing of either molecular species to other galaxy observables have largely been met with only modest success (e.g. Darling & Giovanelli 2006; Zhang 2012; Zhu 2011), but significant connections have been achieved, linking OH megamasers to large dense gas fractions (Darling 2007) and water emission to high column densities (Zhang et al. 2006; Castangia et al. 2013), large X-ray luminosities (Kondrakto e al. 2006) and high corrected [OIII]/Hβ (Constantin 2012). Luminous OH emission is frequently powered by starbursting in LIRG/ULIRG galaxies while water megamasers are usually associated with AGN (Lo 2005).

Though AGN and starbursting activity frequent the same galactic nucleus (e.g. Dixon & Joseph 2011; Wild et al. 2010), very luminous OH and H_2O emission were not until recently observed in the same galaxy (Wagner 2013; Tarchi et al. 2011, hereafter T11). This observation led to the hypothesis that OH and H_2O exclude each other due to the different and respectively restrictive conditions each molecule demands for masing (see Lo 2005, Lonsdale 2002). However, water emission has since been discovered in multiple regions in Arp 299 including Arp 299-A (IC 694), a galactic nucleus also hosting an OH megamaser (T11). Another possible dual megamaser candidate, IIZw96, was found in a tentative water detection by Wagner (2013). It is thus unclear whether galaxies hosting dual megamasers are experiencing a brief phase of galaxy evolution (such as a transition from starburst nucleus to an AGN) or whether the relationship between the two megamaser species is more complicated than previously believed.

The frequency of simultaneous OH and H_2O has previously been somewhat badly constrained as many masing galaxies have yet to be searched for emission in the remaining molecule. Of the nearly 4500 galaxies searched for maser emission in either molecule, ~ 90 have been searched for masers of both species (see Tarchi 2012; Wagner 2013). Of those which have been searched and have emission in at least one molecule (~ 60), the majority (38) only emit in water while 18 are only OH emitters. The number of extragalactic OH megamasers surveyed for H_2O emission is thus somewhat under-sampled in the literature.

Where previous work has attempted to link megamaser luminosities with galaxy observables, ours is the first survey of which we are aware which aims to exclusively address the question of the relationship between the two megamaser species. Here we present results of a survey of known OH megamaser hosts for 22 GHz water emission to probe the dependency of H_2O emission on conditions sufficient for OH megamasers.

This chapter is structured as follows. In §2, we outline our survey sample. In §3 we outline our observations. §4 contains our data reduction and analysis procedure. In §5 we discuss in turn galaxies toward which we detected 22 GHz emission. In §6, we outline the effectiveness and limitations of our survey. We present statistical results from our survey and their implications for the OH and H_2O megamaser connection in §7 and conclude in §8.

4.2 The Sample

Our sample is taken from T11 and consists of the subset of their galaxies which are established OH emitters observable by the GBT which had never been observed for H_2O emission or for which significantly tighter upper limits on 22 GHz emission might be obtained. Due to observing time limitations, rise times of objects, and RFI, we carried out observations for 22 GHz emission for 47 galaxies hosting OH masers. Figure 4.1 summarizes nuclear activity and distribution in redshift z of sample members. Nuclear activity types are fairly well-represented in z, mitigating sensitivity biases for detections in a particular group. We note that OH megamasers are fairly uniformly distributed in galaxy activity type (i.e. HII, LINER, Seyfert), occupying roughly the same optical population as (U)LIRG galaxies (Darling & Giovanelli 2006), so our sample is decently representative of the OH maser/megamaser population.

4.3 Observations

Observations were carried out at the Robert C. Byrd Green Bank Telescope (GBT) between the dates of Feb 27 and April 6, 2014 under project code AGBT14A_381. We utilized the GBT spectrometer backend and observed with two 200 MHz bands, the first band being centered on systemic velocity and the second offset by 180 MHz toward lower frequencies. Each band contained 8192 spectral channels giving a velocity resolution of 0.366 km s^{-1} at 20 GHz. Spectra were taken by nodding between beams 3 and 4 of the KFPA receiver every 2.5 minutes for a 5 minute nod cycle. The telescope was pointed and focused every 30-60 minutes or whenever the telescope slewed more than a total of 10 degrees on the sky. System temperatures were typically 40-60 K. With few exceptions, observations were carried out above elevations of 30° over the horizon with objects closer to the horizon experiencing increases in system temperatures and compromises in RMS sensitivity.

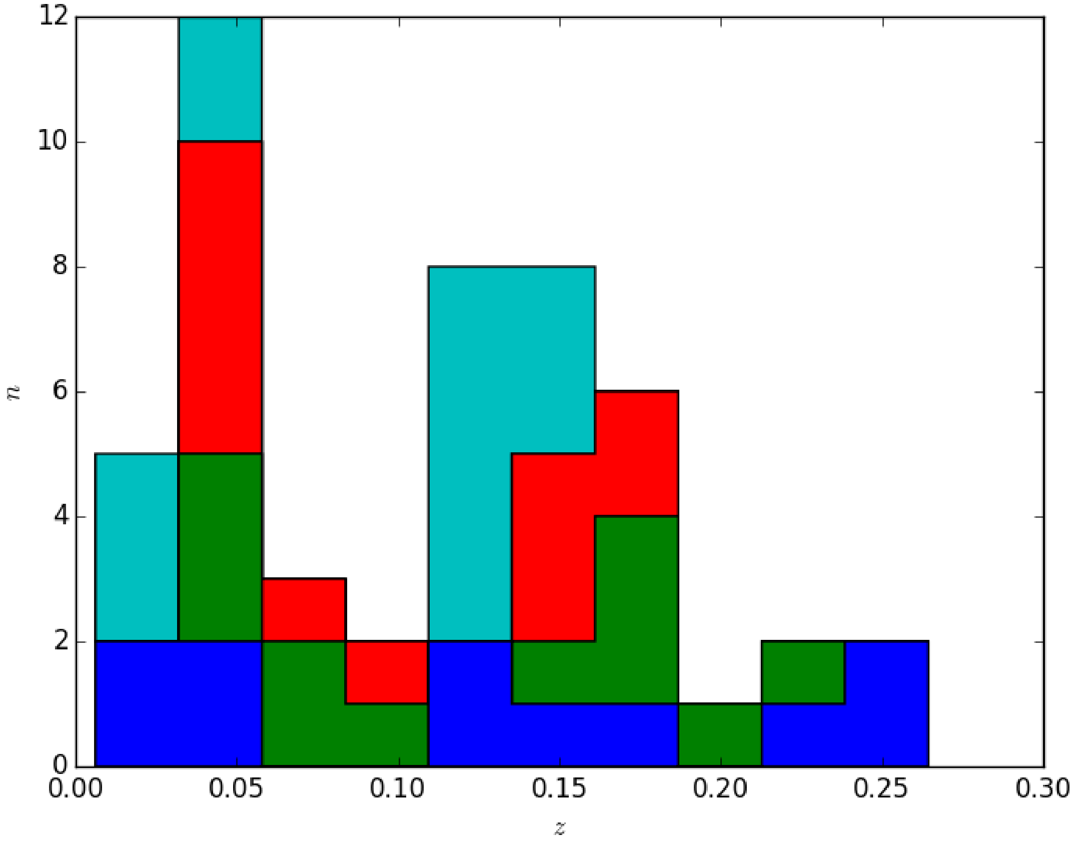

Figure 4.1 The distribution of sample galaxies in redshift z labeled by nuclei type as reported by the NED database. Seyfert-type AGN are in blue, LINER-type AGN appear in green, HII nuclei in red, and galaxies for which no NED classification was available appear in cyan. All galaxies in our survey sample were OH maser hosts. All populations in our sample are relatively well represented in redshift z.

The project was granted ∼ 60 hours of telescope time divided into 8 epochs. Good observing conditions and zenith opacities (0.02 - 0.03) were enjoyed over the course of the observations. All objects were observed in LL and RR circular polarizations which were averaged to produce final spectra. To test our setup, we successfully observed the bright water megamaser in Mrk 1029.

We encountered a bright RFI source from a pair of satellites[2] which prevented observations of all the galaxies on our source list. We were the first observers to encounter this RFI which likely arose from detecting the side lobes of one or both of these satellites which had recently began servicing nearby locales. The RFI persisted over our ∼ 1.5 months of observations. These effects were mitigated by restricting observations to certain portions of the sky.

4.4 Data Reduction and Analysis

Most data reduction was carried out with GBTIDL on NRAO Green Bank computing platforms. Local weather conditions were determined from the GBT CLEO tool, which estimates zenith opacities by averaging weather data over 3 surrounding stations. Amplitude calibration was carried out with appropriate calibrators in Ott et al. (1998). Spectra were then examined band by band and flagged for obvious signs of RFI. 15 of our 61 observed sources were sufficiently damaged by RFI that no constraints on 22 GHz water emission could be achieved. Each of our nod scans in a given observation (including those across multiple nights of observation) were then averaged. Non-emitting portions of the averaged spectrum were fit with 3rd order polynomial to flatten baselines. During inspection, reference spectra were smoothed with 16 channel boxcar routine to bring out weaker features, though we found that this sometimes introduced spurious spikes in the data. All apparent signals were verified against the spectrum without reference spectral smoothing. All spectra were immediately smoothed with a 4 channel boxcar scheme which was successful in eliminating about half the noise.

---

[2] http://www.spectrumwiki.com/wiki/DisplayEntry.aspx?DisplyId=45, http://www.spectrumwiki.com/wiki/DisplayEntry.aspx?DisplyId=109

Because masers detected in this paper had a distinctly non-gaussian character, line fluxes were first calculated within GBTIDL using their `stats` procedure, and then subsequently calculated using a numeric integrator based on Simpson's rule. We assume our survey is sufficiently sensitive to detect the flux from a $\sim 3\sigma$ peak with a FWHM of 2 km s−1 (approximately 5 channels; see Wagner 2013). Upper limits for isotropic luminosities of masers can then be estimated with the method in Bennert et al. (2009), i.e.

$$\frac{L_{H_2O}}{L_\odot} = \left[0.023 \times \frac{W}{\mathrm{Jy\ km\ s^{-1}}}\right] \times \frac{1}{1+z} \times \left(\frac{D_L}{\mathrm{Mpc}}\right)^2,$$

where W is the sensitivity of the survey which we took as the integrated volume of our 3σ Guassian curve with a FWHM of 2 km s^{-1}. We estimate our errors in calibration to be between $10-15\%$.

4.5 Results and Discussion

Our observations are summarized in Table 2. We include all observed sources in this table, including 15 sources badly damaged with RFI, for which upper limits on emission could not be achieved. Note that RMS sensitivities reported are 1 σ for the entire band after boxcar smoothing. Of the 46 uncompromised sources observed, we detect confident water emission toward one source and we set new upper limits for water emission on 45 galaxies, 40 of which have yet to be observed for 22 GHz emission. We now discuss our sole maser detection.

4.5.1 IIZw96

IIZw96 is a complex merger between at least two galaxies. The OH megamaser is offset from obvious galactic nuclei (Migenes et al. 2012), in a $\sim 10^9 M_\odot$ reddish clump of gas. Soft X-ray emission and strong IR emission lines (Goldader et al. 1997) suggests this clump is an extra-nuclear, obscured starburst, similar to that found in Arp 299, regions C and C' in T11 (Imani et

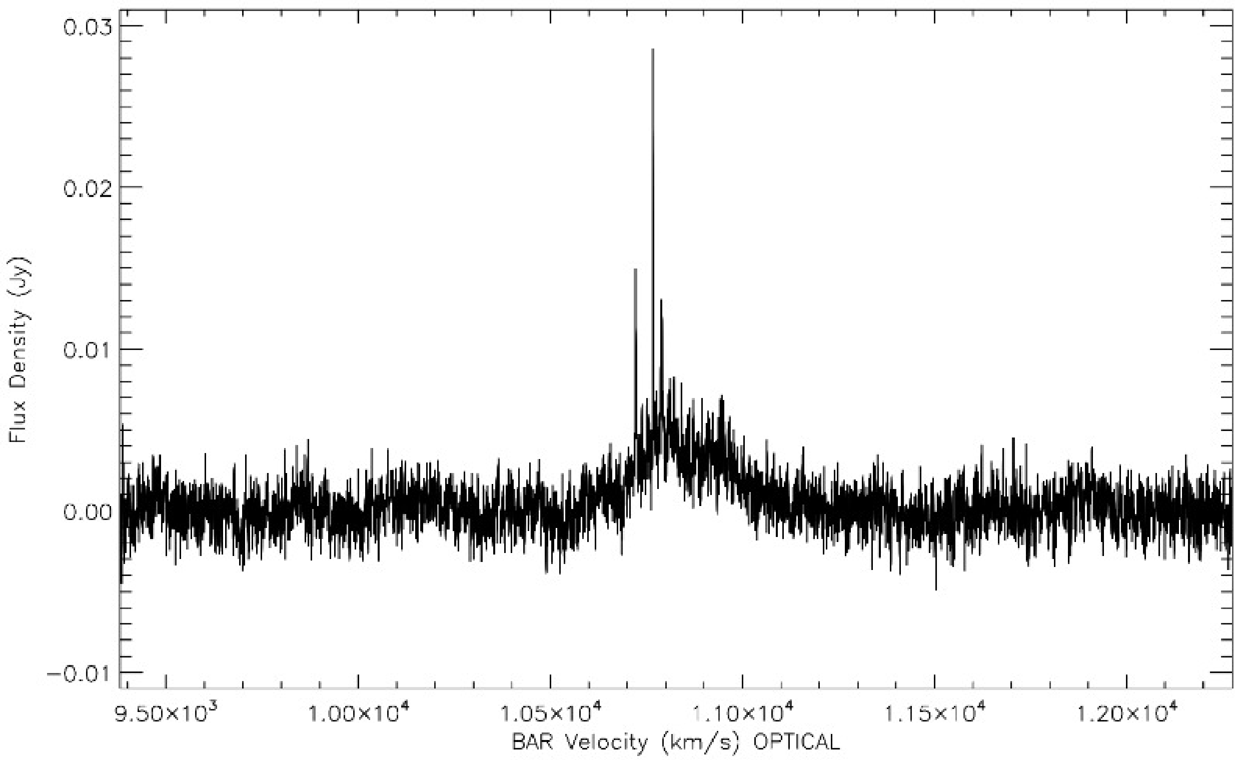

Figure 4.2 22 GHz line detection toward IIZw96 after 1 hour of integration, baseline removal and 4 channel boxcar smoothing. RMS noise is 1.22 mJy. This figure was generated in GBTIDL.

al. 2010). IIZw96 resembles Arp 299 morphologically: Goldader et al. (1997) observes that both galaxies possess similar projected size (10-15 kpc), and are composed of distinct nuclei which are strongly interacting and are in a similar, very short ($\sim$ 10 Myr) “intermediate" stage of merging.

Water emission toward IIZw96 was tentatively detected by Wagner (2013) but could not be confirmed above 5σ as integration time was only 12 minutes. In Figure 4.2, we present the IIZw96 feature after approximately an hour of integration. This generous observation time was sufficient to resolve the finer features of the water maser which were not previously detected. The ~ 500 km s^{-1} profile exhibits a double-humped character in agreement with Wagner (2013) but we do not detect his two side-lobes. We also obtain an isotropic luminosity somewhat smaller than Wagner (2013) at $\sim 400 L_{\odot}$ but the maser remains very luminous. This difference might be attributed to Wagner’s possible inclusion of tentative side bumps in the maser luminosity in addition to uncertainties in Wagner’s measurement arising from short integration times and possibly to short-term maser variability. Our observation confirms this detection beyond doubt ($\sim 8\sigma$) and establishes IIZw96 as the second system to host formal megamasers in both OH and H_2O species.

Ripples in the baseline of the spectrum of IIZw96 persist after baseline removal. The residual baseline structure is a time and frequency dependent ripple caused by some combination of RFI and system instability.

Wagner (2013) drew connections between IIZw96 and the water feature in NGC 2146 which is associated with star formation. With larger integration times, the line in IIZw96 better resembles the profile of Arp 299 itself (see Figure 4.5). We should carefully note, however, that Arp 299’s profile contains water emission from several regions within the merger (not just IC 694) and a similar situation could be the case with IIZw96. Because of this and the fact that water emission profiles are time-variable, no conclusive connections between the systems can be made without radio interferometric followups. As with Arp 299, we do not detect high velocity line emission in IIZw96. Our observations reveal narrow features in the water spectrum of IIZw96. Though

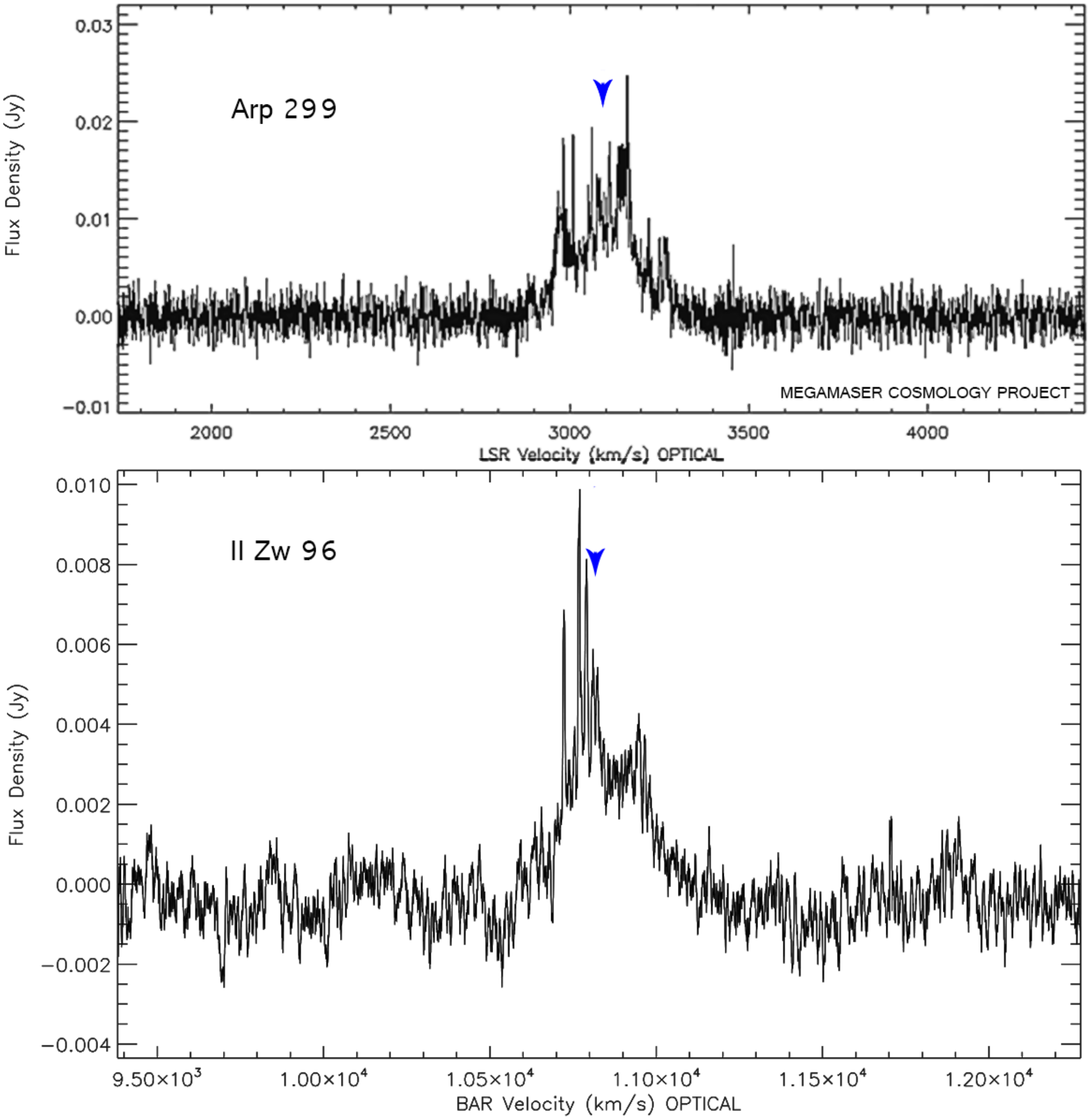

Figure 4.3 *Top Panel:* Water feature in Arp 299 adopted from the Megamaser Cosmology Project (`https://safe.nrao.edu/wiki/bin/view/Main/MegamaserCosmologyProject`). *Bottom Panel:* Water feature in IIZw96 after ∼ 1 hour integration time and 16-channel boxcar smoothing. The narrow features on the blue peak reach amplitudes of 28 mJy when 4-channel boxcar smoothing is applied. Systemic velocities are indicated with blue arrowheads. Note the different scales on vertical axes between panels. The figure was generated in GBTIDL.

IIZw96 is among the most powerful starbursts known (Inami et al. 2010), there is a possibility it also hosts an obscured AGN (Migenes et al. 2012) which could provide a pumping mechanism for the maser.

If water emission arises from more than one location in IIZw96, it may make the maser more difficult to detect via interferometric measurements, especially with VLBI, because if the already somewhat low flux is broken up into multiple spatial regions, longer integration times will be required to detect emission from any single region. However, the narrow lines in the water maser emission may suggest the presence of compact emission which would render such followup worthwhile.

4.5.2 IRAS 15179+3956

IRAS 15179+3956 has recently been observed for water emission (Wagner 2013) though integration times were short enough that follow up in this survey was justified. Unfortunately, our nearly 1 hour of observations on IRAS 15179+3956 was badly damaged by RFI with an RFI signal appearing close to the systemic velocity. After meticulous flagging of the data, a ~ 70 km s^{-1} feature still appears above the noise (Figure 4.4) offset from the systemic velocity by ~ 100 km s^{-1}. The precise luminosity of the source and the confidence of the detection cannot be naively estimated using the RMS of the band and the height of the peak as both the line volume and its height may be affected by correlations in the spectral data (i.e. ripples in the band). Indeed the feature could be a statistical blip atop an pronounced baseline ripple. Using basic integration techniques over the spectra gives a very bright water maser with an isotropic luminosity $\sim 130\ L_\odot$ which is in conflict with previous observations (Wagner 2013).

To investigate the legitimacy of the signal, we modeled the noise in the spectrum. Noise modeling is used frequently when attempting to discriminate a weak signal from detector noise to quantify the confidence of detection (e.g. Zemcov et al. 2014). This is usually carried out by carefully

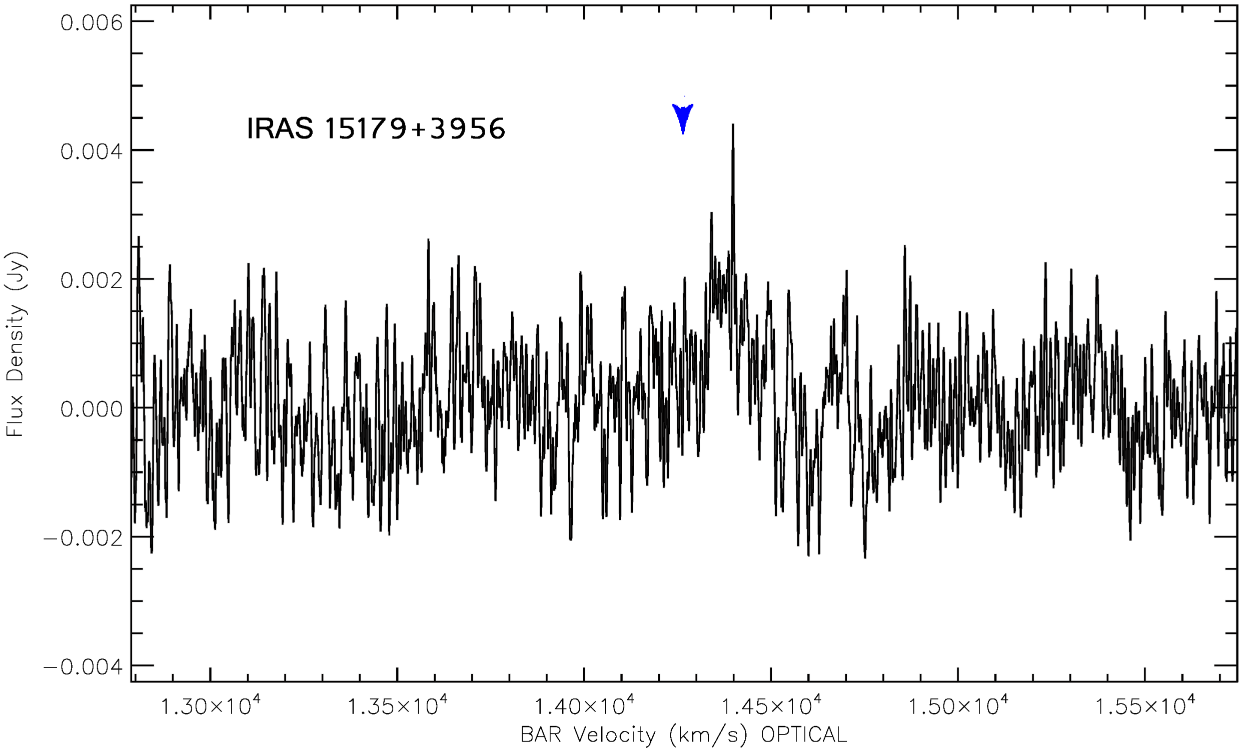

Figure 4.4 *Upper panel:* Apparent water maser detection toward IRAS 15179+3956. Spectrum is smoothed 4 channels with a boxcar routine. The systemic velocity is indicated with a blue arrowhead. The rms noise over the entire band is 1.18 mJy. This figure was generated in GBTIDL.

characterizing the noise in electronics and machinery of the detector. Here, we use a bootstrapping method, i.e. using the noise in the spectrum itself, to make consistent random realiations of the noise.

First, we confirmed the noise in the band to be Gaussian by verifying that the mean and skewness of the distribution is consistent with zero. Next, we quantifies correlations in the noise that might yield a false detection if one is not careful. For this we calculated the power spectrum of the dataset that revealed strong correlations in the underlying noise with power in the larger frequency (velocity) scales consistent with what one expects from harmonics in the KFPA receiver. We also broke the spectrum into 4 quadrants and verified that this harmonic ringing is robust across the whole data set. Next, we created Gaussian realizations of the spectrum consistent with the correlations of the data to determine how likely such random fluctuations could yield a false detection. We produced 100,000 simulated random spectra for this analysis. To demonstrate the effectiveness of this method in reproducing the character of the noise of the observations, we include three sample spectra in Figure **??**. Of those spectra which we simulated, only one in 120 achieved peak luminosities as large as our signal, implying strong evidence at 2.9σ that our signal is real. We thus present the feature in Figure 4.4 as a tentative detection of water emission in IRAS 15179+3956.

If IRAS 15179+3956 contains a water maser, we must explain the non-detection in the most recent survey. Wagner (2013) provided a tight upper bound on isotropic maser luminosities in IRAS 15179+3956 of 16.92 $L_\odot$. A 130$L_\odot$ maser is a full order of magnitude brighter than that estimated in previous work. The feature could be a good deal less luminous, however, as it seems to appear atop a baseline bump. Fitting a gaussian to the peak $\sim$4 km s^{-1} feature gives a luminosity of 12 $L_\odot$ which would be consistent with prior observations. Measuring the luminosity of the full 70 km s^{-1} feature from the base of the swell, rather from the 0 mJy baseline still gives a bright feature at 65 $L_\odot$. With an integration time of $\sim$ 15 minutes, Wagner achieved an rms noise of 2.9 mJy before smoothing, which is comparable to the peak luminosity of the water feature in

IRAS15179+3956. If the feature appeared in a baseline trough (e.g. Figure **??**, middle panel) as could be characteristic of such observations, the signal would have been lost. Previous observations also took place nearly a year before ours, giving time for possible variability in the feature to render it detectable in our survey. If Wagner's upper bound is strict, our detection corresponds to a $5-10$-fold increase in maser luminosity which, though large, has been observed in some nuclear water masers. Finally, we cannot exclude the possibility that the feature is RFI related in spite of our meticulous efforts to eliminate such signals during flagging. The feature in IRAS 15179+3956 fails to qualify as a formal $5-7\sigma$ detection. There are good reasons to believe IRAS 15179+3956 is a legitimate detection, however, including the fact that the galaxy's morphology and nuclear type conform to other dual megamaser hosts. We will discuss this in greater detail in §6.

IRAS 15179+3956 is a merging system with a HII nucleus. If we accept this detection, IRAS 15179+3956 is the third (or 4th after the questionable case of UGC 5101) galaxy hosting dual megamasers to take place in a merger remnant with separated nuclei. Optical diagnostics place both its north and south nuclei as HII-type as is also the case with IC 694 and IIZw96. If our detection is legitimate, the evidence is suggestive that OH and H_2O megamasers may trace very particular galactic conditions related to mergers or perhaps signal a brief phase of galaxy evolution along the merger sequence. As we only have a sample size of 2 or 3, this conclusion can be warranted without both followup on IRAS 1519+3956 as well as the detection of additional galaxies cohosting OH and H_2O megamasers.

4.6 Effectiveness of the Survey

A survey for H_2O emission among OH megamaser hosts poses a problem in that OH megamasers are spread more widely in z, rending maser emission more difficult to constrain. In Figure 4.5, we plot detection limits of our survey as a function of z for 3σ Gaussian peak with 2 km s^{-1}

FWHM assuming a 1, 2 and 4 mJy rms noise over the entire 200 MHz band. Superposed on this are the individual upper limits of the masers in our sample, variations in upper limits being derived from system temperatures and differing integration times ($30-60$ minutes). The location of our megamaser detection is indicated with a cross. One will note that at very high z ($z \sim 0.3$), our survey will only be effective in observing masers with $L_{\mathrm{H_2O}}/L_{\odot} > 400$. Though such water masers are inherently rare (see Bennert et al. 2009), very luminous water megamasers at high z have been detected. With only a few exceptions (IRAS 10039-3338, IRAS 11010+4107, IRAS 11506-3851, IRAS 12243-0036, IRAS 15065-1107, IRAS 15247-0945), our survey does not provide upper bounds on water emission below $L/L_{\odot} = 10$.

Very luminous water masers tend to be associated with AGN activity and masers appearing on molecular disks may have velocities far (1000s of km s^{-1}) displaced from the systemic. At 20 GHz our 200 MHz bands span a velocity of range of $\sim$ 3000 km s^{-1} centered on the systemic velocity. Our second 200 MHz band offers similar velocity coverage toward lower frequencies covering a total velocity coverage of about (-4500 km s^{-1}, +1500 km s^{-1}). In this particular regard, our observations are identical to water observations of e.g. Braatz (2008). In some cases, RFI prevented full use of the band, so upper bounds on emission were determined from portions of the band near the systemic velocity (see notes on Table 2). In these special cases, our upper bounds do not constrain emission of possible high velocity features.

Maser luminosities of AGN-pumped water masers can vary dramatically on the timescale of years. We cannot exclude the possibility that a fraction of our nondetections arose from missing maser flares.

Table 4.1. Megamaser Sample and Summary of Observations

object name	RA	DEC	z	rms* (mJy)	$\log(L_{\rm OH}/L_\odot)$	$\log(L_{\rm H_2O}/L_\odot)$	Notes
IRAS 00057+4021	00:08:20.5	+40:37:57	0.044660	3.77	1.93	<1.26	Sy 2
IRAS 03260-1422	03:28:24.3	-14:12:07	0.043350	2.78	2.04	< 1.11	Starburst
IRAS 03521+0028‡	03:54:42.2	+00:37:03	0.151910	-	1.96	-	Starburst
IRAS 03566+1647‡	03:59:29.1	+16:56:26	0.133522	-	1.61	-	Sy2
IRAS 04121+0223‡	04:12:47.1	+02:30:36	0.122424	-	2.29	-	HII
IRAS 06487+2208	06:51:45.8	+22:04:27	0.143390	2.70	2.90	<2.17	HII, ULIRG
IRAS 07163+0817‡	07:19:05.5	+08:12:07	0.110973	-	1.47	-	HII
IRAS 07572+0533‡	07:59:57.2	+05:25:00	0.190000	-	2.63	-	LINER, ULIRG
IRAS 08071+0509	08:09:47.2	+05:01:09	0.052203	1.66	1.90	< 1.08	Radio Jet, HII
IRAS 08201+2801	08:23:12.6	+27:51:40	0.167830	2.44	3.30	<2.27	HII, ULIRG
IRAS 08279+0956‡	08:30:40.9	+09:46:28	0.208634	-	2.98	-	LINER
IRAS 08449+2332	08:47:50.2	+23:21:10	0.151458	2.54	2.12	<2.20	HII, ULIRG
IRAS 08474+1813†	08:50:18.3	+18:02:01	0.145404	2.35	2.66	< 2.13	Sy 2, ULIRG
IRAS 09039+0503‡	09:06:34.2	+04:51:25	0.125140	-	2.63	-	LINER
IRAS 09531+1430†	09:55:51.1	+14:16:01	0.215275	2.20	3.01	<2.45	Sy 2
IRAS 09539+0857†	09:56:34.3	+08:43:06	0.128899	2.14	3.26	<1.98	
IRAS 10039-3338	10:06:05.1	-33:53:17	0.034100	2.47	2.86	< 0.87	LIRG, merger
IRAS 10036+2740	10:06:26.3	+27:25:46	0.165531	2.14	1.99	< 2.204	ULIRG
IRAS 10173+0828	10:20:00.2	+08:13:34	0.049087	1.67	2.46	< 1.03	LIRG
IRAS 10339+1548‡	10:36:37.9	+15:32:42	0.197236	-	2.34	-	Sy 2, ULRIG
IRAS 10378+1109†	10:40:29.2	10:53:18	0.136274	2.61	3.20	<2.12	ULIRG, LINER
IRAS 11010+4107	11:03:53.2	+40:50:57	0.034524	1.47	1.74	<0.67	LIRG, ring-like
IRAS 11029+3130	11:05:37.5	+31:14:32	0.198604	2.43	2.53	<2.55	LINER, ULIRG
IRAS 11180+1623	11:20:41.7	+16:06:57	0.166000	1.89	2.17	<2.15	LINER, ULIRG
IRAS 11506-3851	11:53:11.7	-39:07:49	0.010781	3.84	1.52	<-0.613	LIRG
IRAS 11524+1058	11:55:02.8	+10:41:44	0.178670	2.48	2.81	< 2.34	LINER, ULIRG
IRAS 12018+1941	12:04:24.5	+19:25:10	0.168646	2.43	2.49	< 2.28	Sy 2
IRAS 12032+1707	12:05:47.7	+16:51:08	0.217787	2.42	4.15	<2.50	LINER, ULIRG
IRAS 12112+0305	12:13:46.0	+02:48:38	0.073317	5.94	2.78	<1.454	LINER, ULIRG, HII
IRAS 12162+1047	12:18:47.7	+10:31:11	0.146500	2.43	2.05	< 2.15	
IRAS 12243-0036	12:26:54.6	-00:52:39	0.007268	1.60	-0.01	< -0.546	Sy 2, LIRG

Simply integrating the water megamaser luminosity function (Bennert et al. 2009; McKean 2011) over the volume of our survey as characterized by our bandwidth of ~ 400 MHz, number of pointings (46) and field of view (2.5 arcmin) with upper and lower isotropic luminosity limits of $10^{-3}L_\odot$ and $10^3L_\odot$, i.e. assuming the survey is blind, predicts ~ 3 masers with luminosities $\geq 1L_\odot$ in our survey volume. 12% of 100,000 Monte Carlo simulations which treated maser luminosities with our detection limits predicted we would detect at least one maser. However, with a global detection rate of $\sim 3\%$ across all galaxies surveyed in the literature and $\sim 10\%$ detection rates among Seyfert 2 galaxies, we might estimate the number of detections to be $\sim 1-2$ maser detections with ~ 1 detection toward a Seyfert 2 type nucleus.

4.7 The OH and H_2O Megamaser Connection

Previous to this study, approximately 61 galaxies had been searched for both OH and H_2O emission which also showed emission in one of the two molecules. With 43 observations of galaxies which have never previously been observed, our study nearly doubles this number. In particular, previous to the present study, 35 objects which had been searched in both molecules showed emission in only water while only 18 galaxies showed only hydroxyl. Now a total of 103 galaxies have been searched for emission in both molecules and show emission in at least one maser species, 60 of these being established OH maser hosts.

Previous studies have included UGC 5101 as a possible dual megamaser. A very luminous water maser was detected toward UGC 5101 (Martin 1989), which has not been detected in followup observations (Baan et al. 1992). We re-reduced VLBI 1665 MHz observations (VLBA project VLBA_VSN000352) of UGC 5101 and were unable to either find a line or to image the emission. Of the tentative detections discussed, UGC 5101 is the only maser observation where follow up observations were unsuccessful in detecting a signal. For these reasons, we omit UGC 5101 in our

Table 4.1 (cont'd)

object name	RA	DEC	z	rms* (mJy)	$\log(L_{OH}/L_\odot)$	$\log(L_{H_2O}/L_\odot)$	Notes
IRAS 12540+5708	12:56:14.2	+56:52:25	0.042170	2.37	2.84	$<$1.04	LIRG, Sy 1
IRAS 12548+2403	12:57:20.0	+23:47:46	0.131700	3.40	1.89	$<$ 2.20	
IRAS 13218+0552‡	13:24:19.9	+05:37:05	0.205102	-	3.07	-	Sy 1.5
IRAS 14043+0624‡	14:06:49.8	+06:10:36	0.113187	-	1.68	-	
IRAS 14059+2000‡	14:08:18.7	+19:46:23	0.123700	-	2.97	-	
IRAS 14070+0525	14:09:31.2	+05:11:31	0.264380	3.88	3.88	$<$2.88	ULIRG, Sy 2
IRAS 14553+1245	14:57:43.4	+12:33:16	0.124900	2.28	1.94	$<$ 2.00	
IRAS 14586+1431	15:01:00.4	+14:20:15	0.147700	2.39	2.54	$<$2.37	
IRAS 15065-1107	15:09:16.1	-11:19:18	0.006174	2.10	0.04	$<$-0.61	Sy 2, HII
IRAS 15179+3956‡	15:19:47.1	39:45:38	0.047570	-	1.02	$<$1.23**	merger, HII
IRAS 15224+1033	15:24:51.5	+10:22:45	0.134049	2.53	2.22	$<$2.08	
IRAS 15250+3609	15:26:59.4	+35:58:38	0.055155	1.57	2.52	$<$1.09	ULIRG, LINER
IRAS 15247-0945	15:27:27.8	-09:55:41	0.040004	1.67	1.59	$<$0.84	LINER
IRAS 15587+1609†	16:01:03.6	+16:01:03	0.137181	2.00	3.04	$<$2.00	HII
IRAS 16100+2528‡	16:12:05.4	+25:20:23	0.132385	-	1.68	-	LINER
IRAS 16255+2801‡	16:27:38.1	+27:54:52	0.133612	-	2.38	-	HII, ULRIG
IRAS 16300+1558	16:32:21.4	+15:51:46	0.241747	1.79	2.71	$<$ 2.46	ULIRG, Sy2
IRAS 16399-0937	16:42:40.2	-09:43:14	0.027012	2.00	1.68	$<$0.570	LIRG
IRAS 17160+2006	17:18:15.6	+20:02:58	0.109800	1.77	2.04	$<$1.75	
IRAS 17208-0014	17:23:21.9	-00:17:01	0.042810	1.80	3.04	$<$0.92	Starburst, LINER
IRAS 17540+2935	17:55:56.1	+29:35:26	0.108108	2.23	1.56	$<$1.83	LINER
IRAS 18368+3549	18:38:35.4	+35:52:20	0.116170	2.28	2.81	$<$1.90	Sy 2
IRAS 18544-3718	18:57:52.7	-37:14:38	0.073424	3.32	2.23	$<$1.66	HII, Spiral
IRAS 18588+3517	19:00:41.2	+35:21:27	0.106727	2.09	2.12	$<$1.79	HII, Spiral
IRAS 20550+1656	20:57:23.9	+17:07:39	0.036098	1.28	1.92	**2.60**	HII, LIRG, merger
IRAS 21077+3358	21:09:49.0	+34:10:20	0.176699	2.71	2.94	$<$ 2.35	LINER
IRAS 21271+2514	21:29:29.4	+25:27:50	0.150797	2.80	3.36	$<$2.43	
IRAS 22025+4205	22:04:36.1	+42:19:38	0.014310	2.02	0.86	$<$ -0.047	Spiral
IRAS 23019+3405‡	23:04:21.1	+34:21:48	0.108038	-	1.78	-	Sy 2
IRAS 23365+3604	23:39:01.3	+36:21:08	0.064480	2.44	2.30	$<$1.40	pec, LINER, ULIRG

Note. —
Boldfaced entries represent detections. Italicized objects have been observed previously, but this study provides tighter upper limits for water megamasers.

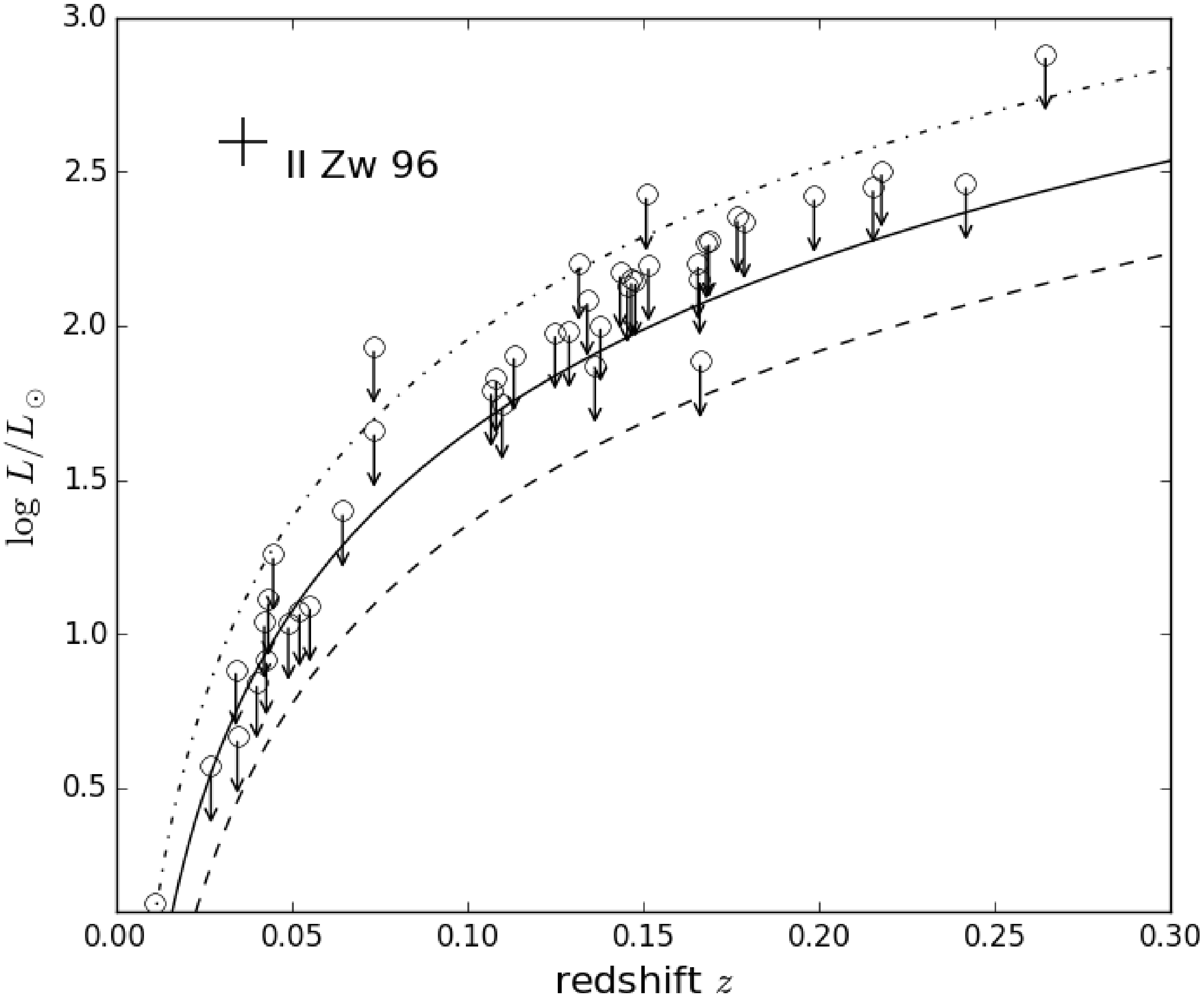

Figure 4.5 Isotropic water maser luminosity upper limits for our survey plotted against redshift z. Open circles correspond to H_2O non-detections. The dashed, solid and dot-dashed curves are the sensitivity limits of 1, 2 and 4 mJy rms observations for a ∼ 2 km s^{-1} (∼ 5.5 channel) feature. Our survey is only effective at constraining very luminous maser emission at higher z. Our maser detection is indicated with a black cross.

analysis, but will provide some discussion on how our results change if the questionable case of UGC 5101 is considered.

In the bottom panel of Figure 4.6, we plot a "Baldwin, Phillips & Terlevich" (BPT) diagnostic panel for as many galaxies in our sample as have values for optical spectroscopy line values available in the literature (Lozinskaya et al. 2009; Darling & Giovanelli 2006; Veillux et al. 1999; Zenner & Lenten 1993; Garcia-Marlin 2006; Baan et al. 1998). Plus symbols represent OH maser hosts for which no water was detected. In this figure, IRAS 16399-0937 has been included twice as the location of the OH megamaser is unknown (Sales et al. 2014). Blue and inset red triangles mark positions of galaxies with dual masers, the size of the triangles being proportional to $\log[L/L_\odot]$ for water and hydroxyl respectively. The dashed line is Kauffman et al. (2003) demarcation line distinguishing starburst galaxies from AGN. The solid line is the demarcation criterion from Kewley et al. (2001) or the "extreme-stardust" line. With the exception of UGC 5101, both systems (Arp299 and IIZw96) hosting dual megamasers are classified as HII nuclei. In general, however, dual masers trace the BPT positions of sole OH emitters well. A KS test in $\log([\mathrm{OIII}])/\mathrm{H}\beta$ between dual masers and OH maser hosts does not exclude the possibility that the two may be drawn from the same distribution ($p = 0.39$) and a test in $\log([\mathrm{NII}])/\mathrm{H}\alpha$ gives $p = 0.29$.

In Figure 4.7, we plot all galaxies searched for both OH and H_2O emission in OH vs. H_2O maser luminosity space. Objects appearing in red are OH megamaser which have never previously been observed in the literature. Yellow circles corresponding to OH megamasers which have been observed previously but for which tighter upper bounds were achieved in this study. Upper limits in emission in OH and H_2O are indicated by horizontal and vertical arrows respectively.

T11 noted a lack of H_2O kilomasers in OH megamaser hosts compared to OH kilomasers among H_2O hosts, i.e. between Quadrants I (hereafter QI) and QIII. We carried out a survival analysis (e.g. Feigelson & Babu, 2012; Feigelson & Nelson 1985) between the heavily censored samples of upper limits and maser luminosities in Q1 and Q3 to investigate a potential of the lack

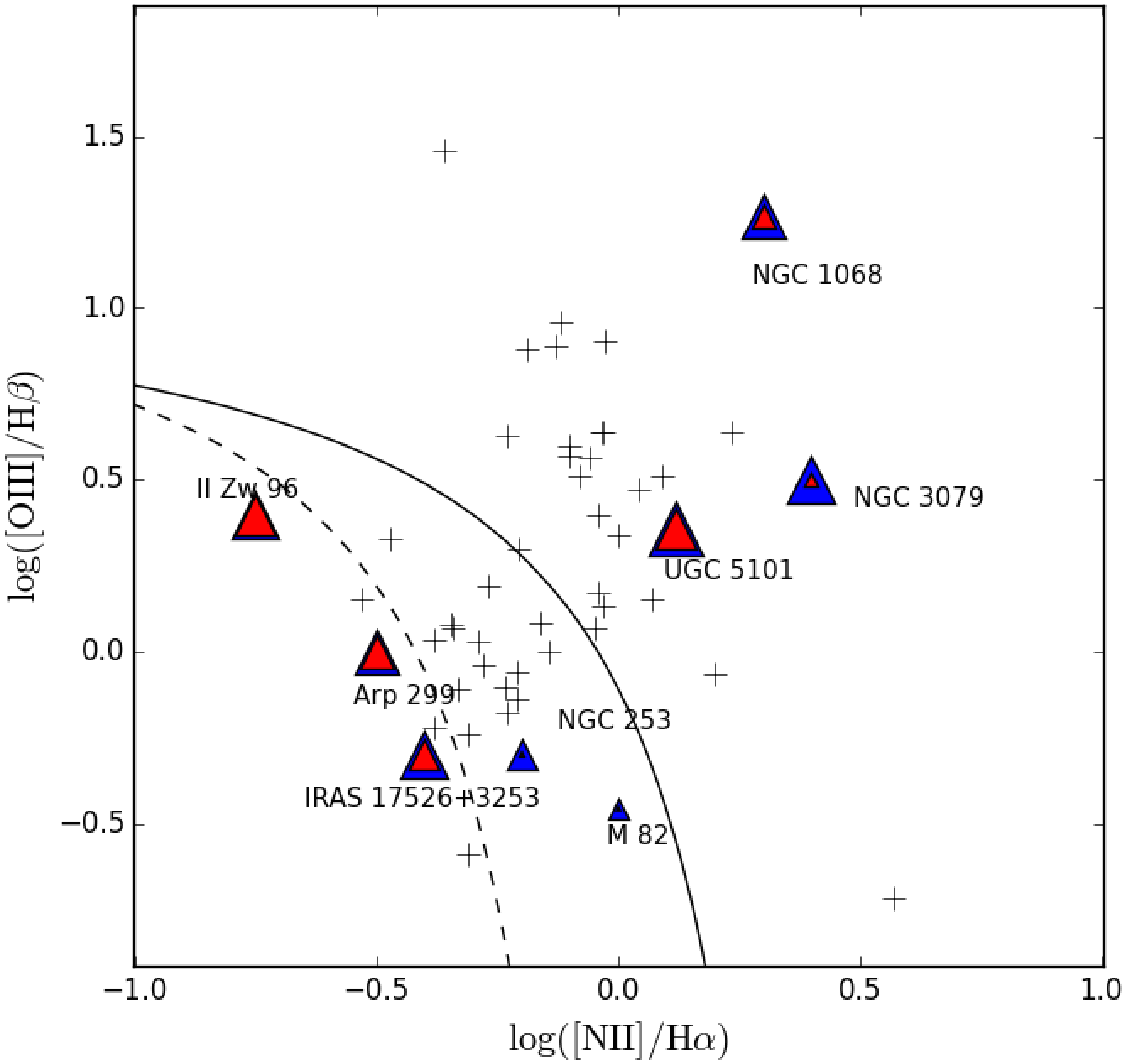

Figure 4.6 BPT diagnostic tool diagram for as many OH megamaser host galaxies in our survey for which [OIII]/Hβ and [NII]/Hα existed in the literature (see text). Plus symbols are OH megamasers for which no water maser emission was detected. Maser emission toward all known dual maser hosts are represented as triangles with the relative size of the triangles proportional to the isotropic luminosities of water (blue) and hydroxyl (red) emission. Note that in all cases of megamaser coexistence, water emission is more luminous than hydroxyl (see discussion in text). Note that fluxes reported are for single dish measurements and that fluxes reported for the entire Arp 299 system should not be confused with fluxes from IC 694 which contains the dual megamaser.

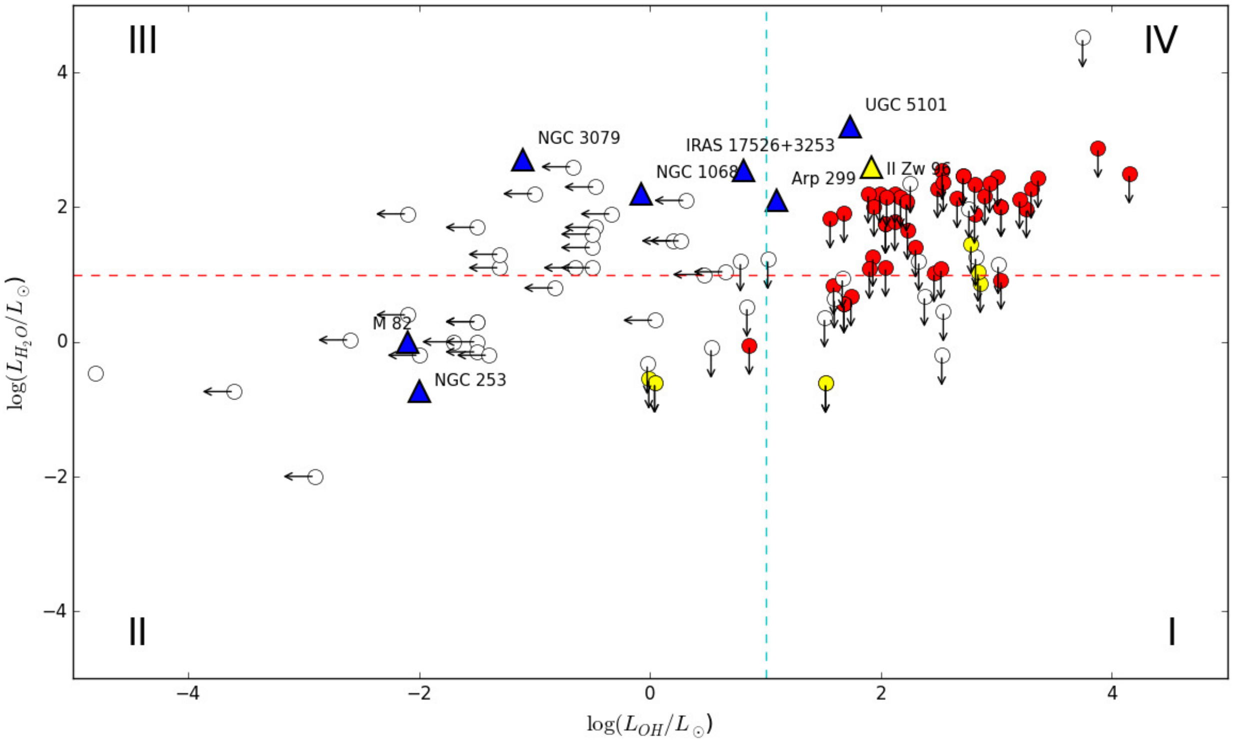

Figure 4.7 OH vs. H_2O luminosities for all galaxies searched for both OH and H_2O maser emission. As in T11, dual megamaser galaxies appear as triangles. Blue triangles are sources dual megamasers from T11. Circles or triangles with yellow filling are objects which have been previously observed in the literature (e.g. T11; Wagner 2013) and which were observed again in this study. Symbols with red filling are galaxies which have never been observed previous to this study. The sensitivity of our survey does not eliminate many galaxies as H_2O megamaser candidates by Tarchi's criterion ($\log(L_{\mathrm{H_2O}}/L_\odot) > 1.0$, i.e. many galaxies have upper limits appearing in quadrant IV).

of water kilomasers compared to OH kilomasers in dual megamaser hosts. We used the survival analysis package (Therneau 2015) in R (R Core Team 2013), utilizing both the Mantel-Haenszel and Peto & Peto tests to bracket the effects of different non-detection weightings. The probabilities that we observe no emission from Q1 with the null hypothesis that there is no difference between maser luminosities between quadrants is $p = 0.0896$ and $p = 0.0863$ for the Mantel-Haenszel and Peto & Peto tests respectively. The difference between kilomaser luminosities and hence numbers of detections between the quadrants is thus marginally significant.

In every case of coexistance, OH is less luminous than its H_2O counterpart (see Figure 4.6). Further, OH megamasers coexisting with H_2O masers are substantially less luminous than sole OH masers. While this might appear to indicate that coexisting OH megamasers are a distinct population from sole OH megamasers, this is likely due to the independent natures of the water (Bennert et al. 2009; Henkel et al. 2005) and hydroxyl (Darling et al. 2002) luminosity functions. Dual megamasers are confined to relatively small survey volume compared to the entire OH megamaser catalog. Comparing luminosity functions reveals that in a given relatively small survey volume[3], more H_2O masers of a given luminosity will appear than OH of the same luminosity which implies that the brightest maser in the volume will likely be of H_2O type. Indeed, this is the same effect which makes comparisons between Q1 and QIII of Figure 4.7 difficult. This effect would need to be disentangled before one considers this trend as evidence for an interplay between the two megamaser species.

We find no statistical difference in our water maser detection rate (2.17%) among OH hosts and the rate of the rest of the literature combined (3.7%).

So far all galaxies co-hosting dual megamasers, including UGC5101 are merger remnants. If one excludes UGC5101, the remaining two dual megamasers are merging galaxies with spatially

---

[3] Here we mean a sufficiently small survey volume such that we do not expect to detect masers with $L > 1000L_{\odot}$, where the two luminosity functions intersect. Such luminous OH masers are more abundant per volume than H_2O.

distinct nuclei which are optically classified HII-type. Interferometric followups, in particular using VLBI, on IIZw96 is needed to diagnose its masing behavior, but the known additional similarities between IIZw96 and Arp 299 could suggest tight constraints on dual megamasering in general.

4.8 Conclusions

We have reported on a systematic search for 22 GHz water emission in established OH megamaser hosts with the Robert C. Byrd Green Bank Telescope (GBT). Our ~ 60 hour survey of 47 sources nearly doubles the number of galaxies now searched for both OH and H_2O emission with confirmed emission in at least one molecule. This effort is additionally significant because many galaxies searched for emission in both molecules are established water masers leaving many OH megamasers un-probed. We confirm to $> 8\sigma$ the previously tentative water maser detection toward IIZw96. This finding reinforces the celebrated similarities (e.g. Imani et al. 2010; Goldader et al. 1997) between IIZw96 and Arp 299, the only other known host of both megamaser species. Our hour-long integration was sufficient to resolve multiple, luminous narrow water features toward IIZw96. IIZw96 provides another vital site to investigate dual megamasing.

Our survey is sensitive enough to eliminate 6 galaxies as H_2O megamaser ($L/L_\odot > 10$) candidates. For the first time, we verify, on a statistical basis, a marginally significant lack of H_2O kilomasers among OH megamaser hosts. The two, and so far only, dual megamaser hosts are HII type and are galaxy mergers with spatially distinct nuclei.

BIBLIOGRAPHY

Ade, P. A. R. *et al.* [Planck Collaboration], arXiv:1502.01589

Agarwal, B., Dalla Vecchia, C., Johnson, J. L., Khochfar, S., Paardekooper, J.-P. 2014, MNRAS, 443, 648

Agarwal, B., et al. 2015, MNRAS, submitted (arXiv:1510.01733)

Ahn, K., Shapiro, P. R., Iliev, I. T., Mellema, G., Pen, U.-L. 2009, ApJ, 695, 1430

Arnett, D., 1995, "Supernovae and Nucleosynthesis: An investigation of the history of matter from the Big Bang to Present", Princeton University Press.

Aykutalp, A., Wise, J. H., Spaans, M., Meijerink, R. 2014, ApJ, 797, 139

Baan, W. A., Haschick, A., & Henkel, C. 1992, AJ, 103, 728

Baan, W. A., Salzer, J. J., LeWinter, R. D. 1998, ApJ, 509, 633

Baek, S., Ferrara, A. 2013. MNRAS, 432, L6

Barnes, L., 2009, Ph.D. Diss. Cambridge.

Bennert, N., Barvainis, R., Henkel, C., Antionucci, R., 2009, ApJ, 695, 276

Bethe, H. A., G. E. Brown, J. Applegate, J. M. Lattimer, 1979, Nucl. Phys. A 324, 487

Blondin, J. M., A. Mezzacappa, C. DeMarino, 2003, ApJ, 584, 971

Braatz, J. A., Gugliucii, N. E. 2008, ApJ, 678, 96

Braatz, J. A., Reid, M. J., Humphreys, E. M. C., Henkel, C., Condon, J. J. & Lo, K. Y. 2010, ApJ, 718, 657

Bromm, V., Kudritzki, R. P., Loeb, A. 2001, ApJ, 552, 464

Bromm, V., Yoshida, N., Hernquist, L., McKee C. 2009, *Nature*, 49-54

Bruenn, S. W. et al. 2013, ApJ, 767, L6

Bruenn, S. W. , De Nisco, K. R., Mezzacappa, A. 2001, ApJ, 560, 326

Bryan, Greg L, *et al.* 2013, ApJS, 211, 2, 19

Burrows, A. 2012, Reviews of Modern Physics, 85, 245

Burrows, A., Dessart, L., Livne, E., 2007, AIP Conference Series, 937, 370

Burrows, A., Dolene, J.C., Murphy, J. W., 2012, arXiv:1204.3088

Campisi, M.A., Maio, U., Salvaterra, R., Ciardi, B. 2011, MNRAS, 416, 2760

Castangia, P., Panessa, F., Henkel, C., Kadler, M., Tarchi, A., 2013, MNRAS, 436, 3388

Cavagnolo1, K. W., McNamara1, B. R., Nulsen, P. E. J., Carilli, C. L., Jones, C., & L. Birzan. 2010, ApJ, 720, 1066

Chatzopoulos, E., Wheeler, J. C. 2012, ApJ748, 42

Chatzopoulos, E., Wheeler, J. C., Vinko, J., Nagy, A. P., Wiggins, B. K., Even, W. P. 2016, ApJ(in review), arXiv:1603.06926

Chen, X., Ellingsen, S., Baan, W. A., Qiao, H.-H., Li, J., An, T., Breen, S. 2015, ApJ, 800, L2

Chon, S., Hirano, S., Hosokawa, T., Yoshida, N. 2016, ApJ, submitted (arXiv:1603.08923)

Christlieb, N., Bessell, M., Beers, *et al.* 2002, *Nature,* 419, 904-906

Colgate, S., R. White, 1965, ApJ, 143, 626

Condon, J. J. 1992, ARA&A, 30, 575

Constantin, A., 2012, JPCS, 372, 2047

Couch, S. 2013, ApJ, 775, 35

Couch, S., C. Ott, 2013, ApJL, 778, L7

Couch, S., O'Connor, E. 2014, ApJ, 785, 123

Darling, J., 2007, ApJ, 669, L9

Darling, J., Giovanelli, R. 2002, ApJ, 572, 810

Darling, J., PhD diss., Cornell University, 2002

Darling. J., Giovanelli, R., 2006, AJ, 132, 2596

DeBuhr, J., Quataert, E., Ma, C.-P., Hopkins, P., 2010, MNRAS, 406, L55

Deguchi, S. 1981, ApJ249, 145

Dessart, L. Audit, E., Hillier, D. J. 2015, 449, 4304

Dijkstra, M. 2014. Publications of the Astronomical Society of Australia, 31

Dijkstra, M., Gronke, M., Sobral, D. 2016, ApJ, submitted (arXiv:1602.07695)

Dijkstra, M., Haiman, Z., Mesinger, A., Wyithe, J. S. B. 2008, MNRAS, 391, 1961

Dixon, T. G., Joseph, R. D., 2001, ApJ, 740, 99

Dubois, Y., Devriendt, J., Slyz, A. & Romain Teyssier, 2011, arXiv:1109.1457

Elitzur, M., Hollenback, D. J., McKee, C. F. 1989, ApJ, 346, 983

Epstein, R. I. 1979, MNRAS, 188, 305

Feigelson, E. D., Babu, G. J., 2012, Cambridge University Press, UK

Feigelson, E. D., Nelson, P. I., 1985, ApJ, 293, 192

Filippenko, A. V. 1997, Ann. Rev. Astron. Astrophys, 35, 309

Frebel, A., Aoki, W., Christlieb, N., Ando, H., Asplund, M., Barklem, P., Beers, T., Eriksson, K., Fechner, C., Fujimoto, M., Honda, S., Kagino, T., Minezaki, T., Nomoto, K., Norris, J., Ryan, S., Takada-Hidai, M., Tsangarides, S., Yoshii, Y. 2005, *Nature,* 434, 871-873

Frey, L., Even, W., Whalen, D., Fryer, C., Hungerford, A., Fontes, C., Colgan, J. 2013, ApJ, 204, 16

Fryer, C., Benz, W., Herant, M., Colgate, S.A. 1999, ApJ, 516, 892-899

Gallimore, J. F., Henkel, C., Baum, S. A., Glass, I. S., Claussen, M. J., Preito, M. A., von Kap-Herr, S. 2001, ApJ, 556, 694

Garica-Marin, M., Colina, L., Arribas, S., Alonso-Herrero, A., Mediavilla, E. 2006, ApJ650, 850

Gittings, M., Weaver, R., Clover, M., Betlach, T., Byrme, N., Coker, R., Dendy, E., Hueckstaedt, R., New, K., Oakes, W., Ranta, D., Stefan, R. 2008, arXiv, 0804.1394.

Goldader, J. D., Goldader, D. L., Joseph, R. D., Doyon, R., Sanders, D. B. 1997, AJ 1113, 1569

Greene, Seth, den Brok, Braatz, Henkel, Sun, Peng, Kuo, Impellizzeri & Lo, 2013, ApJ, 771, 121

Greenhill, L. J., Ellingsen, S. P., Norris, R. P., Gough, R. G., Sinclair, M. W., Moran, J. M., Mushotzky, R. 1997, ApJ, 474, L103

Grefenstette, B. W., *et al.*, 2014, Nature, 506, 339

Habouzit, M., Volonteri, M., Latif, M., Dubois, Y., Peirani, S. 2016, MNRAS, submitted

Hahn, O.& T. Abel. 2011, MNRAS, 415, 2101

Haiman, Z. 2013, ASSL, 396, 293

Hanke, F., A. Marek, B. Muller, H.-T. Janka, 2012, ApJ, 755, 138

Harrington, J. P. 1973, MNRAS, 162, 43

Hartwig, T., et al. 2015, MNRAS, submitted (arXiv:1512.01111)

Hatchett, S., Buff, J., McCray, R., 1976, 206, 847

Heinz, S., & R. A. Sunyaev. 2003, MNRAS, 343, L55

Herant, M., Benz, W., Hix, W. R., Fryer, C. L., Colgate, S. A. 1994, ApJ, 435, 339

Herrnstein, J. R., Moran, J. M., Greenhill, L. J., Diamond, P. J., Inoue, M., Nakai, M., Miyoshi, M., Henkel, C., Riess, A., nature, 400, 539

Hirano, S., Hosokawa, Yoshida, N., Umeda, H., Omukai, K., Chiaki, G., Yorke, H. 2014, ApJ, 781, 60-81

Hosokawa, T., Omukai, K., Yoshida, N., Yorke, H. 2011, *Science,* 334, 1250-1253

Humphreys E. M. L., Reid, M. J., Moran, J. M., Greenhill, L. J., Argon, A. L., 2013, ApJ775, 13

Inami H. *et al.* 2010, AJ, 140, 63

Ishibashi, W., Courvoisier, T. J.-L. 2011, A&A, 525, A118

Janka, H.-T., 2012, Annual Review of Nuclear and Particle Physics, 62, 407

Janka, H.-T., L. Hudelpohl, A. Marek, B. Muller, M. Obergaulinger, 2012, arXiv:1211.1378

Joggerst, C. C., Almgren, A., Bell, J., Heger, A., Whalen, D., Woosely, S. E., 2009, ApJ, 709, 11-26

Johanson, A. K., Migenes, V., Breen, S. L. 2014, ApJ, 781, 78

Johnson, J. L. 2010, MNRAS, 404, 1425

Johnson, J. L., Haardt, F. 2016, PASA, in press (arXiv:1601.05473)

Johnson, J. L., Khochfar, S., Greif, T. H., Durier, F. 2011, MNRAS, 410, 919

Johnson, J.L., Dalla, V.C., Khochfar, S. 2013, MNRAS, 428, 1857

K. Hirata *et al.*, 1987, Phys. Rev. Lett. 58, 1490

Kauffman G., Heckman, T. M., Tremonti, C., Brichmann, J., Charlot, S., White, S. D. M., Ridgeway, S. E., Brinkmann, J., Fukugita, M., Hall, P., Ivezic, Z., Richards, G. T., Schneider D. P. 2003, MNRAS, 346, 1055

Kassen, D., Thomas, R. C., Nugent, P. 2006, ApJ, 651, 366

Kewley, L., Dopita, M., Sutherland, R., Heisler, C., Trevena, J. 2001. ApJ, 566, 121

Kitaura, F. S., Janka, H.T., Hillebrandt, W. 2006, A&A, 450, 345.

Klöckner, 2004, PhD. Thesis.

Kondratko, P. T., Greenhill, L. J., Moran, J. M., 2006, ApJ, 652, 136

Kuhlen, M., Madau, P. 2005, MNRAS, 363, 1069

Kuo, Braatz, Condon, Impellizzeri, Lo, Zaw, Schenker, Henkel, Reid, Greene, 2011, ApJ, 727, 20

Kylafis, N. D., Norman, C. A. 1991, ApJ, 373, 525

Latif, M. A., Ferrara, A., 2016, arXiv preprint, arXiv:1605.07391

Lo, K. Y. 2005, Annu. Rev. Astron. Astrophys. 43, 625-676

Lonsdale, C. J. 2002. Cosmic Masers: From Proto-Stars to Black Holes, 206, 413

Lozinskaya, T. A., Egorov, O. V., Moiseev, A. V., Bizyaev, D. V., 2009, Astronomy Letters, 35, 730

Magee, N.H., Abdallah, Jr. J., Clar, R.E.H., Cohen, J.S., Collins, L.A., Csanak, G., Fontes, G., Gauger, A., Keady, J.J., Kilcrease, D.P., Merts, A. L. 1995, *Astronomical Society of the Pactific Conference Series,* Vol 78, Astrophysical Applications of Powerful New Databases, ed. SJ Adelman, WL Wiese, 51

Marek, A., H.-T. Janka, 2009, ApJ, 694, 664

McKean, J. P., Impellizzeri, C. M. V., Roy, A. L., Castangia, P., Samuel, F., Brunthaler, A., Henkel, C., Wucknitz, O., 2011, MNRAS, 410, 2506

Meier, D. L. 2001. ApJ, 548, L9

Meiksin, A., Whalen, D. 2013, MNRAS, 430, 2854-2863

Merloni, A., Heinz, S. & T. Di Matteo, 2003, MNRAS, 345, 1057

Migenes, V., Coziol, R., Cooprider, K., Klockner, H.-R., Plauchu-Frayn, I., Islas, J. M., Ramierez-Garduno, L. 2011, MNRAS, 416, 1267

Moretti, A., Ballo, L., Braito, V., Caccianiga, A., Ceca, R., Gilli, R., Salvanterra, R., Severgnini, P., Vignali, C. 2014, A&A, 563, A46

Moriya, T. J., Blinnikov, S. I., Tominaga, N., Yoshida, N., Tanaka, M., Maeda, K., & Nomoto, K. 2013, MNRAS, 428, 1020

Muller, B., H.-T. Janka, A. Heger, 2012a, ApJ, 761, 72

Muller, B., H.-T. Janka, A. Marek, 2012b, ApJ, 756, 84

Muratov, A., Gnedin, O., Gnedin, N., Zemp, M. 2013, ApJ, 773, 19

Neufeld, D. A. 2000, ApJ, 542, L99

Neufeld, D. A., Melnick, G. J. 1991, ApJ, 368, 215

Nomoto, K., Iwamoto, K., Mazzali, P.A., Umeda, H., Nakamura, T., Patat, F., Danziger, I.J., Young, T.R., Suzuki, T., Shigeyama, T., Augusteijn, T., Doublier, V., Gonzalez, J.F., Boehnhardt, H., Brewer, J., Hainaut, O.R., Lidman, C., Leibundgut, B., Cappellaro, E., Turatto, M., Galama, T.J., Vreeswijk, P.M., Kouveliotou, C., Van Paradijs, J., Pian, E., Palazzi, E., Frontera, F. 1998, *Nature,* 395, 672674

Nordhaus, J., A. Burrows, A. Algren, J. Bell, 2010, ApJ, 720, 694

Oh, S. P., Haiman, Z., Rees, M. J. 2001, ApJ, 553, 73

Ott, M., Witzel, A., Guireenback, A., Krichbaum, T. P., Standke, K. J., Schalinski, C. J., Hummel, C. A., 1998, A&A, 284, 311

Pacucci, F., Ferrara, A., Grazian, A., Fiore, F., Giallongo, E. 2016, MNRAS, accepted (arXiv:1603.08522)

Pallottini, A., et al. 2015, MNRAS, 453, 2465

Pan, T., Loeb, A., Kasen, D. 2012, MNRAS, 423, 2203

Paxton, B., Cantiello, M., Arras, P., Bildsten, L., Brown, E., Dotter, A., Mankovich, C., Montgomery, M.H., Stello, D., Timmes, F.X., Townsend, R. 2013, ApJS, 192, 3

Perez-Torres, M., Alberdi, A., Romero-Canizales, C., Bondi, M. 2010, A&A, 519, L5

Pihlstroöm, Y. M., 2007, IAU Symp., 242

R Core Team, 2013, R: A language and environment for statistical computing. R Foundation for Statistical Computing, Vienna, Austria.

Rakavy, G., Shaviv, G. 1967, ApJ, 148, 803

Regan, J., Haehnelt, M. 2009a, MNRAS, 393, 858-871

Regan, J. A., Johansson, P. H., Wise, J. H. 2015, MNRAS, submitted (arXiv:1511.00696)

Regan, J. A., Johansson, P. H., Wise, J. H. 2016, MNRAS, submitted (arXiv:1603.06612)

Reid, Braatz, Condon, Greenhill, Henkel & Lo, 2009, ApJ, 695, 287

Reid, Braatz, Condon, Lo, Kuo, Impellizzeri, Henkel. 2013, ApJ, 767, 154

Sales, D. A., Robinson, A., Axon, D. J., Gallimore, J., Kharb, P., Curran, R. L., O'Dea, C., Baum, S., Elitzur, M., Mittal, R. 2015, ApJ799, 25

Schaerer, D. 2002, A&A, 382, 28

Schneider, P. 2006, Extragalactic Astronomy & Cosmology: An Introduction, Springer-Verlag, Berlin

Smidt, J., Whalen, D., Chatzopoulos, E., Wiggins, B. K., Chen, K.-J., Kozyreva, A., Even, W., 2014b, 805, 11

Smidt, J., Whalen, D., Even, W., Wiggins, B. K., Johnson, J., Fryer, C., Stiavelli, M. 2014a, ApJ, 797, 97

Smith, A., Bromm, V., Loeb, A. 2016, MNRAS, submitted (arXiv:1602.07639)

Sobral, D., et al. 2015, ApJ, 808, 139

Tarchi, A., 2012, IAU Symp., 287

Tarchi, A., Castangia, P., Henkel, C., Surcis, G., Menten, K. M., 2011, A&A, 525, A91 (T11)

Therneau, T., 2015, A Package for Survival Analysis in S. version 2.38

Tumlinson, J., Giroux, M. L., Shull, J. M.. 2001, ApJ, 550, L1

Turk, Matthew J. 2011, ApJS, 192, 9

Valdes, M., & Ferrara, A. 2008, MNRAS, 387, L8

Valiante, R., Schneider, R., Volonteri, M., Omukai, K. 2016, MNRAS, 457, 3356

Veilleux, S., Kim, D.-C., Sanders, D. B. 1999, ApJ, 522, 113

Visbal, E., Haiman, Z., Bryan, G. L. 2014, MNRAS, 445, 1056

Visbal, E., Haiman, Z., Bryan, G. L. 2016, MNRAS, submitted (arXIv:1602.04843)

Vlemming W. H. T., van Langevelde, H. J., Diamond, P. J. 2005, Mem. S. A. It., 76, 462

Volonteri, M. 2012, Sci, 337, 544

Young, P., Fryer, C. 2007, ApJ, 644, 1033

Wagner, J. 2013, A&A, 560, A12

Wanajo, S. , K. Nomoto, H.-T. Janka, F. S. Kitaura, and B. Muller, 2009, ApJ, 695, 208

Warren, M., Salmon, J. 1995. Computer Physics Communications, 87, 266

Weaver, T.A., Zimmermann, G.B., Woosley, S.E. 1978, ApJ, 225, 1021

Whalen D. 2012, arXiv, 1209.4688

Whalen, D., Abel, T., Norman, M. L. 2004, ApJ, 610, 14

Whalen, D., Abel, T., Normon, M. 2004, ApJ, 610, 14

Whalen, D., Even, W., Frey, L., Smidt, J., Johnson, J., Lovekin, C., Fryer, C., Stiavelli, M., Holz, D., Heger, A., Woosley, S.E., Hungerford, A.. 2013a, ApJ, 777, 110

Whalen, D., Joggerts, C., Fryer, C., Stiavelli, M., Heger, A., Holtz, D.. 2013b, ApJ, 768, 95

Whalen, D., Smidt, J., Even, W., Woosely, S.E., Heger, A., Stiavelli, M., Fryer, C. 2014b, ApJ, 781, 106

Whalen, D., Smidt, J., Johnson, J., Holz, D., Stiavelli, M., Fryer, C. 2014a, arXiv:1312.6330

Wild, V., Heckman, T., Charlot, S., 2010 MNRAS, 405, 933

Wilson, J.R., 1985, "Numerical Astrophysics", ed. J. M. Centrella, J. M. Leblanc, & R. L. Bowers, p. 422.

Wise, J., Abel, T. 2011, MNRAS, 414, 3458-3491

Wise, J., Turk, M., Abel, T. 2008, ApJ, 682, 745

Wise, J., Turk, M., Norman, M., Abel, T. 2011, ApJ, 745, 50

Wollaeger, R. T., van Rossum, D. R. 2014, ApJS, 214, 28

Woosley, S.E. 1993, ApJ, 405, 273

Woosley, S. E., Blinnikov, S., & Heger, A. 2007, Nature, 450, 390

Wu, X.-B., Wang, F., Fan, X. et al. 2015, Nature, 518, 512

Yang, Y., Zabludoff, A. I., Dave, R., Eisenstein, D. J., Pinto, P. A., Katz, N., Weinberg, D. H., Barton, E. J. 2006. ApJ, 640, 539

Young, P. A., Fryer, C. L., 2007, ApJ, 664, 1033

Zemcov, M., Smidt, J., Arai, T., et al., 2014. *Science*, 346, 6210

Zenner, S., Lenzen, R. 1993, A&A, 101, 363

Zhang J. S., Henkel, ., Kadler, M., Greenhill, L. J., Nagar, N., Wilson, A. S., Braatz, J. A., 2006, A&A, 450, 933

Zhang, J.S., Henkel, C., Guo, Q., Wang, J., 2012, arXive preprint arXiv:1201.2075

Zhu, G., Zaw, I., Blanton, M.R., Greenhill, L., 2011, ApJ, 742, 73

INDEX